ADVANCED MATERIALS
www.advmat.de

Flexible and Stretchable Organic Electrochemical Transistors for Physiological Sensing Devices

Yao Yao, Wei Huang, Jianhua Chen, Xiaoxue Liu, Libing Bai, Wei Chen, Yuhua Cheng, Jianfeng Ping,* Tobin J. Marks,* and Antonio Facchetti**

Flexible and stretchable bioelectronics provides a biocompatible interface between electronics and biological systems and has received tremendous attention for in situ monitoring of various biological systems. Considerable progress in organic electronics has made organic semiconductors, as well as other organic electronic materials, ideal candidates for developing wearable, implantable, and biocompatible electronic circuits due to their potential mechanical compliance and biocompatibility. Organic electrochemical transistors (OECTs), as an emerging class of organic electronic building blocks, exhibit significant advantages in biological sensing due to the ionic nature at the basis of the switching behavior, low driving voltage (<1 V), and high transconductance (in millisiemens range). During the past few years, significant progress in constructing flexible/stretchable OECTs (FSOECTs) for both biochemical and bioelectrical sensors has been reported. In this regard, to summarize major research accomplishments in this emerging field, this review first discusses structure and critical features of FSOECTs, including working principles, materials, and architectural engineering. Next, a wide spectrum of relevant physiological sensing applications, where FSOECTs are the key components, are summarized. Last, major challenges and opportunities for further advancing FSOECT physiological sensors are discussed.

1. Introduction

Physiological sensing by means of building interfaces between sensing elements and cells, tissues, and organs of biological systems is of great significance for the fundamental investigation of biosignal transmission and processing,[1–3] disease diagnosis,[4–7] pathology,[8–12] and health monitoring.[13–16] The development of flexible/stretchable electronic devices that are sensitive to physiological signals provides an efficient and convenient way for not only basic pathological research but also the realization of wearable electronics for reliable in situ medical diagnosis and monitoring.[17–22] A physiological signal could be divided into several categories such as biochemical, bioelectrical, bioacoustic, biomagnetic, biomechanical, bioimpedence, and biooptical, however, the most investigated in the context of flexible/stretchable sensors are mainly the former two signals. The operating principles for biochemical sensing (such as ions and metabolites of a biological system) by typical electrochemical biosensors are based on the variations of electrical current, voltage potential, and/or impedance induced by a chemical reaction and/or physisorption.[23] However, further signal amplification is usually required, which also calls for more accessible, ultrasensitive, and biocompatible electronic sensing platforms. Bioelectrical sensing includes cell culture and behavior monitoring in vitro, as well as various electrograms' analysis for clinical applications, such as electrocardiography (ECG), electromyography (EMG), electrooculography

Y. Yao, X. Liu, W. Chen, J. Ping
School of Biosystems Engineering and Food Science
Zhejiang University
866 Yuhangtang Road, Hangzhou 310058, P. R. China
E-mail: jfping@zju.edu.cn
Y. Yao, X. Liu, J. Ping
Innovation Platform of Micro/Nano Technology for Biosensing
ZJU-Hangzhou Global Scientific and Technological Innovation Center
Hangzhou 311200, P. R. China

Y. Yao, W. Huang, J. Chen, T. J. Marks, A. Facchetti
Department of Chemistry and the Materials Research Center
Northwestern University
Sheridan Road, Evanston, IL 60208, USA
E-mail: whuang@uestc.edu.cn; t-marks@northwestern.edu; a-facchetti@northwestern.edu
W. Huang, L. Bai, Y. Cheng
School of Automation Engineering
University of Electronic Science and Technology of China (UESTC)
Chengdu, Sichuan 611731, P. R. China
A. Facchetti
Laboratory of Organic Electronics, Department of Science and Technology
Linköping University
Norrköping 60174, Sweden

The ORCID identification number(s) for the author(s) of this article can be found under https://doi.org/10.1002/adma.202209906

DOI: 10.1002/adma.202209906

(EOG), and electroencephalography (EEG), which monitor electrical signals generated from the activities of heart, muscle, eye, and brain, respectively, in vivo.[24–26] However, for in situ recording of bioelectrical signals in a wide frequency and amplitude ranges, challenges exist in achieving high signal-to-noise ratio (SNR) and analyte sensitivity. Moreover, the robustness and stability of the sensors under complex mechanical deformations remain challenging and still lack of in-depth research. Consequently, it is critical to develop flexible/stretchable electronics that can realize stable and ultrasensitive detection of physiological signals in complex biological systems.

An emerging technology that holds broad prospects for overcoming the abovementioned limitations is the organic electrochemical transistor (OECT), an ideal multifunction device that is suitable for both biochemical and bioelectrical sensing. Since it was first proposed by Wrighton and co-workers in 1984,[27] OECTs of different types have demonstrated superb abilities in chemical sensing,[28–34] cell culture and action potential recording,[35–40] and health monitoring.[41–45] OECTs exhibit a unique set of advantages for various sensing applications, such as: 1) a biocompatible organic (semi)conductor in the OECT channel making it an ideal platform to interface with biological systems;[46–48] 2) fabrication of OECTs is compatible with various low-temperature processing techniques, from low-cost, high-throughput printing methods to conventional photolithography;[49–52] 3) benefiting from the signal conversion and amplification capabilities of OECTs, high current modulation and fast response can be achieved leading to excellent sensing performance;[53–55] 4) operation of OECTs in aqueous electrolyte solutions is suitable for working in complex physiological environments;[56] 5) high compatibility of OECTs with traditional microelectronic integration techniques enables the fabrication of high density sensing arrays for mapping purposes[57–59] as well as fabrication of OECT-based microfluidics for multiple analyte detection;[60–62] 6) Most importantly, OECT fabrication can be carried out on flexible/stretchable plastic/elastomeric substrates, which can provide satisfactory mechanical compliance for various in vivo and in vitro sensing applications.[56,63–65]

Several important reviews have summarized recent OECT achievements, mainly focusing on the aspects of chemical and biological sensing capabilities of these devices,[48,54,66–68] the molecular design of the organic semiconductor,[47,69] and the electrolyte gate dielectric materials for these devices,[70] as well as elaborating on the composition, functions, and applications of OECTs.[71,72] In addition, OECTs have been also reviewed in the context of flexible organic electronics.[63,73–76] However, a detailed and systematic overview focusing on recent progress of flexible/stretchable OECTs (hereafter indicated as FSOECTs) used in physiological monitoring, including biochemical and bioelectrical sensing of biological systems, is lacking.

In this review, recent developments in FSOECTs interfacing with various biological systems for physiological sensing are summarized. First, we delve into the working principles and sensing mechanisms of OECTs, summarize design strategies for FSOECTs, and then introduce different physiological sensing applications based on these devices. Conclusions and prospects of FSOECTs for future applications in the areas for health monitoring, clinical diagnosis, and finally pathobiology research are discussed.

2. Working Principle of OECTs

2.1. Background

There are several types of transistor operating modes and architectures.[42,77–83] Among that using organic (or channel) semiconductors as the key material element, the organic field effect transistor (OFET) is the more mature technology that has attracted far more research efforts.[77,84–86] A typical OFET is composed of three electrodes (source, drain, and gate), an organic semiconductor forming the charge carrying channel between the source and drain electrodes, and a gate dielectric (electronic insulator) separating the semiconductor from the gate electrode.[78] The channel source-to-drain current (I_{DS}) is controlled by changing both the gate voltage (V_{GS}), which controls the induced electrostatic carrier charge density at the dielectric/semiconductor interface, and the source–drain voltage bias (V_{DS}) (**Figure 1**a). The amplification capability of an OFET consists of converting a modulation of V_{GS} into a variation of I_{DS} and is defined as the transconductance ($g_m = \Delta I_{DS}/\Delta V_{GS}$), which is one important performance parameter of transistors, including OFETs.

When the gate dielectric of an OFET is replaced with an electronically insulating but ionic conducting electrolyte, ions in the electrolyte can move under the effect of gate electric field and form an electrical double layer at the interface of the electrolyte with the semiconductor. Compared to conventional gate dielectrics, such as most metal oxides and insulating polymers,[88] the use of electrolytes typically leads to far larger gate capacitance (typically >1 μF cm^{-2}) and lower driving voltage (typically <3 V).[80,81] Devices operating in this mode are defined as organic electrical double layer transistors (OEDLTs) (Figure 1b). However, unlike in a typical OEDLT, where ions only accumulate at the electrolyte side of the semiconductor–electrolyte interface, in OECTs, the ions can penetrate into the semiconductor bulk and this process is associated with a redox reaction of the organic semiconductor. The ion intake/outtake and the redox process vary the electronic carrier density in the semiconductor modulating the electronic conductivity of the channel upon application of V_{GS}/V_{DS} biases (Figure 1c).[89] Consequently, a volumetric capacitance is associated with OECT operation, which is typically orders of magnitude higher than that in typical OFETs/OEDLTs,[90–94] as well as solution processed metal oxide FETs/EDLTs,[95–101] leading to a large amplification capability at low driving voltages (typically <1 V for aqueous electrolyte).[42,71] Figure 1d compares the g_m range of OFETs, OEDLTs, and OECTs versus driving voltage, but note, the driving voltages of OFETs are typically much larger than the 5 V reported in this figure.

The most advanced OECTs reported to date are based on p-type (hole-transporting or electrochemically oxidized) semiconductors, while n-type (electron-transporting or electrochemically reduced)-semiconductor-based OECTs remain rare, are typically less stable, and exhibit much lower performance compared to their p-type counterparts. Even though a few studies have reported stable n-type OECT operation, their g_m remains about 10^2–10^3 lower than that of the best p-type OECTs.[102–105] Additional details and discussion can be found in previous reviews.[69,106–108] Here we stress the aspects of gate-voltage-induced charge depletion and charge accumulation in OECTs since they are the basis of the physiological sensing process.

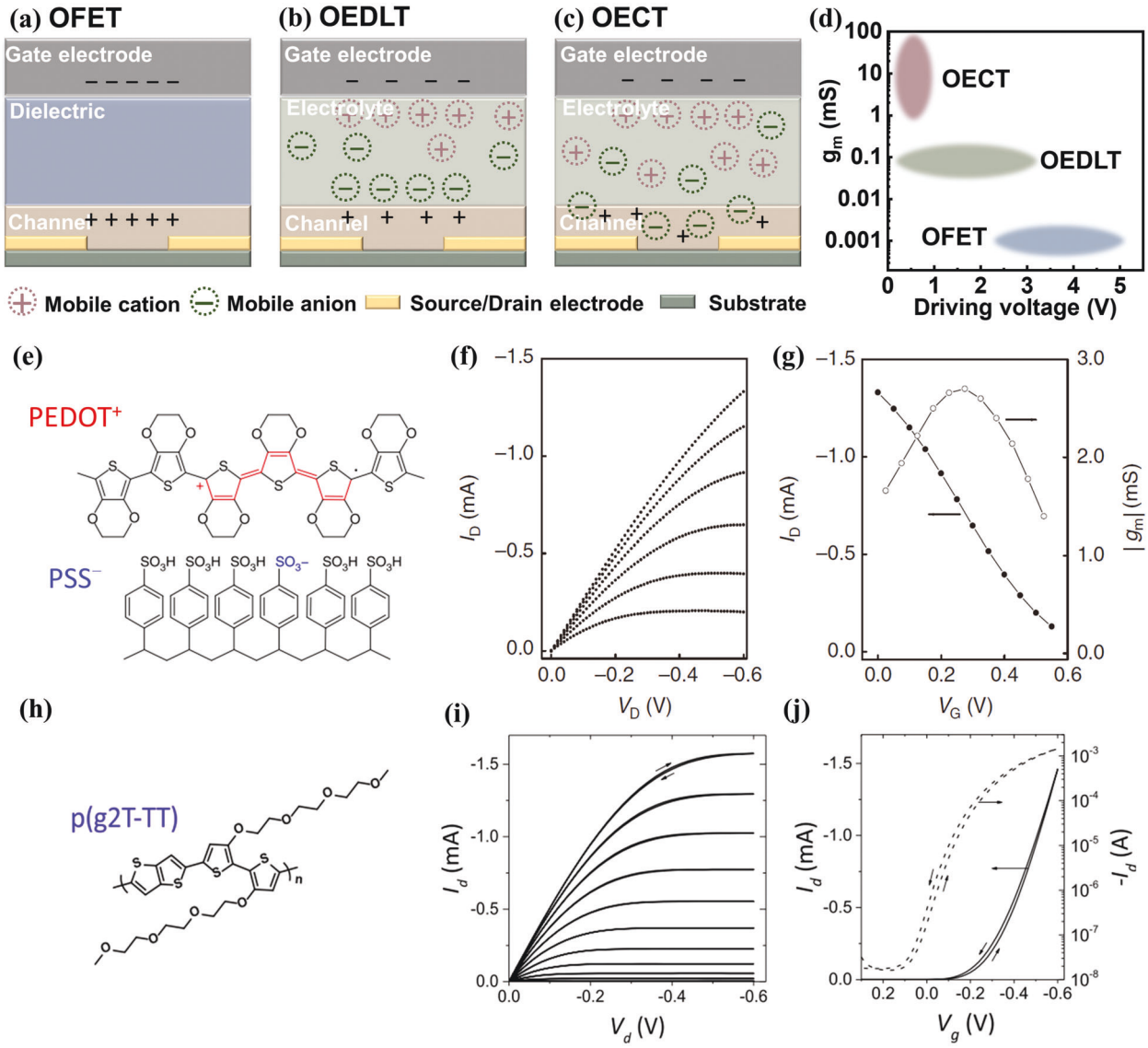

Figure 1. a–c) Schematic illustration of various transistor structures and operation of OFET (a), OEDLT (b), and OECT (c). d) Comparison of device driving voltage and transconductance (g_m) between OFET, OEDLT, and OECT. e) Molecular structure of the p-type conducting polymer PEDOT:PSS. f) Output and g) transfer characteristics and the associated g_m of PEDOT:PSS-based depletion-mode OECT. e–g) Reproduced with permission.[79] Copyright 2013, Springer Nature. h) Molecular structure of the p-type semiconducting polymer p(g2T-TT). i) Output and j) transfer characteristics of p(g2T-TT)-based enhancement-mode OECT. h–j) Reproduced with permission.[87] Copyright 2016, National Academy of Science.

Figure 1e shows the chemical structure of poly(styrene sulfonate)-doped poly(3,4-ethylenedioxythiophene) (PEDOT:PSS), which is one of the most investigated channel materials in OECTs and specifically in OECT-based sensors.[79] Since this material consists of hole-doped PEDOT chains with PSS counterions, pristine PEDOT:PSS OECTs function in the depletion mode where the application of a (positive) V_{GS} dedopes (reduces) the polymer decreasing the drain current (I_{DS}). This device is normally ON, as the representative current–voltage output and transfer characteristics of a PEDOT:PSS-based OECT in Figure 1f,g clearly show.[79]

However, most organic semiconductors for OECTs operate in the enhancement mode, meaning that they are normally OFF before application of a gate bias. For instance, the polymer poly(2-(3,3′-bis(2-(2-(2-methoxyethoxy)ethoxy)ethoxy)-[2,2′-bithiophen]-5-yl)thieno[3,2-*b*]thiophene) (p(g2T-TT)) (Figure 1h) is a p-type semiconductor widely investigated in the OECT literature.[87,109–111] In enhancement-mode OECTs, a negative V_{GS} results in anions being injected into the channel with concomitant doping (oxidation) of the polymer leading to enhanced I_{DS} (ON state) (Figure 1i,j).

Despite the faster switching speeds and higher I_{DS} of depletion mode OECTs compared to those of enhancement mode OECTs, they hold inherent disadvantages particularly for biosensing applications; the output current of depletion mode sensors may decrease faster over time due to rapid polymer degradation under

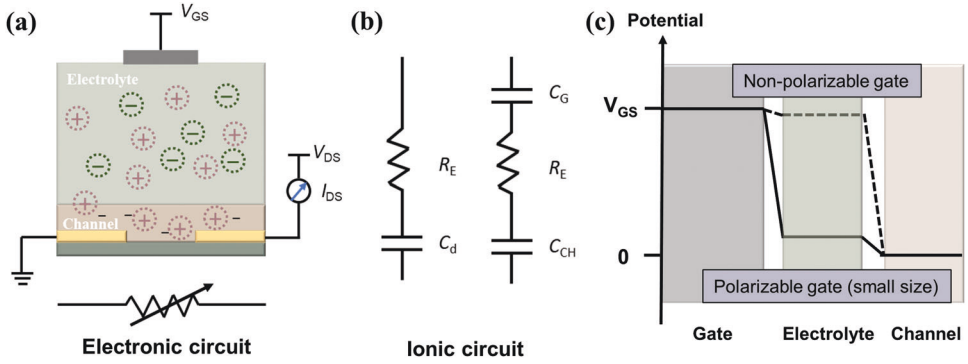

Figure 2. a) The electronic circuit of an OECT, where V_{GS} is the gate voltage, V_{DS} is the drain voltage, I_{DS} is the channel current. b) The ionic circuit models of OECTs with nonpolarizable gate electrode (left) and metal gate electrode (right) where C_G corresponding to the capacitors of gate is considered, C_{CH} is the channel capacitor, and R_E represents the resistance of electrolyte. c) Gate potential distribution on the gate/electrolyte and channel/electrolyte interfaces with nonpolarizable gate electrode (dashed line) and polarizable gate electrode (solid line), respectively.

the always-ON working condition affecting sensing output signal and large power consumption.

2.2. Basic Physics of OECTs

Understanding the physics and details of OECT operations is vital for the design of high-performance OECT-based sensors. Various physical models for OECTs haven been proposed,[42,112–116] among them, Bernards' model[112] consists of a combination of electronic (**Figure 2**a) and ionic circuits (Figure 2b, left) best reproducing the steady-state and transient transport behaviors of depletion mode OECTs. In this model, the drain–channel–source current is defined as an electronic circuit (Figure 2a) working as a resistor with a resistance that varies upon gating. The gate–electrolyte–channel part is defined as an ionic circuit where ions are stored in the electrolyte and flow into the channel. This circuit includes a capacitor, corresponding to the volumetric capacitance of the channel (C_{CH}), and a resistor (R_E) referring to the ionic strength of the electrolyte in series. In this case, the capacitance of the gate is neglected (vide infra). This model implies a purely capacitive process, according to which ions injected in the channel do not exchange charge with the organic film but rather electrostatically compensate the presence of opposite charges. The electronic charge transport in the OECT channel in the steady state is described by the following equations[112,117]

$$I_{DS} = \begin{cases} \mu C^* \frac{Wd}{L}\left[1 - \frac{V_{GS} - \frac{1}{2}V_{DS}}{V_T}\right] V_{DS},\ V_{DS} > V_{GS} - V_T \\ -\mu C^* \frac{Wd}{L}\frac{\left[V_{GS} - V_T\right]^2}{2V_T},\ V_{DS} < V_{GS} - V_T \end{cases} \quad (1)$$

where μ is the hole mobility; C^* is the capacitance per unit volume of the channel; V_T is the threshold voltage; and W, L, d are the channel width, length, and thickness of channel material, respectively.

Since g_m is defined as the derivative of I_{DS} with respect to V_{GS} ($\Delta I_{DS}/\Delta V_{GS}$), it can be expressed by the following equations

$$g_m = \begin{cases} -\mu C^* \frac{Wd}{L} V_{DS},\ V_{DS} > V_{GS} - V_T \\ \mu C^* \frac{Wd}{L}\left[V_{GS} - V_T\right],\ V_{DS} < V_{GS} - V_T \end{cases} \quad (2)$$

According to this equation, g_m of an OECT is directly proportional to Wd/L ($g_m \propto Wd/L$), thus the physical thickness of the channel material is a parameter that can tune the device performance. This distinguishes OECTs from OFETs and OEDLTs as electrochemical doping in OECTs modulates the carrier density throughout the bulk of the semiconductor, while the modulation of carrier density in field-effect devices only occurs in the semiconductor near the interface with the dielectric. The different charge accumulation explains the far higher g_m of OECTs compared with other organic transistor technologies.

In addition to the steady-state behavior, the source–drain current transient response of an OECT can also be described by the ionic circuit of Bernards' model (Figure 2b, left). The ionic circuit involving the gate implies that the time required for the channel electronic current in an OECT to respond to a gate voltage change is characterized by a RC time constant, τ_i, given by $R_E C_{CH}$.[112] It was found that the channel capacitance, C_{CH}, is proportional to the channel volume WdL, that is, $C_{CH} \propto WdL$, and the slope of C_{CH} vs WdL affords the capacitance per unit volume of the channel (C^*) discussed above.[42] In addition, the electrolyte resistance R_E, as another parameter determining the time constant τ_i, follows the scaling law of $R_E \propto 1/\sqrt{WL}$.[118,119] After taking the above scaling of C_{CH} and R_E into account, the time constant τ_i is proportional to $d\sqrt{WL}$ ($\tau_i \propto d\sqrt{WL}$).[120] Thus, the response speed of an OECT to a gate voltage change can also be tuned by varying the device geometry. Most importantly, putting together the scaling laws of g_m and τ_i, a trade-off between these two OECT figure of merits can be drawn since decreasing W and d improves the response speed but via sacrificing the device g_m. Therefore, an optimal device geometry must be considered when designing a device having specific application requirements.

If, for simplicity, the capacitance of the gate–electrolyte interface is neglected in the discussion of the ionic circuit, the device capacitance (C_i) is the equivalent capacitance of two capacitors, C_{CH} of the electrolyte–channel interface and C_G of the gate–electrolyte interface (Figure 2b, right), and it is given by the equation

$$C_i = \frac{1}{1/C_{CH} + 1/C_G} \quad (3)$$

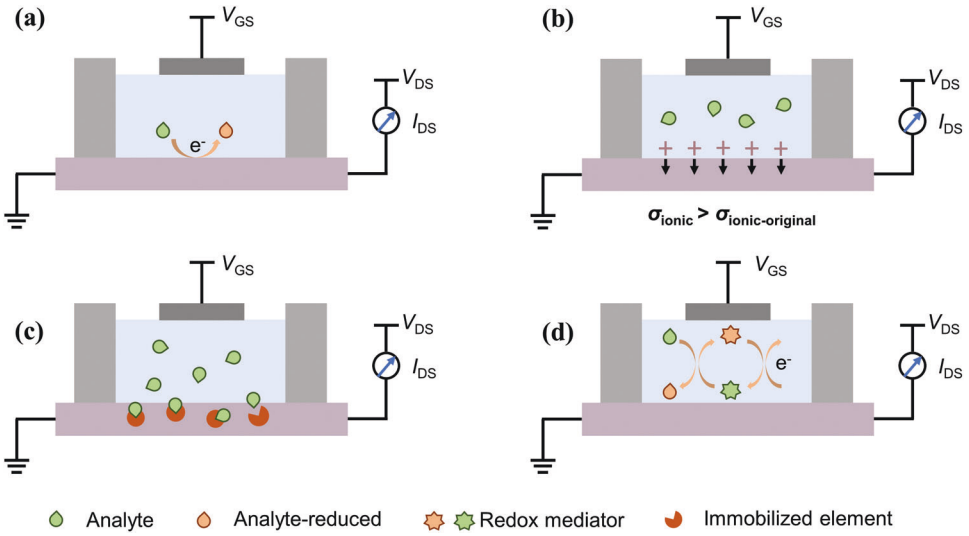

Figure 3. a–d) Schematic representation of different OECT sensing mechanisms of an analyte for biochemical signal detection.

In this case, the sum of the voltage drop at the two interfaces equals that of the applied V_{GS}, which mainly drops across the smaller capacitor. For nonpolarizable gate electrodes (e.g., Ag/AgCl or a thick PEDOT:PSS film) (Figure 2c), the gate capacitance (C_G) can be considered infinite. Thus, Equation (3) can be described as $C_i = C_{CH}$, with V_{GS} mainly dropping at the electrolyte–channel interface achieving an efficient gating.[71] When using a polarizable gate electrode (e.g., Pt or Au) with a small size, C_G cannot be neglected. Thus, the capacitance in the scaling laws of g_m and τ_i should be replaced by C_i. Otherwise, an ultralarge gate electrode affording a capacitance ≈10× larger than that of the channel is required to achieve an efficient gating of the channel, which however complicates device integration.

3. Sensing Mechanisms Using OECTs

There are four major types of sensing mechanisms for analyte biochemical signal detection using an OECT: 1) the analyte chemically reacts with the semiconductor channel material (**Figure 3**a);[121–123] 2) the analyte interacts with the electrolyte changing the ionic conductivity (σ_{ionic}) (Figure 3b);[124,125] 3) conformational changes of the semiconductor upon binding with the analyte guest (Figure 3c);[126–128] 4) a cascade event caused by the presence of the analyte causing a change in the semiconductor chemical state (Figure 3d).[129,130] In all cases, the analyte concentration can be acquired based on the change of the channel current, I_{DS}, or the change of effective gate voltage (V_{GS}^{eff}, the equivalent voltage that needs to be applied in the absence of the analyte at the gate electrode in order to afford the same I_{DS}). Most of the current FSOECT-based sensors employed in biochemical signals detection follow the last working mechanism.[131–133]

For the detection of bioelectrical signals, an OECT is usually employed as a transconductance amplifier converting changes in the electrical potential to changes in the channel current. The working principle of OECT sensing for electrophysiological monitoring is based on the local field potential changes caused by an ion flux during various activities of an organ, a tissue, or even a single electrogenic cell, which can further modulate I_{DS}. The SNR measurement is commonly used as the gold standard for quantifying the performance of electrophysiological recording events (for instance, action potentials). Usually, the SNR value of OECT-based electrophysiological sensors is calculated by taking the highest peak (A_{signal}: amplitude of signal) during a period of activity and the standard deviation of the background (A_{noise}: amplitude of noise), according to the equation

$$\mathrm{SNR\,[dB]} = 20\log_{10}\left(\frac{A_{signal}}{A_{noise}}\right) \quad (4)$$

The scaling laws (Equations (1)–(3)) derived from models can provide general guidelines for how to optimize the performance of OECT-based sensors by tuning the device geometry. The g_m, τ_i, and the distribution of the voltage drop at gate–electrolyte interface and electrolyte–channel interface correlate to the key OECT sensing figures of merit, which are the amplification property, operation frequency, and effective gate voltage (V_{GS}^{eff}). Therefore, the device geometry of OECT-based sensors should be optimized to the requirements of a particular sensing application.

For instance, when using an OECT to record bioelectronic signals for clinical applications (e.g., ECG, EOG, EEG), the signals are characterized by small action potential differences (as low as 10 μV) at low frequencies (<100 Hz). In this regard, the signals must be amplified enough to provide a significant information to track a certain activity or process. Therefore, OECTs for sensing electrophysiological signals should be designed with a large Wd/L ($g_m \propto Wd/L$) to achieve high signal amplification even at the cost of sacrificing the operating frequency. Other sensing modalities, such as fast-scan cyclic voltammetry or monitoring single-neuron action potentials, require measurements of the signal at higher frequencies. Therefore, the OECTs for these applications should be designed with a smaller $d\sqrt{WL}$ ($\tau_i \propto d\sqrt{WL}$) in order to decrease the response time.

For some biochemical OECT sensing applications, such as in the case of glucose detection based on enzymatic catalytic reactions which belong to the fourth type of OECT sensing mechanism discussed previously (**Figure 4**a), defining an optimal device

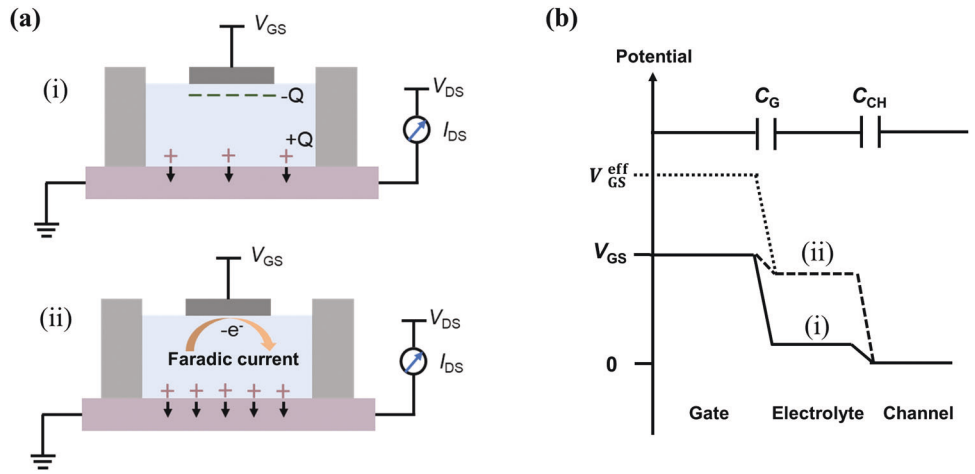

Figure 4. a) Schematic and b) potential diagram of a OECT-based glucose sensor in the absence (i) and presence (ii) of glucose.

geometry is more complex. From the potential diagram shown in Figure 4b, the voltage drop at the gate–electrolyte interface will decrease due to the Faradaic current induced by the enzyme-based catalytic reaction of glucose, thus increasing the effective gate voltage V_{GS}^{eff} and further modulating the I_{DS}. Since the detection mechanism depends on the voltage drop variation at the gate–electrolyte interface, the gate capacitance C_G should not be infinite in this case. Furthermore, V_{GS}^{eff} variation is proportional to C_{CH}/C_G ($\Delta V_{GS}^{eff} \propto 1 + C_{CH}/C_G$) under a certain glucose concentration change,[28] thus, a small polarizable gate electrode is preferred for improving detection sensitivity. In addition to the V_{GS}^{eff} shift, the glucose concentration can also be measured using a change in I_{DS}. According to the Equation (1), a higher detection sensitivity can be obtained upon a higher signal amplification of the device, that is, a higher g_m. However, it should also be considered that the response time of glucose sensing in practical applications is also an important device performance parameter. Thus, the OECT geometry (W, d, L, gate material, and size) utilized in enzyme-based glucose sensors need to be optimized for the requirements of specific application scenarios.

4. Strategies for Fabricating FSOECTs

The need for conformal adhesion at the interfaces between biological systems and sensing electronics has inspired research activities for developing flexible/stretchable sensors. Flexible devices can sustain bending deformations, the extent of which are determined by the Young's modulus of the materials, their thickness, and adhesion characteristics. The ability of a device to be bend depends on the material's mechanical properties but also on the geometry of the system. Device flexibility increases significantly with the reduction of the device and substrate film thicknesses. The bending strain (ϵ) experienced by a material in the bending direction can be calculated by the ratio of the device stack and substrate thicknesses, t_f and t_s, respectively, to twice the radius of curvature, $2r$, and is given by $\epsilon = (t_s + t_f)/2r$.[134] Since these thicknesses are relatively small, the strains associated with bending deformations even at small radii of 0.5–1 mm are typically very limited (<1–2%). Stretchable devices need to sustain more complex mechanical deformations. The strain that stretchable electronic devices can experience includes bending, stretching, shaping, wrapping, twisting, and crumpling.[135] Thus, these deformations typically result in larger strains, which are typically far greater (>10–20%). OECTs hold the advantage of simple fabrication, excellent biocompatibility, as well as proven resilience to mechanical deformations, which are important properties for constructing wearable electronics.[136–138] To date, most flexible OECTs have been constructed on flexible substrates that can only achieve a limited bending strain. However, wearable sensors for biological monitoring can require the device to retain stable performance under larger tensional strains (e.g., the maximum strain of human skin is ≈30%).[139] In this regard, more in-depth research is needed to improve the mechanical resistance of OECT-based sensors to bridge the mechanical property mismatch between the device and biological systems.

FSOECT-based sensors should retain performance under reversible deformations, such as elongation, compression, twisting, bending, and different geometrical distortions. This requirement can be fulfilled by device optimization involving both material selection and component/device engineering (**Figure 5**). Thus, intrinsically flexible/stretchable materials should be used as critical OECT components. For materials expected to endure tensile modes of deformation (e.g., stretching and bending), the key parameters are the tensile (Young's) modulus (E) and crack-onset strain (ϵ_{cr}), which should be as low and large as possible, respectively.[136] Since OECTs are composed of multimaterial stacked (substrate, electrodes, channel material, electrolyte, encapsulation, etc.) layers, each material will likely have a different tensile modulus, which will affect interlayer stresses, adhesion parameters, and delamination behavior. Since the substrate and the encapsulation layer are typically the thicker layer components, their behavior will dictate the deformation of the active materials/electrodes, thus the simplest route to minimize interfacial stresses is to lower the modulus of the latter. The typical modulus of organic semiconductors and polymeric/metal electrodes would have to be lowered by several orders of magnitude to align with those of elastomeric substrates such as poly(dimethylsiloxane) (PDMS) or thermoplastic polyurethanes. In addition, device optimization where the device and/or layer architectures are engineered to enhance deformability includes

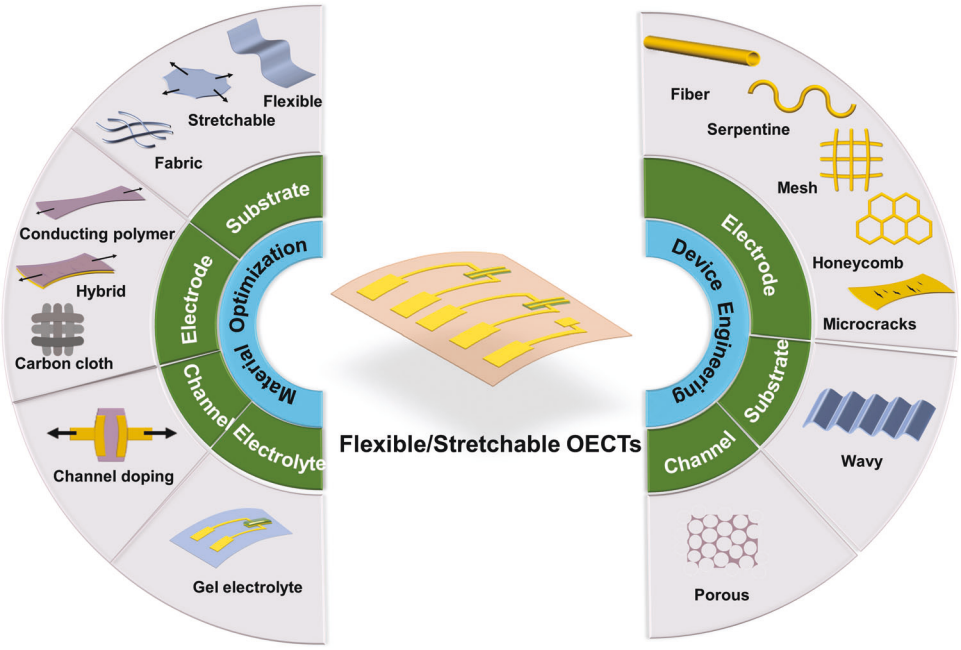

Figure 5. Schematic illustration of the two general approaches for the development of FSOECTs: material optimization (left) and device engineering (right).

the use of flexible/stretchable interconnects (e.g., serpentine, mesh-shaped) and prestrained elastomeric patterns (e.g., waved, buckled, wrinkled, microcracked, or porous patterns). These approaches are elaborated in more detail in the following sections.

4.1. Material Optimization

Major OECT materials that can be optimized include, 1) the substrate for supporting the device, 2) the channel material where ion exchange, redox reactions, and electronic conductance occur, 3) the electrodes for transmitting electronic signals, 4) the electrolyte serving as ion storage and acting as the gate dielectric. **Table 1** summarizes the Young's modulus (E) and crack-onset strain (ϵ_{cr}) of representative substrates, channel materials, electrodes, and electrolytes used in FSOECTs versus conventional electronic materials.

4.1.1. Substrates

The adoption of flexible/stretchable substrates is the most common strategy to achieve flexible/stretchable OECT sensors. Flexible substrates are those which can only bend in 1D at a time, while stretchable ones can conform to a surface with an arbitrary 2D curvature, such as that of the human body.[162] Polymer substrates such as poly(ethylene terephthalate) (PET),[163] poly(ethylene-2,6-naphthalate) (PEN),[164] polyimide (PI),[165] and parylene[79] are commonly used flexible substrates, but these polymers are only suitable for flexible sensors that cannot be stretched. Furthermore, both PET and PEN are not compatible with high temperature (>150 °C) manufacturing processes which may be required for some channel materials.[166,167] PI and parylene are more stable at high temperatures and the latter can be produced as extremely thin flexible films by chemical vapor deposition.[168,169] Furthermore, parylene is biocompatible and biostable, which is important for use at biointerfaces.[170] Other

Table 1. Young's modulus and tensile strain of representative substrate, channel material, electrodes, and electrolyte used in FSOECTs and comparison with classical electronic materials.

	Materials	E [GPa]	ϵ_{cr} [%]	Refs.
Substrates	PET[a)]	2.3 ± 0.3	≈12	[140,141]
	PEN[b)]	3.3 ± 0.4	≈7	[141,142]
	PI[c)]	2.5	≈3	[143,144]
	Parylene	2.8	24.7	[145,146]
	PDMS[d)]	(0.4–5) × 10^{-3}	≈93	[147,148]
	SEBS[e)]	25.4 ± 2.2	518 ± 20	[149]
	Fabric	8.18	3.5	[150]
	Glass	23.8–90.5	≈2	[151,152]
Channel materials	PEDOT:PSS	1.7	9	[153]
	P3HT[f)]	0.252 ± 0.057	>150	[154]
	PANI[g)]	2.6 ± 0.4	6 ± 1	[155]
	IGZO[h)]	130	≈0.75	[156]
	Silicon	150	0.3	[134,157]
Electrodes	Au	70	≈1	[134,158]
	PEDOT:PSS	1.7	9	[153]
Electrolyte	IL[i)] gel	(60–120) × 10^{-6}	>1000	[159,160]
	Hydrogel	(39–907) × 10^{-6}	>1000	[161]

[a)] Poly(ethylene terephthalate); [b)] Poly(ethylene-2,6-naphthalate); [c)] Polyamide; [d)] Poly(dimethylsiloxane); [e)] Styrene–ethylene–butylene–styrene; [f)] Poly(3-hexylthiophene); [g)] Polyaniline; [h)] Indium gallium zinc oxide; [i)] Ionic liquid.

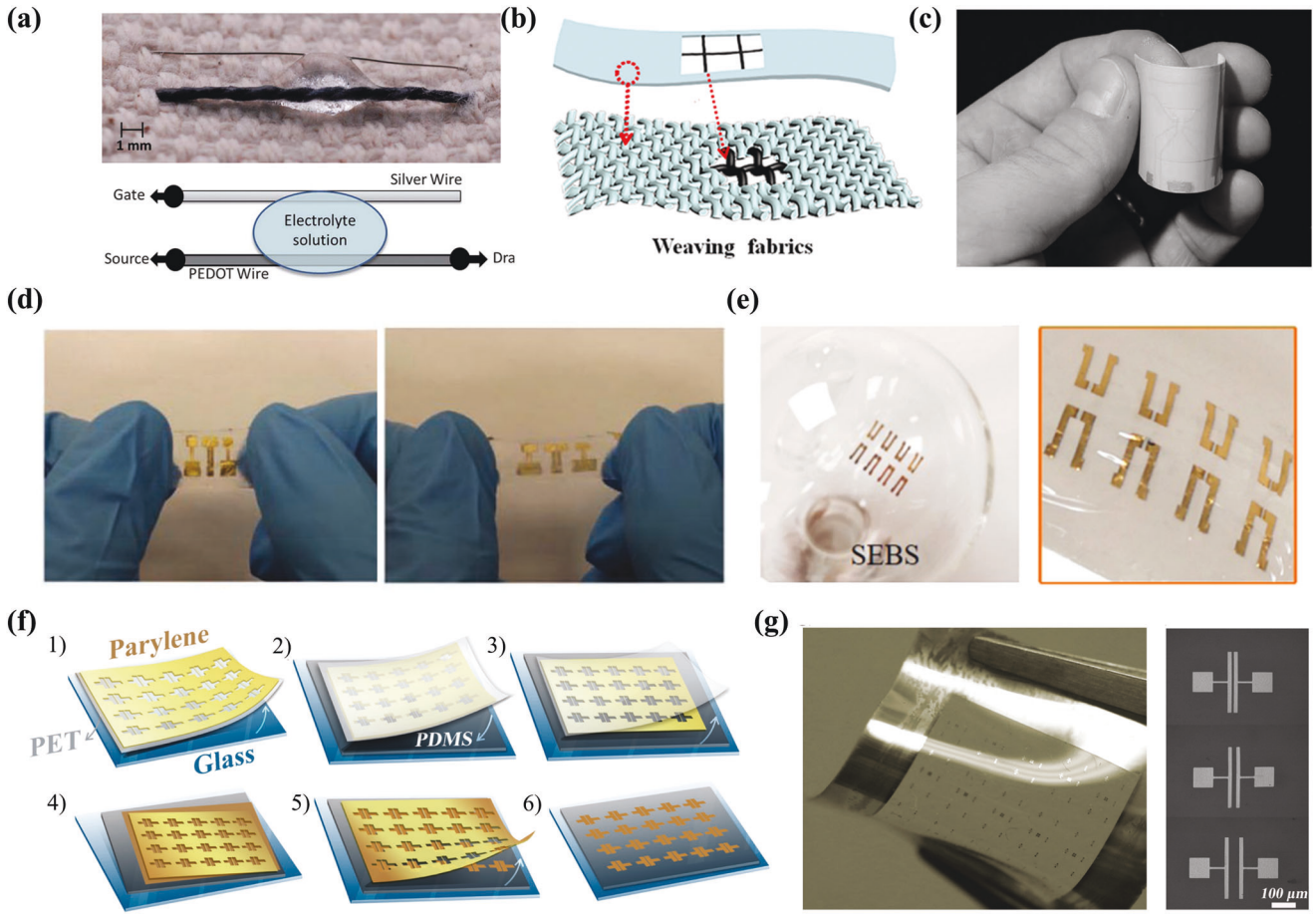

Figure 6. a–e) FSOECTs with low-cost fabric (a), fiber (b), paper (c), PDMS (d), and SEBS (e) as substrates. a) Reproduced with permission.[171] Copyright 2012, Royal Society of Chemistry. b) Reproduced with permission.[174] Copyright 2019, American Chemical Society. c) Reproduced with permission.[125] Copyright 2002, Elsevier. d) Reproduced with permission.[175] Copyright 2019, Wiley-VCH. e) Reproduced with permission.[176] Copyright 2020, American Chemical Society. f) Parylene transfer process for fabricating microelectrode arrays on PDMS substrate. g) PDMS substrate patterned with Au microelectrodes (15 mm × 15 mm) and the channel lengths of Au microelectrodes are 5, 20, and 50 μm, respectively. f,g) Reproduced with permission.[177] Copyright 2020, American Chemical Society.

substrates used in FSOECTs are low-cost fabric (**Figure 6**a), fibers (Figure 6b), and even paper (Figure 6c).[125,171–173]

In order to improve the flexibility and achieve stretchable OECTs, stretchable substrates such as PDMS (Figure 6d)[175] and styrene–ethylene–butylene–styrene (SEBS) (Figure 6e),[178,179] have also been adopted. However, high resolution patterning of electrodes and channel materials on these substrates is challenging due to their ultrasoft surface. Thus, for example, a transfer patterning process was proposed by Cicoira and co-workers[177] to fabricate high-resolution metal microelectrodes on PDMS (Figure 6f). Here, a thin parylene film (2 μm) was deposited on a PET film attached on a glass substrate. Next a parylene-based shadow mask was fabricated on this platform by photolithography and reactive ion etching. The resulting PET/parylene mask film was attached to the PDMS film and the PET film was removed leaving the parylene mask laminated to the PDMS film. After Au deposition by E-beam evaporation, Au electrodes with a channel length as low as 5 μm and excellent geometry control were obtained on the PDMS substrates by peeling off the parylene layer (Figure 6g).

Finally, since OECT operation involves electrolyte ions entering/exiting the channel material, material challenges remain for devices based on current flexible/stretchable substrates. For instance, the swelling/contraction of the channel material upon operation can compromise the adhesion between the substrate and channel material. This problem can result in debonding of channel material from the substrate, such as often occurs for PEDOT:PSS OECTs when operated in physiologically relevant environments.[180] Thus, future studies must also address promoting adhesion between the substrate and supported device components.

4.1.2. Semiconductor Channel Materials

The most commonly used channel material for FSOECTs used in physiological sensing is PEDOT:PSS, due to commercial availability, high ionic and electronic mobilities, "hydrogel" type nature in aqueous solution, and superior biocompatibility with biological environments. The typical approach to

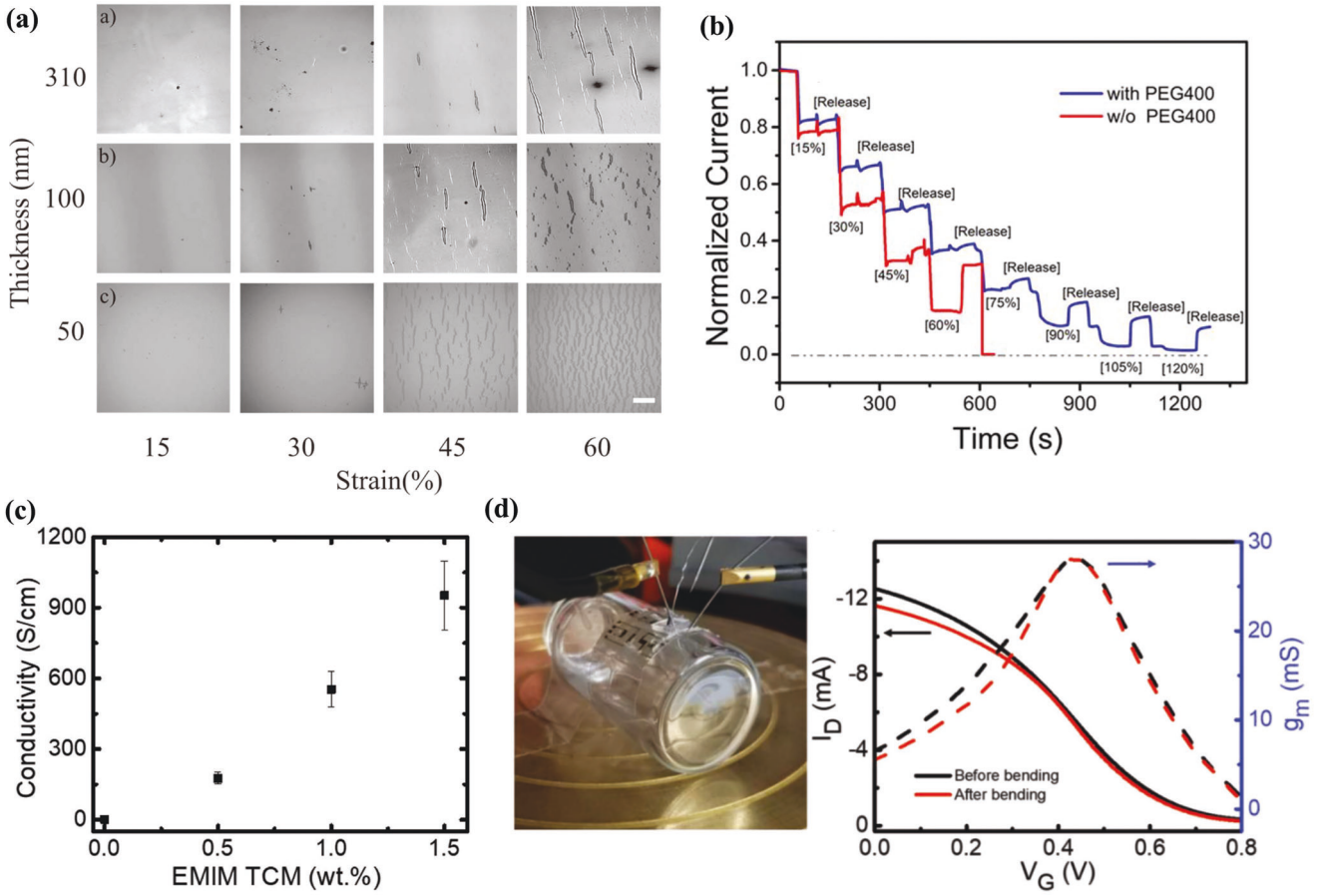

Figure 7. a) Optical images of ≈300 nm-thick PEDOT:PSS/PEG, ≈100 nm-thick PEDOT:PSS/PEG, and ≈50 nm-thick PEDOT:PSS (from top to bottom) films on PDMS under different strains. b) Normalized current vs time for different elongation strains for PEDOT:PSS/PEG hybrid and pristine PEDOT:PSS films on PDMS. a,b) Reproduced with permission.[185] Copyright 2021, IOP Publishing. c) Conductivity of PEDOT:PSS films with different concentrations of [EMIM][TCM]. d) Bending test (R = 11 mm) of a PEDOT:PSS/[EMIM][TCM] OECT array on a flexible PAR substrate and the corresponding transfer curves before and after bending. c,d) Reproduced with permission.[186] Copyright 2018, Wiley-VCH.

increase the deformability of PEDOT:PSS is to incorporate electronically insulating additives such as nonionic surfactant (e.g., Triton X-100),[181] ionic liquids (ILs, e.g., 1-butyl-3-methylimidazolium tetrafluoroborate),[182,183] and cosolvents (e.g., dimethyl sulfoxide).[184] Thus, a trade-off between enhanced PEDOT:PSS deformability upon blending and possible reduction of ionic/electronic transport efficiency must be considered for constructing high performance OECTs. For instance, Cicoira and co-workers[185] found that adding low-molecular weight poly(ethylene glycol) (PEG), as well as 5 v/v% glycerol and 1 v/v% Capstone, could effectively prevent the formation of cracks in PEDOT:PSS films while retaining a high electrical conductivity of ≈450 S cm^{-1}. Thus, when applying elongation strains as large as 45% and 60%, short and sparse cracks were found in the PEG-added PEDOT:PSS film, while much more severe cracks were observed for the bare PEDOT:PSS film (**Figure 7**a). Thus, the low crack density in PEG-added PEDOT:PSS leads to a small current variation between the stretched and released states (Figure 7b), which indicates that PEG addition significantly improves the mechanical robustness of the PEDOT:PSS film and device.

Addition of ILs to the channel semiconductors has also been explored considering their good chemical stability, wide electrochemical window, and high ionic conductivity as well as, specifically for PEDOT:PSS, can p-dope the polymer and promote formation of a fibrillar network structure enhancing charge transport concomitantly greater mechanical deformability. Leong and co-workers[186] proposed an IL (1-ethyl-3-methylimidazolium tricyanomethanide, [EMIM][TCM])-doped PEDOT:PSS, as the channel material of an OECT using a NaCl aqueous solution as the electrolyte. An electronic conductivity as high as 1000 S cm^{-1} was obtained when the IL concentration was 1.5 wt% (Figure 7c). Due to the plasticizer effect of the IL, the device fabricated on a flexible polyarylate (PAR) substrate exhibited stable performance under a bending radius (r) of 11 mm (Figure 7d), and the loss of channel current was only about 1% when r was 5 mm.

4.1.3. Electrodes

The breakdown of FSOECTs mainly originates from the failure of the source/drain electrodes due to crack formation under large strains.[187,188] Hence, it is critical for the electrodes to retain a high, and possibly stable, conductivity under strain. Conventional metal pads made of Au or Pt exhibit good electrical

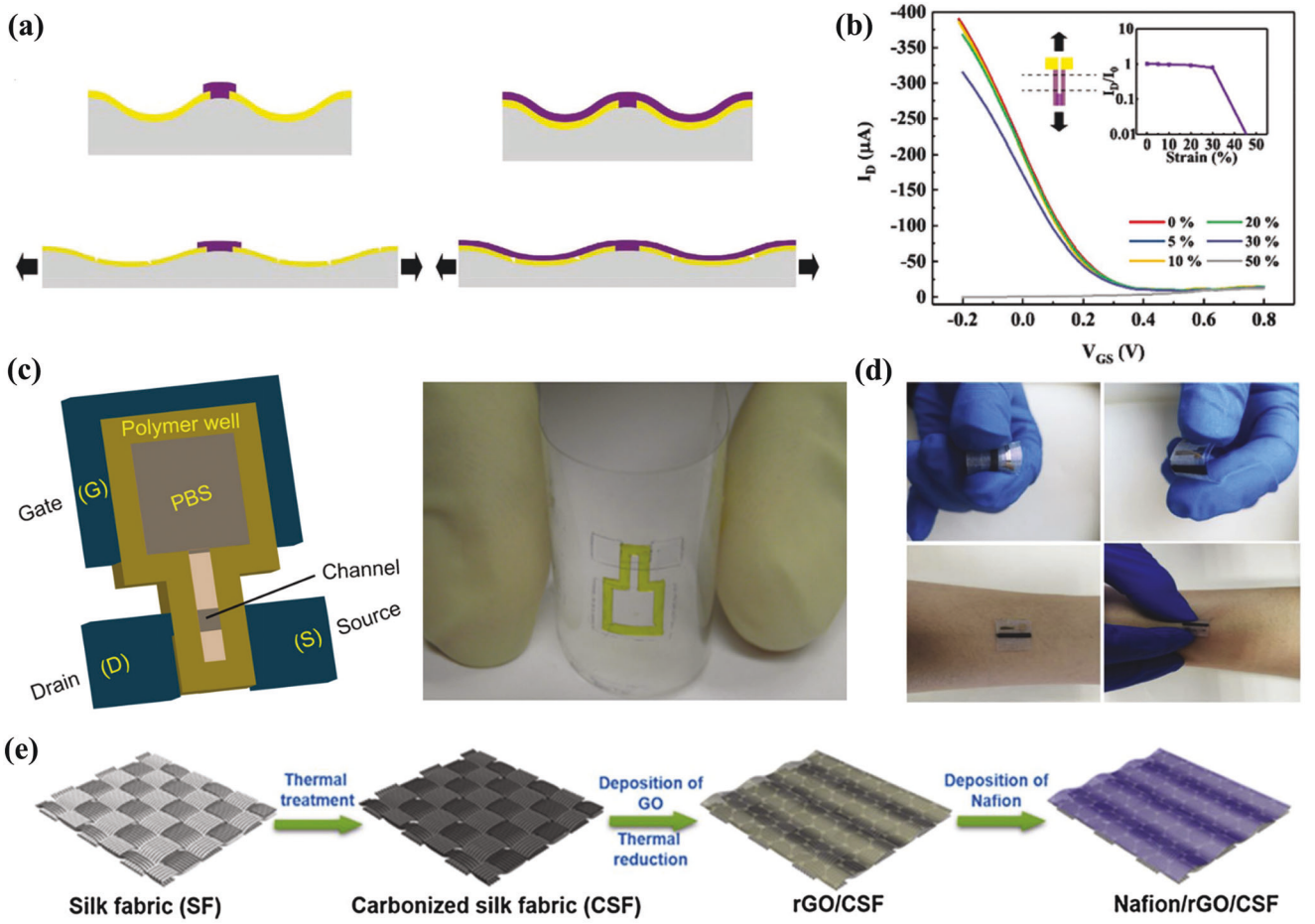

Figure 8. a) Schematic diagram of structural differences for normal (left) and PEDOT:PSS-coated (right) stretchable OECT. Dashed lines indicate cracking. b) Transfer characteristics of PEDOT:PSS-coated stretchable OECT under vertical strains, the inset showing the relative current change. a,b) Reproduced with permission.[175] Copyright 2019, Wiley-VCH. c) Schematic illustration of an all-PEDOT:PSS OECT (left), and the image of device fabricated on flexible polyester sheet (right). Reproduced with permission.[189] Copyright 2011, Elsevier. d) Photographs of the flexible OECT with carbon-cloth-based gate electrode, and e) the fabrication process of gate electrode. d,e) Reproduced with permission.[190] Copyright 2020, Elsevier.

conductivity and enable excellent performance when employed as electrodes in OECTs. However, the poor mechanical deformation properties of planar metal films remains the primary obstacle for the realization of mechanically stable FSOECTs. It has been reported that creating hybrid electrodes by depositing a highly conductive PEDOT:PSS film on metal structures can not only decrease the electrical resistance but also increase flexibility. Thus, in a study led by Yan and co-workers,[175] Au electrodes were first deposited on a PDMS substrate with a wavy surface, next a PEDOT:PSS film was coated on both the channel and the electrode areas resulting in hybrid Au–PEDOT:PSS source/drain electrodes (**Figure 8**a). Since PEDOT:PSS deformability is greater than that of bulk metals, it can provide conductive paths bridging disconnected Au pieces. Thus, these OECTs exhibit stable channel current response (Figure 8b) up to a maximum 20% vertical strain (elongation force is perpendicular to channel length direction), while the performance of the normal OECT (only a small part of Au electrodes was covered by PEDOT:PSS) falls rapidly at a 10% strain. Furthermore, DeCoster and co-workers[189] fabricated OECTs with PEDOT:PSS as electrodes and channels on a flexible polyester substrate and demonstrated satisfactory performance (Figure 8c). In this work, a patterned PI tape was used as a physical mask to define the PEDOT:PSS channel versus the PEDOT:PSS serving as source and drain electrodes. Note, a polymer reservoir with a thickness of 0.6 mm was attached to the device to constrain the location of the electrolyte. In a different approach, Liu and co-workers[190] utilized a flexible carbon cloth as the gate electrode of high performance FSOECTs. This high conductivity and deformable electrode was made of Nafion and reduced-graphene-oxide (rGO)-wrapped carbonized silk fabric (Figure 8d) which was obtained after thermal annealing at 900 °C under nitrogen (Figure 8e). For device fabrication, the fabric was directly adhered to a flexible PEN substrate as a planar gate electrode with deposited Au source/drain electrodes to construct flexible OECTs, the PEDOT:PSS was coated as the channel material. The mechanical stability of this device was evaluated, and the changes of transfer characteristics are negligible after continuous bending of 1000 times. Furthermore, this OECT was also utilized to detect dopamine, and the authors found that the sensing performances are retained in the bent state. These results demonstrated

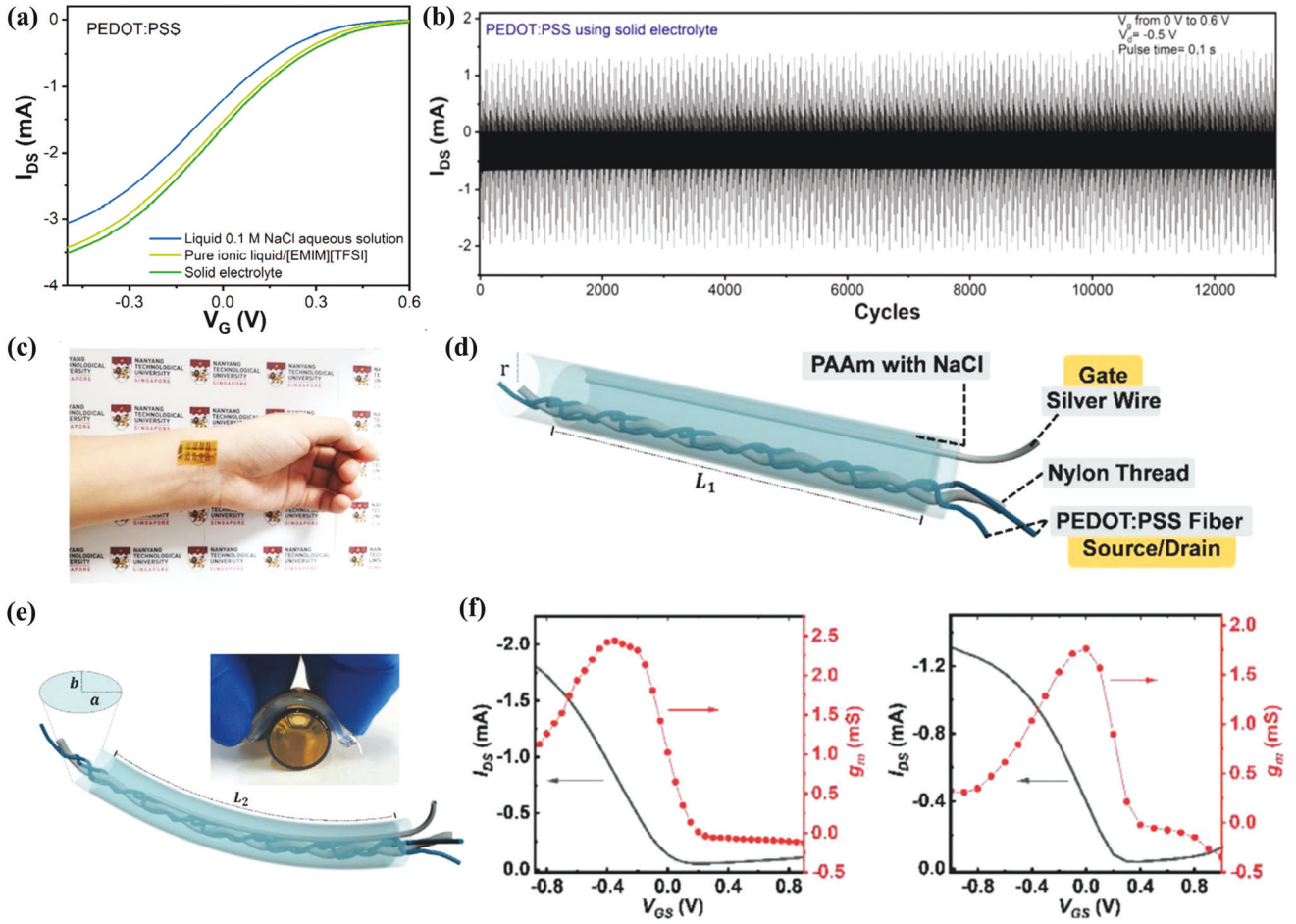

Figure 9. a) Transfer curves of PEDOT:PPS-based OECTs in different types of electrolytes (NaCl aqueous solution, IL, and ion gel). b) Cycling stability of the PEDOT:PSS-based OECT with an ion gel as the solid electrolyte. c) Image of a flexible OECT with an ion gel electrolyte for wearable sensing. a–c) Reproduced with permission.[193] Copyright 2020, Wiley-VCH. d,e) The schematic diagram and image of an all-solid-state fibrous OECT before (d) and after (e) bending. f) The transfer curves of the all-solid-state fibrous OECT before (left) and after (right) bending. d–f) Reproduced with permission.[195] Copyright 2021, Wiley-VCH.

the excellent mechanical resistance of flexible-OECT-based sensors based on carbon cloth.

4.1.4. Electrolyte

The electrolyte plays a critical role in OECT performance since ions are required for the redox chemistry to occur in the OECT channel.[70,167] The most employed electrolytes used in OECTs have been NaCl aqueous and phosphate-buffered saline (PBS) buffer solutions. OECTs used for in vivo and in vitro sensing applications require the development of electrolytes with large electrochemical window of operation, high ionic conductivity, and nonvolatile properties. For this reason, IL or IL-based mixtures have been widely used as the electrolyte for OECT-based biosensors.[191,192] However, the use of liquid electrolytes in FSOECTs can be problematic due to the electrolyte fluid nature. Thus, semisolid electrolytes such as ion gels, consisting of IL cross-linked into polymeric matrices and hydrogels, are preferred. Most importantly, the excellent mechanical resistance of gel electrolytes to severe deformations is a plus for biosensing applications of FSOECTs.

As an example, Leong and co-workers[193] utilized an elastomeric ion gel consisting of poly(vinylidene fluoride-*co*-hexafluoropropylene) ionic conductive polymer and the IL 1-ethyl-3-methylimidazolium bis(trifluoromethylsulfonyl)amide ([EMIM][TFSI]) as the solid electrolyte for OECTs. In this work, an all-solid PEDOT:PSS-based OECT was fabricated using Au as the source/drain electrodes, and by modifying the ion gel solid electrolyte on a Au gate electrode deposited on a PI film and then laminating the film on the channel area, in which the side of the ion gel was contacting the channel surface. This device exhibited comparable electrical performance (transfer characteristics) with the one operated with a NaCl aqueous solution or the pristine IL (**Figure 9**a), as well as excellent long-term stability (Figure 9b). Furthermore, the ion gel electrolyte could be patterned with a needle-shape microstructure and used for constructing flexible-OECT-based pressure sensors. In this case, the ion penetration from the solid electrolyte to the channel is controlled by the contact area between the electrolyte and PEDOT:PSS channel

material, which allows for precise detection of the wrist artery pulse in wearable sensing (Figure 9c). Since some ILs used in ion gels can be toxic to biosystems when the device is in direct contact with the tissue,[167,194] biocompatible hydrogels are excellent alternatives. Zhang et al.[177] prepared a polyacrylamide (PAAm)-based stretchable hydrogel containing NaCl and used it as the solid electrolytefor prestretched PEDOT:PSS-based OECTs. These devices can withstand a tensional stress up to 30%, however higher stresses will result in cracking of the PEDOT:PSS layer while the hydrogel remains intact. Additionally, Wang and co-workers[195] used a PAAm–NaCl hydrogel in constructing an all-solid-state OECT based on PEDOT:PSS fibers. As shown in Figure 9d, two cross-wound PEDOT:PSS fibers used as the source/drain electrode and a silver wire serving as the gate contact were located parallelly in a PET tube, and the PAAm–NaCl hydrogel was filled and thus functioned as the electrolyte. Note, the channel in this device is defined by the overlap area between the two fibers near the contact point. Thus, one contact point and its adjacent area can be regarded as a single OECT, and many individual devices are connected in parallel through the PEDOT:PSS fibers. Since the stretchable PEDOT:PSS fiber prepared in this work has shown a maximum tensile strength of ≈131 MPa and a crack onset of ≈31%, the fiber-based OECT maintained good electrical performance with a slight decrease of g_m from 2.44 to 1.76 mS after bending on a bottle surface (Figure 9e,f).

However, the evaporation of hydrogel water can pose issues for their long-term use. Thus, hydrogels based on nonvolatile glycerols have been developed, exhibiting far more stable performance.[196] Although gel electrolytes have been key in the progress of FSOECTs, obstacles remain for application in chemical signal biosensing. For example, the slow mass transfer process and reaction rates in solid electrolyte reduce the speed and efficiency of OECT-based sensors toward analytes.[197]

4.2. Device Engineering

Engineering of the OECT architecture is another important way to improve the flexibility and stretchability of these devices with the design of electrodes and substrates being the most investigated strategies. Thus, electrodes with fabric (**Figure 10**a),[198] serpentine (Figure 10b),[199] mesh-shaped (Figure 10c),[58] and honeycomb-shaped (Figure 10d)[200] structures can substantially enhance electrical contact deformability. Even though the above designs are effective in preventing crack generation, the Young's modulus mismatch between the electrode and the semiconductor layers can lead to rapid device performance degradation due to crack formation in the channel or delamination between the two layers.[201,202]

To address this problem, Someya and co-workers[200] proposed a stretchable PEDOT:PSS-based OECT array with honeycomb Au electrodes (Figure 10d) having the channel area defined on the side length of each hexagonal electrode unit. The device was freestanding in a PBS electrolyte using an ultrathin parylene film (1.2 μm) as the substrate and encapsulation layer. In this novel design, the channel area was no longer a main stress node when the device was stretched since the honeycomb electrode network functioned as the main stress-bearing component. The transfer curves of these devices upon mechanical deformation indicate that I_{DS} and g_m remain stable up to an elongation strain of 15% (Figure 10e). Moreover, after 1000 operation cycles at a 15% elongation strain, I_{DS} and g_m decrease only by ≈7%, indicating excellent mechanical durability.

Engineering the crack itself is another way to improve electrode stretchability since studies have revealed that premade microcracks in metal electrodes greatly stabilize performance upon mechanical deformation.[203–205] As an example, Chen and coworkers[187] reported more stretchable Au electrodes by creating "long initial microcracks" (>8 μm) in the evaporated Au film (**Figure 11**a). Compared to Au electrodes having "short initial microcracks" (<2 μm), suppressed stress concentration at the tip of cracks and effective stress relaxation in the surrounding area were observed for the longer microcracks. Thus, while application of a strain to Au electrodes with short microcracks led to microcracks propagating across the entire film, disrupting conducting pathways, most of the strain in the Au electrodes with long microcracks only widened the long microcracks, thereby preserving the conducting pathways. The morphology of microcracks was controlled by simply adjusting the evaporation rate and film thickness during electrode fabrication. Based on this strategy, these OECTs remained functional under a 140% elongation strain (with a transconductance as high as 0.14 mS, which is much higher than those in previous stretchable transistors, Figure 11b). Note, I_{DS} and g_m gradually decrease at higher elongation strains due to deformation of the channel increasing the channel length.

Furthermore, constructing wavy structures on flexible/stretchable substrates by prestretching or transfer printing is another simple and remarkably effective strategy to enhance stretchability.[175,177] For example, Cicoira and co-workers[177] prestretched a PDMS substrate by 30% of the initial length, which is about the maximum strain the human skin can sustain. For device fabrication, a PEDOT:PSS channel layer and Au source/drain electrodes were patterned on the prestretched PDMS substrate by transfer printing, which resulted in a stretchable OECT after releasing the prestrain. A polyacrylamide-based stretchable hydrogel containing NaCl and a planar PEDOT:PSS layer were used as the solid electrolyte and gate contact, respectively. These devices show little variation of the electrical performance under a perpendicular strain up to 30% (Figure 11c,d), which is far more stretchable than the devices fabricated without prestretching the substrate (<5%).

Engineered device structures having wrinkled geometries capable of dissipating stress energy are also suitable for channel materials, however, the complex fabrication process and decreased material loading density has hindered this strategy.[206,207] In this regard, our group[138] demonstrated an effective material design concept in FSOECTs by constructing an organic semiconductor film with a regular honeycomb porous structure. The porous channel film fabrication is shown in **Figure 12**a, to achieve a regular honeycomb film morphology, the amphiphilic polymer poly(2,5-bis(2-octyldodecyl)-3,6-di(thiophen-2–yl)-2,5-diketo-pyrrolopyrrole-*alt*-2,5-bis(3-triethyleneglycoloxy-thiophen-2-yl) (DPP-g2T) was dissolved in chloroform/methanol (v/v = 9:1), and the solutions were spin-coated on ≈20 nm-thick poly(vinyl alcohol) (PVA) sacrificial layers on ultrathin (≈0.13–0.17 mm) glass substrates in an environmental chamber maintained at 90% relative

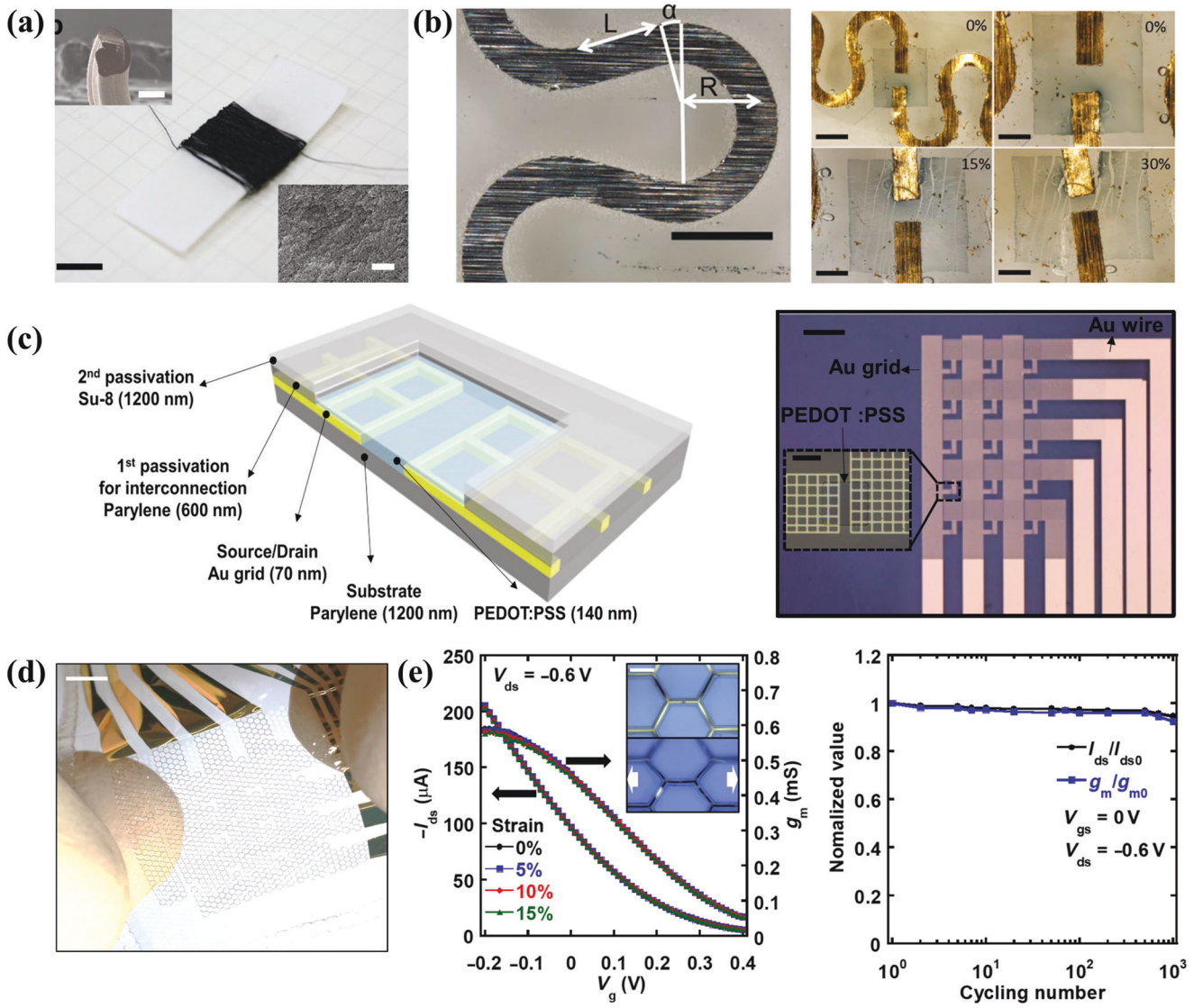

Figure 10. a–d) Flexible and stretchable OECTs with fiber (a), serpentine (b), mesh-shaped (c), and honeycomb-shaped (d) electrodes. e) Transfer curve and g_m of single OECT unit with honeycomb-shaped electrode after 0%, 5%, 10%, and 15% stretching (left). Insets are microscopy images of OECT under 0% (top) and 10% (bottom) stretching strains, where the channel width and length are 10 and 15 mm, respectively. The variations of normalized channel current (I_{DS}) and g_m at V_{GS} = 0 V after stretching at 15% after different cycles (right). a) Reproduced with permission.[198] Copyright 2018, Spinger Nature. b) Reproduced with permission.[199] Copyright 2018, Springer Nature. c) Reproduced with permission.[58] Copyright 2017, National Academy of Science. d,e) Reproduced with permission.[200] Copyright 2018, American Association for the Advancement of Science.

humidity, after water immersion, the freestanding honeycomb films (h-films) (Figure 12b) were transferred to the substrate for further device integration. The mechanical properties of the OECTs based on h-films and conventional dense films were compared using SEBS as the substrates, Au source–drain electrode, an aqueous KPF_6 electrolyte, and a Ag/AgCl gate electrode (Figure 12c). OECTs with dense channel films (defined as d-DPP-g2t) showed a rapid decrease of g_m when stretching above a 30% strain and cannot recover to the initial performance after the strain was released due to macroscopic crack formation. In contrast, OECTs with h-films (defined as h-DPP-g2t) retained a respectable performance until stretched to a 120% strain, demonstrating the superior mechanical stability of honeycomb structures. Then, to further improve the stretchability of OECT by forming wrinkled geometries, the SEBS substrates were biaxially stretched before Au source–drain electrode deposition and h-film transfer. Thus, the prestretched OECT (100% pre-stretched) performance was monitored over stretching cycles with tensional strains applied along directions parallel or perpendicular to channel length from 0% to 30% (Figure 12d), and showed excellent mechanical robustness, with a maximum g_m degradation of 13% or 8% after 1000 stretching cycles and ≈27% or 20% after 10 000 stretching cycles, respectively, attributed to the metal contact fatigue. The same group is now exploring this approach in combination of a recently discovered vertical OECT architecture.[208]

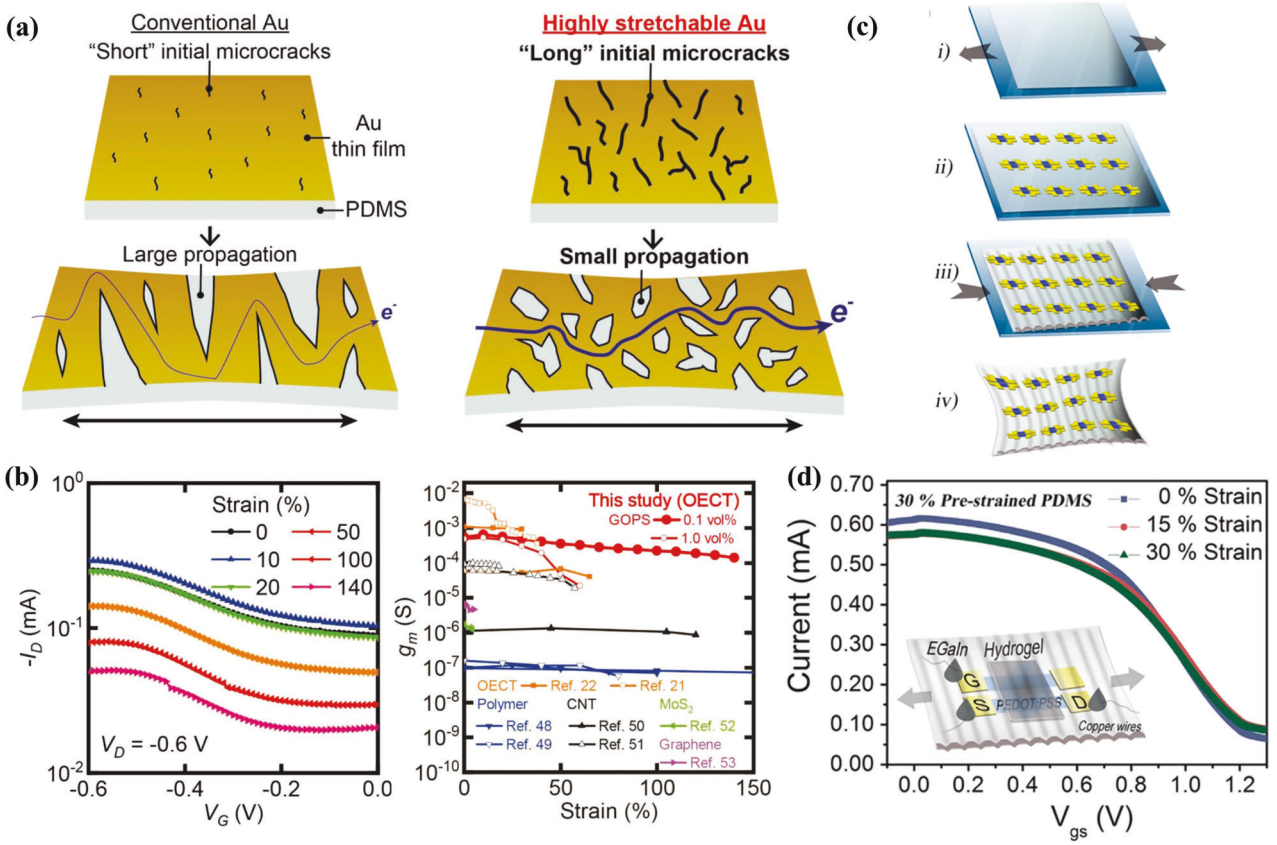

Figure 11. a) Schematics of the crack propagation for a conventional Au film with short initial microcracks (left) and a highly stretchable Au film with long initial microcracks (right) under strain. b) Transfer curves of highly stretchable OECTs under different strains, and comparison of the maximum g_m variations to previous reported stretchable OECTs. a,b) Reproduced with permission.[187] Copyright 2019, Wiley-VCH. c) Scheme of the stretchable OECT fabrication process on 30% prestretched PDMS substrate, and d) transfer curves of the OECTs under 0%, 15%, and 30% strains. c,d) Reproduced with permission.[177] Copyright 2017, American Chemical Society.

5. Physiological Sensing by OECTs

The main motivation for developing FSOECTs in recent years is for applications in physiological sensors, including chemical signal sensing of human metabolites and real-time monitoring of electrical physiological activities.[56,189,197,209] Most of the pioneering studies mainly addressed the detection mechanism neglecting mechanical compliance, stability, and accessibility for applications in real scenarios. However, during the past five years, some studies were devoted to understand and enhance the mechanical flexibility and even stretchability of OECT-based sensors for integration with various biological surfaces.[55,179,210–214] Additionally, fully integrated wearable sensors based on OECTs have been proposed based on emerging application demands consisting of multifunctional modules combining energy supply and data processing.[215–217] In this section, divided into different types of sensors, first we discuss seminal OECT research carried out on rigid platforms for biochemical and bioelectrical sensing followed by progress using FSOECT sensors.

5.1. Biochemical Sensors

Monitoring of biochemical signals based on detection and quantification of ions, pH, glucose, other common metabolites, and biomarkers of biological systems can provide insight in health evaluation at the molecular level.[218,219] Moreover, biochemical signal sensing, which usually operates in various body fluids, plays an essential role in disease diagnosis, drug abuse detection, and athletic performance optimization.[220,221] The latest advances in FSOECTs applied to biochemical sensors are summarized in **Tables 2–5**, based on the classification of the detection targets.

5.1.1. Ion and pH Sensors

Ion concentration and pH value are among the most important physiological parameters of a biological system providing information on the status of hydration and fatigue.[234] OECTs can be extremely sensitive to the fluctuation of ionic concentration in the electrolyte, which makes them a useful tool for sensing ions and pH.[61,125] Wrighton and co-workers[122] first demonstrated the use of a rigid OECT with a polyaniline (PANI) channel material for the direct detection of small changes of pH and redox ions, such as $Ru(NH_3)_6^{3+/2+}$ and $Fe(CN)_6^{3-/4-}$, in aqueous electrolyte solutions. The direct chemical sensing is achieved by the reactions between the analytes and the PANI, which further result in a change to the chemical state (electronic conductivity)

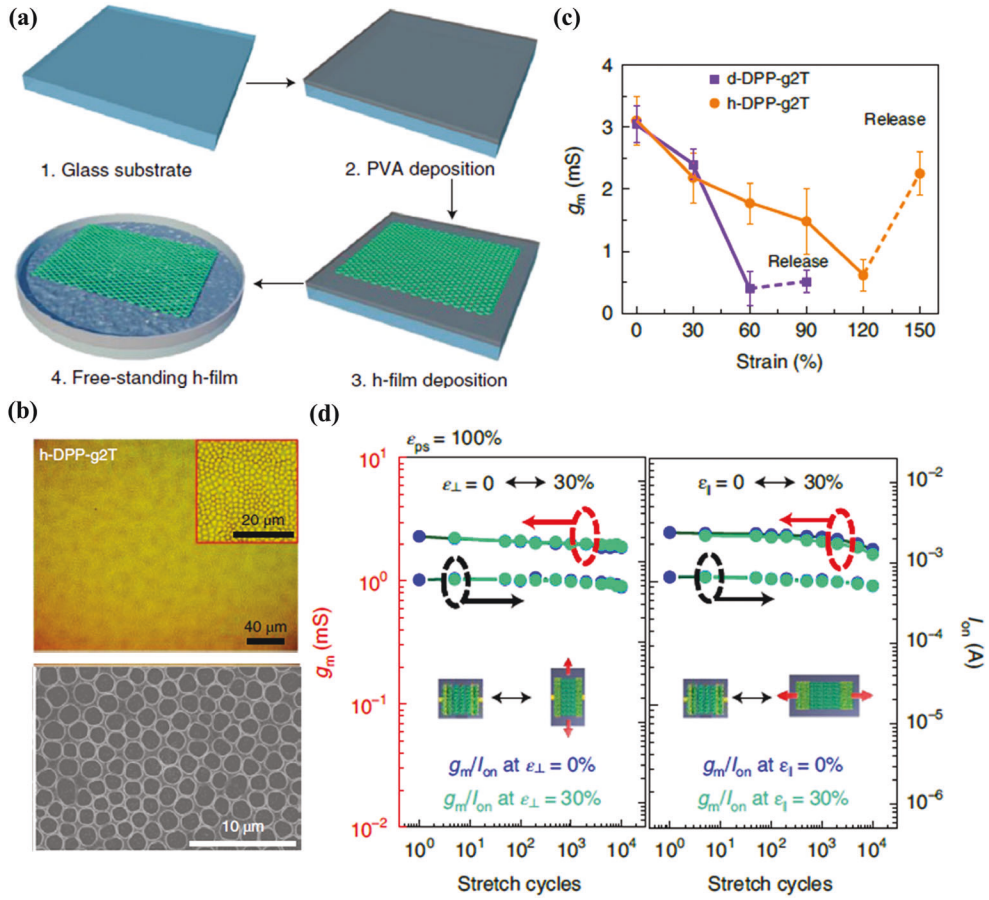

Figure 12. a) Schematic of the fabrication process of channel films with honeycomb structures: spin-coating PVA sacrificial layer (step 2) and then depositing h-film on PVA (step 3); PVA dissolution by water immersion to yield freestanding films. b) Optical microscopy (top) and scanning electron microscopy (SEM) (bottom) images of h-film. The inset shows a zoomed-in view of the images. c) Transconductance (g_m) for OECTs based on h-film (h-DPP-g2T) and dense film (d-DPP-g2T) under different strains (symbols with error bars indicate variation over five test samples). d) The g_m and I_{on} dependence on stretching cycles for prestretched OECTs (prestretched strain: 100%) in the directions parallel or perpendicular to channel length, where g_m and I_{on} under 0% and 30% elongation strains are recorded. Insets indicate stretching directions. a–d) Reproduced with permission.[138] Copyright 2022, Springer Nature.

of the PANI. The large change in electronic conductivity of PANI with variation in the electrochemical potential is at the basis of this device function. Thus, the device can be turned-on/off by the chemical signals in electrolyte that oxidize/reduce the PANI.

Although OECTs can achieve high ion sensitivities, they typically lack ion selectivity, which is essential for ion sensing in complex environments. To increase the detection selectivity, Dabke et al.[126] incorporated 18-crown-6 ethers into the a PANI film serving as the channel material of an OECT device. With this platform, it was possible to selectively detect very low concentrations (≈10^{-8} M) of K^+ owing to the specific interaction between 18-crown-6 and K^+. The transistor response was attributed to the conformational changes of the PANI backbone induced by the high local electrostatic field of the bounded metal ion in the crown cavity of polymer.

A very effective method to achieve high selectivity is by introducing ionophore-based ion-selective membranes (ISMs), which are able to selectively exchange ions in the gate electrolyte of interest.[235,236] Berggren et al.[237] coated an ISM for Ca^{2+} on top of the PEDOT:PSS channel of an OECT to obtain an ion-selective organic electrochemical transistor. The channel area coated by the Ca^{2+} ISM was immersed in an aqueous solution of different $CaCl_2$ concentrations and 0.1 M KCl as the background electrolyte. The response curves of the channel current for different Ca^{2+} concentrations (with a constant background electrolyte of 0.1 M KCl) were tested by applying a gate voltage pulse of 0.15 V, the channel current decreases from 29.5 to 27.5 μA on increasing the Ca^{2+} concentration from 10^{-4} to 10^{-1} M.

To further understand the device physics of OECT ion sensors, Yan and co-workers[238] investigated how the cation (K^+, Ca^{2+}, and Al^{3+}) concentration and gate electrode (Pt, Au, Ag/AgCl) materials affect the sensing operation of a PEDOT:PSS-based OECT. This device was placed into aqueous solutions of cations with different concentrations (0.001, 0.01, 0.1, and 0.3 M) (**Figure 13**a) and the results of the transfer curves indicated that higher cation concentration reduced depletion mode and the gate voltage shift of the transfer curves showed a logarithmic dependence

Table 2. FSOECTs for ions and pH sensors.

Analyte		Substrate	Source/drain	Gate	Electrolyte[a]	Channel material	Flexibility/stretchability	Detection range	Refs.
Ions and pH	pH K^+	PLA[b]/PET[c]	Silver paste	Ag/AgCl probe	PBS KCl	PEDOT:PSS	N/A	2.28–7.55 1–1000 mM	[163]
	Na^+	Cotton fiber	Cotton fiber/PEDOT:PSS	Ag wire	NaCl	PEDOT:PSS	N/A	0.1–100 mM	[171]
	Na^+	PAR[d]	Au	Ag/AgCl probe	NaCl	PEDOT:PSS/[EMIM][TCM][e]	Bending radius: 5 mm	0.001–1000 mM	[186]
	Ions in plant sap	Textile fiber	Textile fiber/PEDOT:PSS	Ag wire	Plant sap	PEDOT:PSS	N/A	N/A	[172,222]
	Cations in sweat	None	PEDOT:PSS/silver wire	–	Sweat	PEDOT:PSS	N/A	0.1–1000 mM	[198]
	NH_4^+ Ca^{2+}	SEBS[f]	Ag/AgCl paste	Ag/AgCl paste	Artificial sweat	PEDOT:PSS	N/A	0.01–100 mM 0.01–100 mM	[178]
	Na^+ Ca^{2+} K^+	PET[c]	Silver paste	Ag/AgCl probe	$CaCl_2$ NaCl KCl	PEDOT:PSS	N/A	1–10/10–1000 mM	[223]
	K^+	Cotton fiber	Cotton fiber/MWCNT[g]/PEDOT	Cotton fiber/MWCNT[g]/PEDOT/K^+ selective membrane	KCl	PEDOT:PSS	Fracture elongation: 42 ± 1%	0.000005–0.001 mM	[224]
	Na^+ Ca^{2+} K^+	PI[h]	Au	Ag/AgCl paste	$CaCl_2$ NaCl KCl	PEDOT:PSS	Bending radius: 1.1 mm	0.001–100 mM 0.001–100 mM 0.001–100 mM	[165]

[a] All electrolytes are aqueous solutions unless indicated; [b] Poly(lactic acid); [c] Poly(ethylene terephthalate); [d] Polyarylate; [e] 1-Ethyl-3-methylimidazolium tricyanomethanide; [f] Styrene–ethylene–butylene–styrene; [g] Multiwalled carbon nanotubes; [h] Polyamide.

Table 3. FSOECTs for glucose sensors.

Analyte		Substrate	Source/drain	Gate	Electrolyte[a]	Channel material	Flexibility/stretchability	Detection range	Ref.
Glucoses	Glucose	PEN[b]	Au	PEDOT:PSS	PBS	PEDOT:PSS	N/A	0.0234–2 mM	[164]
	Glucose	Polyester sheet	PEDOT:PSS	PEDOT:PSS	PBS	PEDOT:PSS	N/A	0.001–10 mM in PBS 0.008–0.21 mM in human saliva	[189]
	Glucose	PEN[b]	Au	Au/PEDOT:PSS/Pt NP[c]/chitosan/GOx[d]	PBS; CIB[e]	PEDOT:PSS	N/A	0.01–0.7 mM in PBS and CIB[e]0.01–0.3 mM in CS[f]	[132]
	Glucose	PET[g]	Pt	Pt/Nafion–graphene/PANI[h]/GO[i]–GOx[d]	PBS	PEDOT:PSS	N/A	N/A	[65]
	Glucose	PA6 fiber	PA6 fiber/rGO[j]/PPy[k]	PA6 fiber/rGO[j]/PPy[k]/Nafion/GOx[d]	PBS	PPy[k]	Breaking stress: 0.10 N tex^{-1}; breaking strain: 53 ± 4%	0.000001–0.005 mM	[225]
	Glucose	Nylon fiber	Nylon fiber/Au	Nylon fiber/Pt/GOx[d]/chitosan/graphene flakes	PBS	PEDOT:PSS	Bending radius: 0.6 cm	0.00003–0.3 mM	[210]
	Glucose	PDMS[l]	Au	Au/Pt flakes/GOx[d]/chitosan	PBS	PEDOT:PSS	Bending strain: 30%; bending radius: 15 mm	0.001–0.611 mM	[175]
	Glucose	PET[g]	Ag	Ag	PBS	PEDOT:PSS	N/A	0.001–10 mM	[226]
	Glucose	Human skin	Au	Ag/AgCl probe	PBS	PEDOT:PSS	Stretching strain: 5%; compressing strain: 40%	0.000001–0.1 M	[133]
	Glucose	PI[m]	silver ink	Graphene/silver ink	PBS	PEDOT:PSS	N/A	0.03–5 mM	[227]

[a] All electrolytes are aqueous solutions unless indicated; [b] Poly(ethylene-2,6-naphthalate); [c] Pt nanoparticles; [d] GOx: glucose oxidase; [e] Chloroplast isolation buffer; [f] Inactive isolated chloroplasts solution; [g] Poly(ethylene terephthalate); [h] Polyaniline; [i] Graphene oxide; [j] Reduced graphene oxide; [k] Polypyrrole; [l] Poly(dimethylsiloxane); [m] Polyamide.

Table 4. FSOECTs for other metabolite sensors.

Analyte		Substrate	Source/drain	Gate	Electrolyte[a]	Channel material	Flexibility/stretchability	Detection range	Ref.
Other metabolites	Tyrosine	Cotton fiber	Cotton fiber/PEDOT:PSS/laccases	Pt wire	Sodium citrate buffer	PEDOT:PSS	N/A	0.0001–1 mM	[228]
	Cortisol	SEBS[b]	Ag/AgCl paste	Ag/AgCl paste	Artificial sweat	PEDOT:PSS	Stretching strain: 40%	0.0000001–0.5 mM	[179]
	Lactate	PI[c]	Au	Au/Pt/chitosan/LOx[d]	PBS	PEDOT:PSS	N/A	0.25–10 mM	[217]
	Lactate	Parylene	PEDOT:PSS	PEDOT:PSS	PBS	PEDOT:PSS	N/A	10–100 mM	[197]
	Lactate	PEN[e]	Au	PEDOT:PSS	PBS	PEDOT:PSS	N/A	0.1–2.3 mM	[164]
	Ethanol	Paper	PEDOT:PSS	PEDOT:PSS	Ethanol solution	PEDOT:PSS	N/A	0.0004–0.15 wt%	[173]
	Uric acid	PET[f]	Pt	Pt/Nafion–graphene/PANI[g]/GO[h]–UOx[i]	PBS	PEDOT:PSS	N/A	0.0001–0.5 mM	[65]
	Uric acid	Nylon fiber	Nylon fiber/Au	Nylon fiber/Pt/Nafion–graphene/PANI[g]/UOx[i]–GO[h]	PBS	PEDOT:PSS	Bending radius: 0.6 cm	0.00003–0.3 mM	[210]
	Urea	PET[f]	Ag ink	PEDOT:PSS	PBS	PEDOT:PSS	N/A	0.001–10 mM	[229]
	Dopamine	PA6 fiber	PA6 fiber/NFs[j]/PPy[k]	PA6 fiber/NFs[j]/PPy[k]	PBS	PPy[k]	N/A	0.0001–0.001 mM	[174]
	Dopamine Noradrenaline Adrenaline	PET[f]	Au	Pt	PBS	PEDOT:PSS	N/A	0.000001–0.001 mM0.000001–0.001 mM0.000001–0.001 mM	[131]
	Ascorbic acid Dopamine	PEN[e]	Au	NOCC[l]–R (H_2/Ar) NOCC[l]–O (O_2/Ar)	PBS	PEDOT:PSS	N/A	0.005–1 mM0.001–0.3 mM	[211]
	Dopamine	PEN[e]	Au	CSF[m]/rGO[n]/Nafion	PBS	PEDOT:PSS	N/A	0.000001–0.03 mM	[190]
	Dopamine	PI[c]	Au	Au/aptamer 1	Tris buffer	PEDOT:PSS	N/A	0.000000005–0.000001 mM	[230]
	Sialic acid	Cotton fiber	Cotton fiber/PDDA[o]/MWCNTs[p]/PEDOT:PSS fiber/PDDA[o]/MWCNTs[p]/PEDOT:PSS/APBA[q]	Cotton	PBS	PEDOT:PSS	N/A	0.000001–1 mM	[231]

[a] All electrolytes are aqueous solutions unless indicated; [b] Styrene–ethylene–butylene–styrene; [c] Polyamide; [d] Lactate oxidase; [e] Poly(ethylene-2,6-naphthalate); [f] Poly(ethylene terephthalate); [g] Polyaniline; [h] Graphene oxide; [i] Urate oxidase; [j] Poly(vinyl alcohol) (PVA)-*co*-polyethylene (PE) nanofibers; [k] Polypyrrole; [l] N/O-codoped carbon cloths; [m] Chloroplast isolation buffer; [n] Reduced graphene oxide; [o] Poly(diallyldimethylammonium chloride); [p] Multiwalled carbon nanotubes; [q] 3-Aminophenylboronic acid.

Table 5. FSOECTs for antibody/antigen-based biomarker sensors.

Analyte		Substrate	Source/drain	Gate	Electrolyte[a]	Channel material	Flexibility/stretchability	Detection range	Ref.
Antibody/antigen-based biomarkers	Cortisol	PI[b]	Au	Au/anticortisol antibody	PBS	PEDOT:PSS	N/A	0.000001–0.001 mM	[232]
	IgG	PET[c]	Au	Au/anti-IgG	PBS	PEDOT:PSS	N/A	0.000006–66 pM	[64]
	SARS-CoV-2 IgG[d]	PET[c]	Au	Au/SARS-CoV-2 spike protein	PBS	PEDOT:PSS	N/A	0.0000001–100 nM	[55]
	Human IgG	PET[c]	Au	ITO[e]/human IgG antibody	PBS	P3HT	N/A	7 000 000–70 nM	[233]

[a] All electrolytes are aqueous solutions unless indicated; [b] Polyamide; [c] Poly(ethylene terephthalate); [d] Severe acute respiratory syndrome coronavirus 2 immunoglobulin G; [e] Indium tin oxide.

to the ionic concentration (Figure 13b). This study also found that OECTs using a Pt or Au wire as the gate electrode for K^+ detection can achieve a higher sensitivity than the one with a Ag/AgCl gate electrode having an identical surface area. This result was attributed to the large C_{CH} of the metal gate/electrolyte interface, versus the negligible one at the Ag/AgCl gate electrode, due to the large Faradaic current at the interface (Figure 13c). Thus, higher gate voltage is needed to compensate for the potential change at the electrolyte–channel interface induced by the change in cation concentration. Furthermore, the authors demonstrated that the gate voltage shift with a metal gate is proportional to $(1 + C_{CH}/C_G)$, and thus it can be used for quantifying the ion concentration. The adoption of metals as the gate electrode is advantageous for improving ion detection sensitivities, simplifying OECT fabrication process, and developing miniaturized/integrated OECT-based sensors. However, the major limitation of these devices is the need of higher operating voltages (typically >0.75 V) to obtain high detection sensitivity, which could potentially compromise sensor stability.

Considerable research activities have addressed FSOECTs for ion and pH detection (Table 2). In particular, FSOECTs based on cotton could be suitable for wearable electronic fabrics. Coppedè and co-workers[171] proposed a single natural cotton fiber coated with PEDOT:PSS by a simple soaking process, and the PEDOT:PSS was used as the channel material, and the two fiber terminals served as the source/drain electrodes. The cotton-fiber-based FSOECT directly interfaced with the aqueous electrolyte in contact with a Ag wire gate, thus the OECT channel was defined by the region where the electrolyte overlaps the PEDOT:PSS film. This device exhibited stable and reproducible electrical performance. By measuring the channel current changes under different NaCl concentrations, it was demonstrated that the cotton-fiber-based FSOECT can efficiently detect the NaCl concentration in the physiological range of human sweat (2×10^{-2} to 8×10^{-2} M). Zappettini and co-workers[172,222] developed this concept further and fabricated cotton-fiber-based FSOECTs for in vivo sensing of sap ions in plants. These devices, consisting of a PEDOT:PSS-coated cotton fiber serving as both the channel and source/drain electrodes and a silver gate electrode, were integrated into the plant stem. With this configuration, the circadian pattern and effect of vapor pressure deficit in tomato plants were investigated by in situ monitoring the variation of the total cation concentrations.

The cotton-fiber-based FSOECTs are simple and low-cost ion sensors, nevertheless, the device flexibility proposed in the abovementioned work remains limited for developing wearable electronics due to the use of a metal wire gate. In this regard, Wang and co-workers[239] developed a FSOECT with a cross-junction-fiber-based configuration for Pb^{2+} detection. As shown in **Figure 14**a, nylon fibers incorporating polypyrrole (PPy) and PVA-*co*-polyethylene nanowires, formed by in situ polymerization, were used as the channel, spatially localized by the overlap between the two fibers, and the source/drain/gate electrodes of an OECT. The final device was completed by forming a cross-junction between two fibers and integrating a solid-state electrolyte consisting of a PV + HCl mixture. The larger surface area and aspect ratio of the nanofibers lead to a large number of interconnected PPy channel areas; thus, fast charge transport could

be achieved. With this configuration, Pb^{2+} can penetrate into the PPy layer under a positive gate voltage, decreasing channel conductivity. The channel current exhibited a dependence with the Pb^{2+} concentration in the range of 10^{-5}–10^{-2} M (Figure 14b), and a limit of detection (LOD) of 10 μM toward Pb^{2+} could be achieved. These FSOECTs can directly integrate into a nonwoven fabric (Figure 14c) and could find application in textile-based sensors.

To overcome mechanical flexibility issues resulting from the underlying cotton fiber substrate, Yoon and co-workers[198] developed substrate-free PEDOT:PSS-microfiber-based FSOECTs for wearable ion sensing. These devices were developed by using a PEDOT:PSS channel fiber fabricated by wet spinning. In this process, a concentrated PEDOT:PSS aqueous solution (2.0–2.5 wt%) injected into a sulfuric acid solution through a syringe needle, results into the formation of a continuous fiber due to the rapid coagulation of PEDOT:PSS. The overall cross-sectional area, and thus conductivity, of the PEDOT:PSS fiber could be controlled by changing the diameter of the needle and/or the acid concentration in the coagulation bath. Ag wires fixed to the PEDOT:PSS fiber by Ag epoxy served as source/drain electrodes and next the device was passivated by poly(methyl methacrylate) (PMMA) except for the Ag epoxy point of the source electrode. The exposed Ag epoxy area was chlorinated to obtain a Ag/AgCl system functioning as a source–gate hybrid electrode (**Figure 15**a). Consequently, the single-strand fiber-type FSOECT worked as a two-terminal device, where the gate voltage was fixed at 0.0 V. The channel current variation ratio ($|\Delta I_{DS}/I_{DS0}|$) of this FSOECT at different ion concentrations was used for evaluating the detection sensitivity (Figure 15b). For practical application in human physiological monitoring (Figure 15c), the two-terminal single-strand fiber-type FSOECT was applied to detect the total cation concentration (e.g., Na^+, K^+, etc.) in PBS samples, artificial sweat samples, and real human sweat samples, with the results matching well with those obtained from ion chromatography–inductively coupled plasma mass spectrometry (IC-ICP–MS).

Since sweat-based biosensors provide a noninvasive route to continuously monitor physiological conditions, an efficient approach for sweat collection and storage is needed for constructing FSOECT-based wearable ion sensors. Parlak and co-workers[178] fabricated a wearable patch-type FSOECT-based ion sensor for the detection of physiological levels of NH_4^+ and Ca^{2+} in sweat. In this case, a highly stretchable SEBS elastomer was used as the substrate of the PEDOT:PSS-based OECT, ISMs for NH_4^+ and Ca^{2+} were directly deposited on the channel of the two OECTs to realize multiplexed ions sensing (**Figure 16**a). An important aspect addressed by this study was the sweat collection method, where a laser-patterned microcapillary sweat-acquisition layer was introduced and placed in between the ISMs and human skin. In this way, sweat samples could be effectively collected, while the ISM surface was protected from mechanical damage. The proposed ISM-based FSOECTs exhibited a wide ion detection range from 0.01×10^{-3} to 100×10^{-3} M, which matched well with the ion concentrations of NH_4^+ and Ca^{2+} in human sweat.

Given that the active polymer channels of OECTs can be prepared by solution-processing methods, this presents a unique opportunity to construct FSOECT-based ion sensors via low-cost printing techniques. For instance, Gupta and co-workers[223] used 3D printing to fabricate a flexible inverter logic circuit based on PEDOT:PSS OECTs for the detection of several cations (here, Na^+, Ca^{2+}, and K^+) at different concentrations. A silver conductive paste and PEDOT:PSS ink were used to print the electrode and the channel layer on PET substrate, respectively, and finally a PDMS mask layer was printed to prevent electrical short during measurements (Figure 16b). In this work, the switching input voltage in the voltage output characteristics shifts to lower values as the cation concentration increases (Figure 16c). By analyzing the results of different ions, the authors found that the switching input voltage directly correlated with the cation mobility, thus, the cation type. This novel method provided a simple way to achieve ion sensing, but limitations remain for real-time wearable applications, since it requires ion samples of different concentrations to determine the cation type.

Due to the growing demand for detecting multiple ions simultaneously and spatial mapping of ion concentrations which can provide dynamic information, OECT-based sensor arrays with various ion detection units have been developed. Doris and co-workers[165] integrated a miniaturized ISM-decorated FSOECT array with a simple multiplexer composed of indium gallium zinc oxide (IGZO) thin-film transistors (TFTs) on a flexible PI substrate as a multi-ion sensing system (Figure 16d). Benefitting from the high electron mobility, excellent on–off current ratio, low subthreshold slope, and flexibility of IGZO TFTs, logic gate functionality and minimized crosstalk during multiplexing were achieved. In this configuration, each sensing unit was composed of an ISM-decorated OECT with PEDOT:PSS as the channel layer (Figure 16e) connected in series with a resistor to form a voltage amplifier while converting the concentration-dependent effective gate voltage into an output voltage. Then, the IGZO TFT with Au electrodes (Figure 16f) functioning as a multiplexer was connected to each sensor, which allowes the output voltage of the corresponding sensor in the array to be measured separately. Due to the excellent amplification properties of the integrated circuit, the detection sensitivity for Na^+ and K^+ over the concentration range of 1 μM to 100 mM was ≈230 mV dec^{-1} (a decade represents a tenfold change of ion concentration), while that for Ca^{2+} was about 175 mV dec^{-1}. This creative design is a stepping stone for further commercialization of FSOECT-based sensing arrays.

Continuous progress made in OECT-based ion and pH sensors have given rise to new application fields. For instance, the dynamics of ion transport in cells can be monitored in real time by interfacing them on the channel surface of an OECT to access physiological activities and effect of drugs.[240] Moreover, methods to improve OECT selectivity to ion sensing are also constantly being updated by introducing new device structures and innovative functional layers, such as modifying the functional polymer on the gate electrode for the selective capture of targeted cations.[241]

5.1.2. Glucose

Glucose level monitoring is of great value in biomedical applications with enzymatic biosensors being very sensitive and selective. Typical working mechanisms of OECT-based enzymatic sensors for glucose can be divided into three types: i) variation

of the channel electrical conductivity due to the change of the electrolyte pH after the enzyme-catalyzed reaction of glucose (**Figure 17**a),[242–245] ii) variation of the semiconductor oxidization state in the channel after the enzymatic reaction inside the channel layer (Figure 17b),[246–250] iii) Faradaic current generation at the gate electrode surface due to the enzymatic reaction (Figure 17c).[28,226]

PANI was initially used as the channel material of rigid OECT-based sensors for glucose detection since its conductivity depends on the pH value of the electrolyte. Thus, in a study from Contractor and co-workers,[244] PANI was deposited on two platinum disk electrodes functioning as the source/drain electrodes, next another layer consisting of glucose oxidase (GOx) entrapped into PANI was deposited on the channel. The resulting OECT device sensed the change in the pH microenvironment resulting from the GOx-catalyzed oxidation of glucose, generating a linear response for glucose concentration up to 10 mM and a detection limit of about 2 mM. Bartlett and Birkin[246] proposed an OECT-based glucose sensor by coating a GOx-immobilized poly(1,2-diaminobenzene) film on the top of a PANI channel film. The application of a GOx-immobilized poly(1,2-diaminobenzene) film, apart from producing a highly reactive enzyme film, prevents interference from other species present in the electrolyte analyte solution. In addition, this device was also placed in a tetrathiafulvalene (TTF)-containing solution to allow the incorporation of TTF functioning as a redox mediator to couple the enzyme-mediated reaction with the transducing PANI layer. The sensing mechanism was attributed to the change of the oxidization state of PANI (from insulating state to conductive state) after the enzymatic reaction with glucose. However, the reduced electrochemical activities of PANI in neutral pH values of typical physiological environments has hindered its use.[251,252]

Since PEDOT:PSS exhibits greater stability in a wide pH range, it has been recently explored more for glucose OECT sensors. Malliaras and co-workers have been systematically investigating PEDOT:PSS-based OECTs for enzyme-based glucose sensors.[28–30,60,61,130,191,253–256] This group first proposed a simple OECT device consisting of a patterned PEDOT:PSS stripe on a glass support and a Pt wire gate electrode.[130] The PBS electrolyte (pH 7.4) and GOx were confined by an elastomeric PDMS cell placed in contact with the PEDOT:PSS layer. When glucose was added into the electrolyte, the channel current of the OECT under a positive gate voltage pulse decreased dramatically (**Figure 18**a). The authors demonstrated that the response of this sensor was not due to the pH change caused by the generation of gluconolactone in the enzymatic reaction, but due to the generation of hydrogen peroxide (H_2O_2), which was oxidized at the Pt gate electrode and resulted in reduction of the PEDOT:PSS layer. Importantly, this OECT sensor is sensitive to glucose from a concentration of ≈1 to as low as 0.1 mM.

Based on the above study, Bernards et al.[28] explored in more detail the device operation and physics of PEDOT:PSS-based OECTs for glucose detection. In this work, the OECT consisted of a PEDOT:PSS channel film and a PBS electrolyte containing GOx with a Pt gate electrode (Figure 18b). The transfer curve of this device shifted to a lower value after the glucose was added to the electrolyte. The relative shift of the gate voltage (defined V_{offset}, $V_{GS}^{eff} = V_{GS} + V_{offset}$) was found to be dependent on the glucose concentration from 0.01 to 1 mM (Figure 18c), and could be described by the Nernst equation where the chemical potential depends on the concentration of the redox-active species. The device sensing mechanism to glucose was corroborated by finding that H_2O_2, the byproduct of the enzymatic reaction of glucose in the presence of oxygen, reacted at the gate and induced a Faradaic current, which further decreases the potential drop at the electrolyte/Pt–gate interface. The increased potential drops on the electrolyte/channel interface led to dedoping of PEDOT:PSS and decreased I_{DS}. The results of this work helped elucidate the physics of OECT-based enzymatic sensors.

The development of FSOECTs for glucose sensing (Table 3) began with the work of DeCoster and co-workers,[189] in which a glucose sensor was made with PEDOT:PSS functioning as all the electrodes and the channel material. The device was fabricated by a one-step fabrication process using xurography (Figure 18d) where a polymer well was used to define the working area of both the gate electrode and the channel. The addition of glucose to the GOx containing well reduced the enzyme and generated H_2O_2. The oxidation of H_2O_2 was catalyzed at the PEDOT:PSS gate electrodewhich reduction of the PEDOT:PSS in the channel was proportional to the glucose concentration. This device detected glucose concentration from ≈1 μM to 10 mM, which meets the detection requirements of the glucose levels in human saliva (8–210 μM).

Later, Yan and co-workers[65,175,210] conducted a series of studies investigating FSOECT-based glucose sensors for human health monitoring. Thus, a device consisting of a Pt gate, source, and drain electrodes, PEDOT:PSS as the channel material, a PBS electrolyte was assembled on a flexible PET substrate.[65] To improve the selectivity of the devices to H_2O_2 versus other charged molecules (e.g., ascorbic acid (AA), dopamine (DA)), the Pt gate electrode of the OECT was modified with a thin layer of a composite of graphene flakes and Nafion, followed by a thin PANI layer. The modified PANI film is in the H^+ protonated emeraldine salt form, which can strongly repel positively charged molecules such as DA in PBS solution by electrostatic forces. On the other hand, Nafion, an acid with a stable Teflon backbone and acidic sulfonic groups, is negatively charged when in contact with the PBS solution and could effectively impede the diffusion of anionic species such as AA and uric acid (UA). Therefore, the PANI/Nafion–graphene bilayer film can block the diffusion of both positively and negatively charged molecules to the Pt gate and improve the selectivity of the device to H_2O_2. In addition, the use of graphene flakes improved the electrocatalytic activity and the conductivity of the gate electrode. The immobilization of GOx on the PANI/Nafion–graphene/Pt gate electrode was achieved by using graphene oxide (GO). In this configuration, a LOD for glucose as low as 30×10^{-9} M was obtained (**Figure 19**a). This FSOECT platform could be conformably contacted to various deformable surfaces such as human skin and fabric and retain stable electrical performance after thousands of bending cycles (Figure 19b) at an undisclosed strain.

Constructing FSOECT-based sensors using common flexible/stretchable substrates still suffers several issues for real applications of human health monitoring, including variation of performance upon mechanical deformation, poor adhesion to the human skin, and low air permeability causing skin inflammation. Fabric-OECT-based sensors could be an efficient way to

address some of these issues.[133] However, the high electrical resistance of metal-free fiber electrodes greatly hindered the sensing performance of these devices.[171,222] Consequently, Yan and co-workers[210] fabricated a fabric glucose sensor by constructing nylon-fiber-based FSOECT. The fabrication process is shown in Figure 19c, where first a nylon fiber was coated with Cr/Au by magnetron sputtering using a narrow tape mask to define the source/drain electrodes, next, PEDOT:PSS channel was coated on the fiber by dip coating. Finally, a different nylon fiber coated with Ti/Pt was used as the gate electrode and it was cross-connected with the source/drain fiber. Note, both fibers were encapsulated with parylene film to define the exposed channel region and the gate electrode, which can be filled with a PBS electrolyte. To achieve glucose detection, the gate electrode was modified with a composite consisting of GOx, chitosan (provides a biocompatible environment for enzyme), and graphene flakes (improves electron conductivity) on the surface. After different glucose amounts were added to the PBS electrolyte, thus resulting in different concentrations, the channel current of the sensor decreases with increasing the glucose concentration. This device design afforded a low LOD of 30×10^{-9} M and allowed integrating the sensor into a fabric by coating it with a PVA protection layer during the weaving process and then removing it by water washing (Figure 19d). This glucose sensor fabric can function by infiltrating body fluids as the electrolyte and the authors found that it showed similar glucose detection performance as the fiber-based device before weaving. Note, although the fabric-based device developed a new perspective in the structural design of FSOECT-based sensors, the stretchability of such devices remains limited by the unstretchable connection between the two fibers. To further promote the stretchability of wearable FSOECT-based glucose sensors, a stretchable PDMS film was patterned with a 2D wavy structure and used as the substrate for PEDOT:PSS-based FSOECTs.[175] The substrate pattern was transferred from the bract of *Bougainvillea glabra* by pouring PDMS over the bract mold, then a highly rough surface composed of buckled structures in sizes of 40–80 μm was replicated on the PDMS film after removing the bract residues. Since the original pattern of bract was isotropic in nature, the resulting PDMS film automatically inherited the 2D wavy structures, which was important for constructing the stretchable device. Next, Cr/Au gate, source, and drain electrodes were deposited on the top of the patterned PDMS substrate. PEDOT:PSS was used as the channel as well as it was printed on the Cr/Au electrodes to fill cracks generated in the electrodes upon stretching, thus it stabilized the electrode conductivity. This design led to an omnidirectional stretchability of the device up to 30%. To complete the wearable glucose sensor, a composite layer consisting of chitosan/Pt flakes and GOx was deposited on the gate electrode, and PBS was used as the electrolyte. This device exhibited a fast channel current response when glucose was added to the PBS electrolyte, with a LOD of ≈1 μM.

Considering body-compliance and skin irritation requirements in wearable sensors, the concept of a skin-worn temporary tattoo is an interesting strategy for constructing noninvasive FSOECT-based glucose monitoring platforms. Khademhosseini and co-workers[133] proposed a transfer-printing method for efficient patterning of a PEDOT:PSS layer on soft substrates and human skin by using a hydrogel carrier (such as agarose, gelatin, and PVA). The first key step in device fabrication is mixing dodecylbenzene sulfonic acid (DBSA) with PEDOT:PSS before pattering it on a glass substrate. The resulting mixture adheres less to the carrier glass substrate, and thus can be transferred on various soft substrates coated with a hydrogel due to the stronger adhesion between PEDOT:PSS and the hydrogel. Thus, the skin-attachable FSOECT tattoo can be completed by depositing source/drain electrodes (Au) on a commercially available tattoo paper with a laser-ablated shadow mask, then laminating the hydrogel stamp with the patterned PEDOT:PSS coating onto the channel area between the source/drain electrodes (Figure 19e). The resulting FSOECT-based tattoo sensor could be laminated directly onto the skin by dissolving the supporting substrate of the tattoo paper with water. This device exhibited excellent compliance with the human skin and stable electrical characteristics upon different mechanical deformations of the skin such as 5% tensile stress and 40% compression stress (Figure 19f). By integrating FSOECT-based tattoo with wireless communication and data readout modules, a compact wearable sensor prototype on human skin was also demonstrated. In addition, a separated Pt electrode coated with GOx was used as the gate electrode, and the integrated device was able to response to a glucose concentration down to 1×10^{-6} M in the PBS electrolyte. While this tattoo design is quite effective to enable flexibility and stretchability, further improvements could be achieved by adoption of a planar gate electrode configuration for a more integrated system and the development of miniaturized flexible functional accessories, such as a power supply module and a Bluetooth communication unit.

In addition to the application in disease diagnosis and health monitoring of mammals, researchers also expanded FSOECT-based glucose sensors to other applications. For instance, Stavrinidou and co-workers[132] utilized PEDOT:PSS-based FSOECTs for real-time monitoring of the glucose level in plant organelles–chloroplasts (**Figure 20**a). Plants are able to convert energy from sunlight into sugars via a photosynthetic process. Chloroplasts are the organelles where the photosynthetic reactions take place, storing the excess of photosynthetic products in the form of starch granules during the day, and converting starch granules into simpler sugars such as glucose during the night to supply the plant's energetic demands. The rate of starch degradation and subsequent amount and rate of sugars exported from chloroplasts will determine the plant's metabolism, growth, and development during night. Thus, sugars are important plant signaling molecules related to metabolism, growth, stress responses, and development. In this work, a FSOECT was fabricated on a thin flexible PEN film, and the PEDOT:PSS-coated gate electrode was next functionalized with Pt nanoparticles and GOx cross-linked on a chitosan membrane for sensitive and selective glucose sensing (Figure 20b). During the detection of glucose export from active chloroplasts, the OECT was operated in a chloroplast isolation buffer (CIB) solution, where the chloroplast was extracted from tobacco plants. The exported glucose detected by the OECT versus the concentration of intact chloroplasts, for chloroplasts harvested in the nighttime mode, daytime mode, and for the control devices are shown in Figure 20c. Interestingly, a fast export of glucose from the nighttime chloroplasts with an increasing trend that lasted for up to 30 min was observed, and an average export of 170 nM glucose mg^{-1} chloroplast was recorded during 1 h monitoring. The direct coupling of the chloroplasts

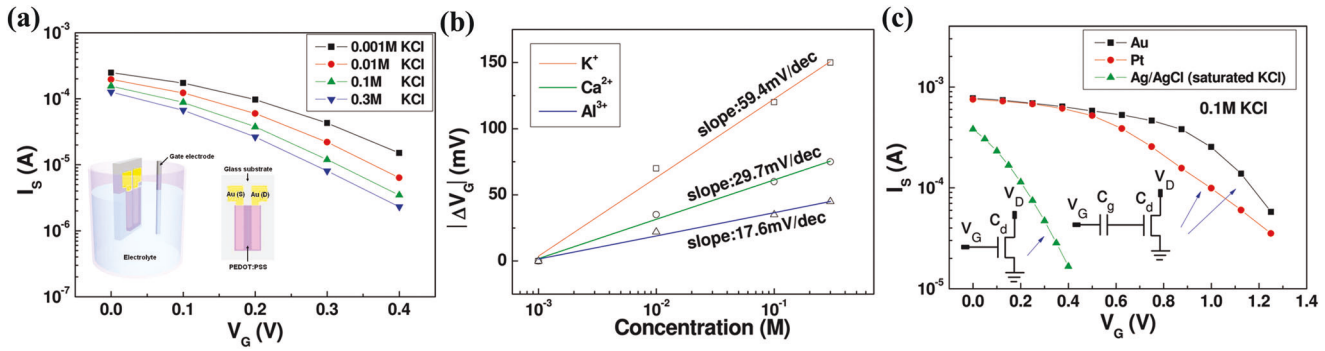

Figure 13. a) Transfer characteristics of an OECT in aqueous electrolytes with different KCl concentrations (inset is the OECT schematic). b) Dependence of the gate voltage shift on the concentration of cations of different salt solutions such as KCl, $Ca(NO_3)_2$, and $Al_2(SO_4)_3$. c) Transfer characteristics measured using KCl aqueous electrolyte with different gate electrodes (Ag/AgCl wire, Pt wire, Au wire). a–c) Reproduced with permission.[238] Copyright 2010, American Chemical Society.

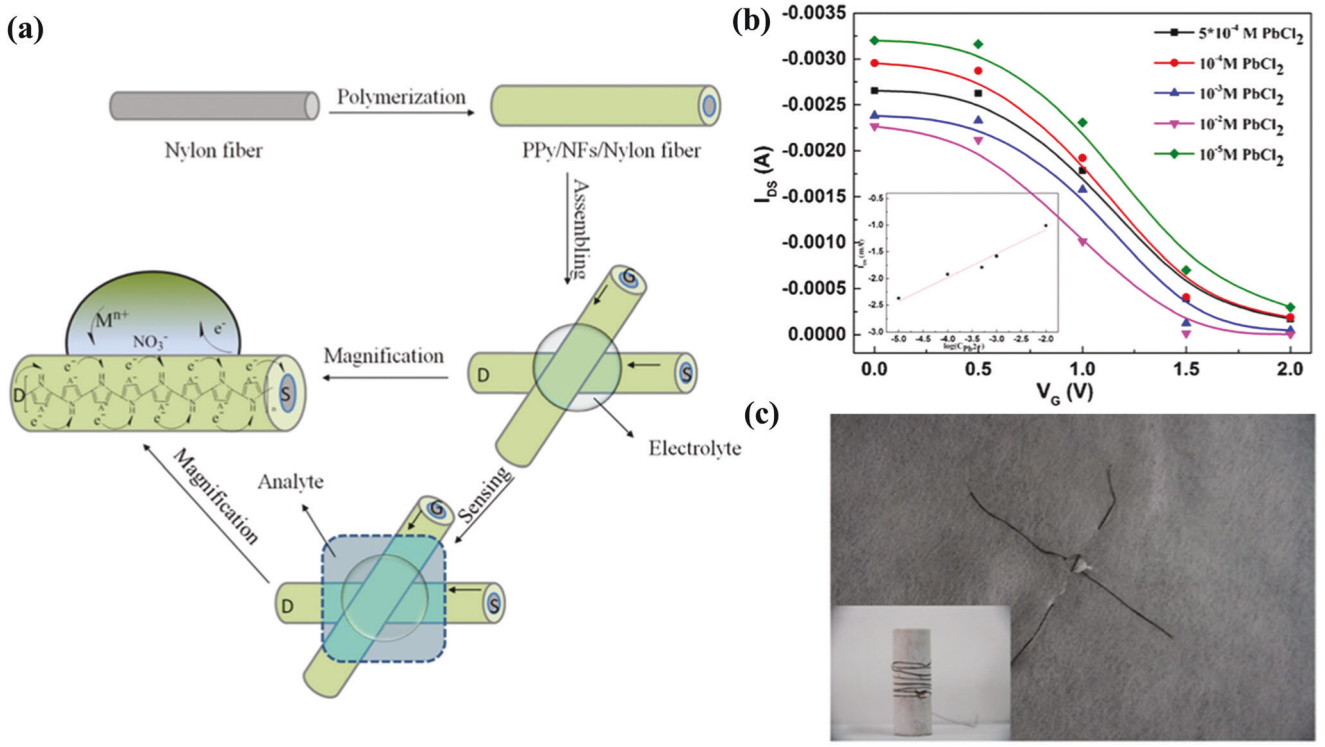

Figure 14. a) Schematic representation of a flexible PPy-coated nylon-fiber-based FSOECT. b) Transfer characteristics of the FSOECT with Pb^{2+} ion concentrations over the range from 10^{-5} to 10^{-2} M. Inset is the channel current vs $\log(Pb^{2+})$ of the device. c) Optical image of a nylon-fiber-based FSOECT directly integrated into a nonwoven fabric. a–c) Reproduced with permission.[239] Copyright 2016, Springer Nature.

with the OECT allowed monitoring the initial glucose export kinetics with a temporal resolution of 1 min during the first 10 min (Figure 20c). This research paved the way for further kinetic investigations into various biological processes using FSOECTs as platform.

Most of the OECT-based glucose sensors reported to date have been fabricated with p-type PEDOT:PSS as the channel material. Utilization of n-type OECTs is limited by the poor stability and low g_m of electron-transporting semiconductors.[69,102] Note, n-type OECTs should be more suitable for glucose sensing since the n-type channel can directly accept electrons formed in the enzyme-catalyzed reaction and act as a series of redox centers to transmit physiological signals.[257,258] Thus, recent developments in high-performance n-type OECTs are a great opportunity for superior detection of glucose.[103,258,259] Inal and coworkers[258] demonstrated the use of the n-type semiconductor P-90 (**Figure 21**a), which exhibits good water uptake capacities and a g_m of ≈2.2 µS with a PBS electrolyte, for the fabrication of n-type OECT-based glucose sensors. Both channel area and planar gate were covered with P-90, and the device operates in the accumulation mode. To achieve selective detection of glucose, a GOx solution was drop casted on the active area (the P-90 chan-

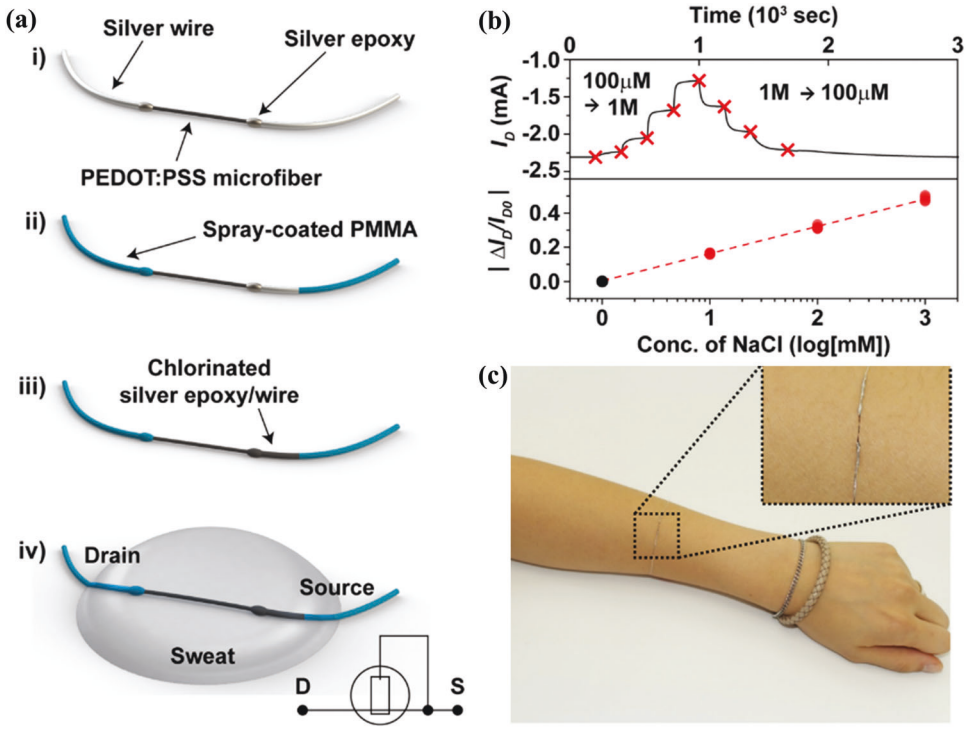

Figure 15. a) Schematic representation of a substrate-free PEDOT:PSS-microfiber-based FSOECTs for sensing cation concentration. b) Drain current (upper) and variation ratio ($|\Delta I_{DS}/I_{DS0}|$) (lower) of the PEDOT:PSS-microfiber-based FSOECTs for different NaCl concentrations. c) Optical image of the PEDOT:PSS-microfiber-based FSOECT directly mounted onto human skin. a–c) Reproduced with permission.[198] Copyright 2018, Springer Nature.

nel and gate region) (Figure 21b). After the addition of glucose to the PBS electrolyte, the channel current increases due to the reaction of glucose with GOx followed by electron transfer to the P-90 film (Figure 21c). Note, in this detection process, the exogenous electron mediator was no longer needed for the enzyme to operate, thus, the device design was extremely simplified.[257] By analyzing the relation between channel current and the glucose concentration (here ranging from 10 nM to 20 mM), an ultralow LOD of 10 nM was obtained (Figure 21d). Optimization of n-type OECT-based glucose sensors for use in complex physiological environments will need to identify new n-type semiconductors with even greater stability and performance in aqueous electrolyte media, matching those of the best p-type.[69,108] Since the n-type P-90/GOx film enhances I_{DS} during the enzyme-catalytic reaction, it was further employed as the anode of an enzymatic biofuel cell (EFC) and integrated with a cathode comprising the p-type p(EDOT-*co*-EDOTOH) (EDOT, 3,4-ethylenedioxythiophene; EDOTOH, hydroxymethyl 3,4-ethylenedioxythiophene) polymer to convert chemical energy (glucose and oxygen) to electrical power.[258] The authors demonstrated that the power provided by the EFC could drive an OECT by manipulating the glucose concentration in the cell. This work demonstrated an interesting approach for a new generation of self-powered glucose sensors.

In the same vein, Salleo and co-workers[260] also integrated an electrochemical biofuel cell with an OECT (gated by Ag/AgCl), for self-powered glucose sensing (Figure 21e). In detail, the biofuel cell consisted of a tetrathiafulvene tetracyanoquinodimethane (TTF-TCNQ)-based cathode and a p(gT2)-based anode, and power generation relies on the enzyme-catalytic reaction of glucose with the GOx in the PBS electrolyte (Figure 21f). This cell was connected with an OECT and provided the gate bias, the significant increase of voltage bias (>300 mV) of the biofuel cell allowed the connected OECT to achieve high current modulation ratios (>10^4). Greater signal amplification can be obtained with these device configurations where the chemical transduction of glucose is separated by the OECT amplification processes. In addition, the self-powered detection and signal amplification of physiological signals by harvesting energy from the biological environment, is of great significance for constructing wearable real-time sensing system for health monitoring.

5.1.3. Other Metabolites

In addition to glucose, several other metabolites have important roles in modulating the physiological activities of biological systems. Metabolite detection with OECTs can be mainly classified into two types. 1) Detection of metabolite molecules that are uncharged such as lactate, cortisol, and cholesterol. Here, the sensing mechanism is similar to that of glucose by using specific enzymes for these molecules.[228,261–263] 2) Detection of charged or easily oxidizable metabolites such as UA, DA, AA, and epinephrine. Here, detection can be achieved by electron transfer induced by metabolite oxidization at the gate electrode surface without the need of an enzyme and redox mediators. Detection sensitivity for both processes could be improved by gate surface modification with nanomaterials to facilitate elec-

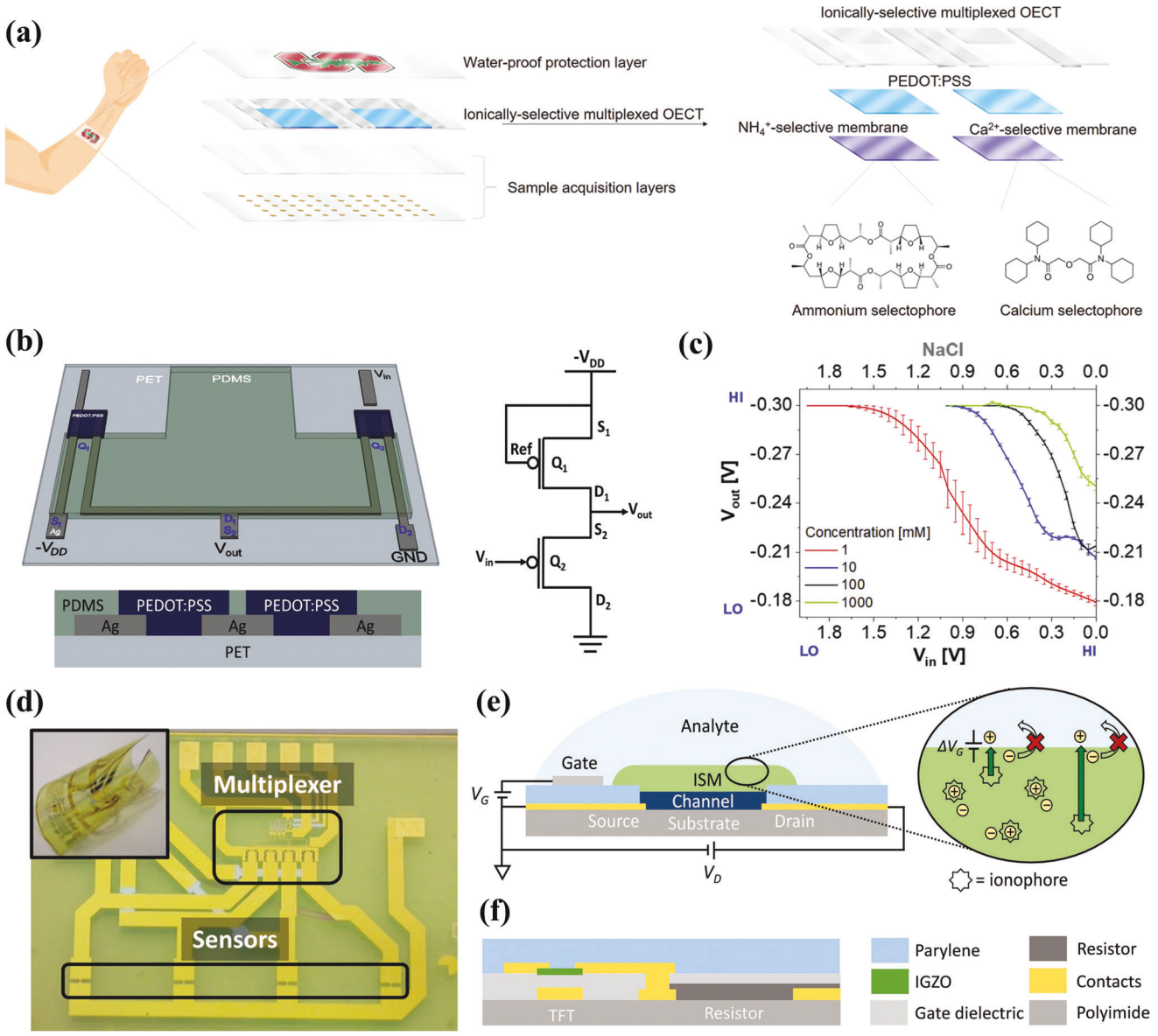

Figure 16. a) Schematic illustration of a wearable ion-selective FSOECT patch for multiplexed sensing of NH_4^+ and Ca^{2+} ions. The device comprises a polyethylene (PE)-based protection layer, a multiplexed sensor layer on the SEBS substrate, and a PI-based sweat acquisition layer. Reproduced with permission.[178] Copyright 2019, Wiley-VCH. b) Schematic illustration and circuit diagram of the FSOECT-based inverter on a PET substrate and passivated with a PDMS mask. c) Voltage characteristics of the FSOECT-based inverter in aqueous electrolytes with different NaCl concentrations. b,c) Reproduced with permission.[223] Copyright 2019, Elsevier. d) A multiplexer and FSOECT ions sensing array integrated on a PI substrate in a flat and a flexed state (inset). e,f) Schematic illustrations of the geometry and operation mechanism of the OECT sensing module (e) and the IGZO TFT module (f). d–f) Reproduced with permission.[165] Copyright 2018, Wiley-VCH.

tron transfer.[264–267] Note, even though the detection of charged metabolites does not require an enzyme and redox mediators, improvements are necessary since these devices suffer for poor selectivity.

Malliaras and co-workers developed several fully solid-state wearable sensors, suitable for analysis of metabolites in limited sample solution volumes, employing gel electrolytes.[164,173,197] In one example, a flexible OECT for in situ lactate detection was fabricated on a parylene substrate using PEDOT:PSS as the channel and gate electrode and an enzyme-based solid state electrolyte was coated on the channel surface (**Figure 22**a).[197] The solid-state electrolyte consisted of lactate oxidase (LOx), ferrocene as mediator, an ionic liquid ($[C_2mIm][EtSO_4]$), as well as a photo-cross-linkable mixture to define the gel network (Figure 22b). For lactate sensing, a small volume (20 µL) of PBS solution with the desired lactate concentration was dropped on the solid electrolyte. This device sensed lactate within a concentration range of 10–100 mM. Since the solid electrolyte slows the diffusion of the analyte, the time required for the sensor to reach a steady state after sampling was ≈10 min.

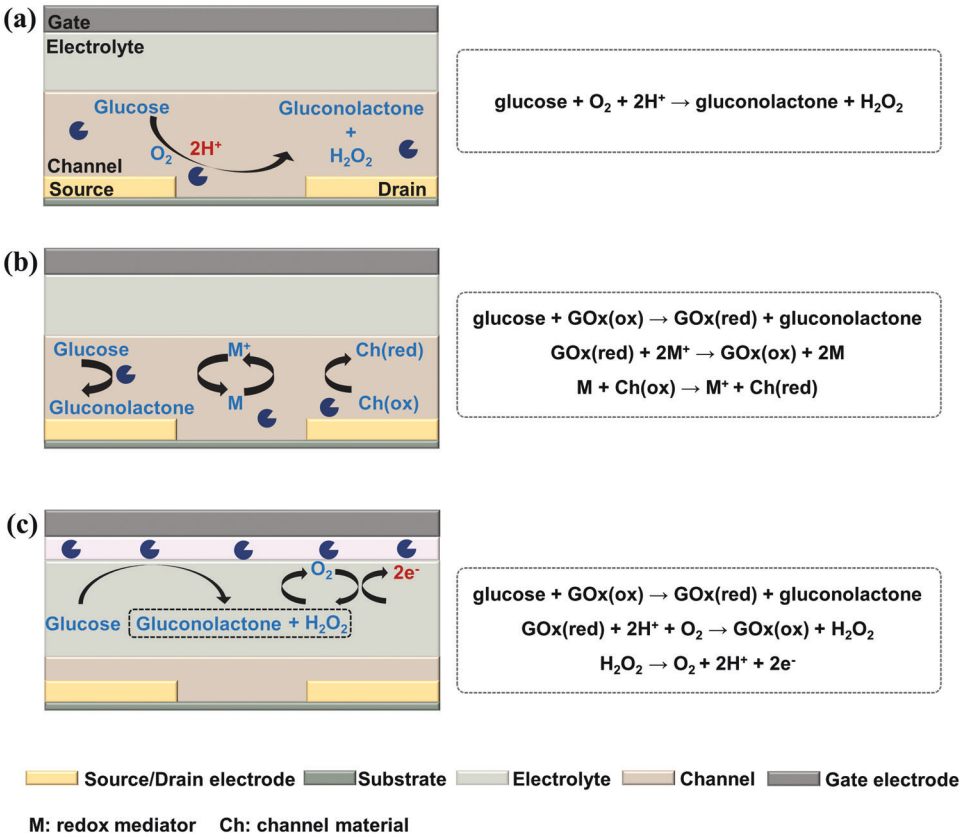

Figure 17. a–c) Schematic illustration and the corresponding reactions occurring of different OECT-based sensors for glucose detection.

The same group also reported a disposable breathalyzer based on a gel-electrolyte-gated FSOECT for alcohol sensing.[173] The gel electrolyte used in this work was prepared by adding a blend of the enzyme alcohol dehydrogenase (ADH) and its cofactor nicotinamide adenine dinucleotide (NAD^+) to a bovine gelatin, which is a good candidate for preparing electrolyte gels due to the high biocompatibility. This device was fabricated on a flexible paper substrate, where the channel and gate electrodes were made of inkjet-printed PEDOT:PSS. After exposing the FSOECT–breath analyzer to ethanol from the breath, a marked decrease of the channel current was observed. Detail of the detection mechanism is shown in Figure 22c, where the enzyme-catalyzed reaction of alcohol produces electrons, which in turn decrease the conductivity of the OECT channel. The ethanol concentration range tested by the authors (from 0.01% to 0.2%) is equivalent to the blood alcohol content in the human body after a glass of wine consumption, thus this device could be used to monitor drinking behavior.

Although solid-state electrolytes are advantageous for developing fully solid-state wearable metabolite sensors, inherent limitations remain such as vulnerability to interference from other ions present in the sample solution. As a result, the development of artificial metabolite sensors with greater stability and selectivity are expected to replace biological enzymes. Salleo and co-workers[179] introduced molecularly selective nanoporous membranes (MSMs) consisting of molecularly imprinted polymers as an artificial recognizer of cortisol in FSOECTs for human sweat wearable monitoring (Figure 22d). This device consists of a PEDOT:PSS OECT with a planar Ag/AgCl gate as an electrochemical transducing layer functionalized with an MSM, coupled with a laser-patterned microcapillary channel array for sample acquisition, and a hydrophobic protection layer. The device is fabricated on a SEBS elastomer substrate to allow flexibility and stretchability of the wearable sensor. The MSM pores allowing ion transfer can be blocked by cortisol in the electrolyte and thus affecting the channel current. Cortisol levels in human sweat (collected from healthy human subjects) was monitored by this wearable FSOECT sensor, where a concentration range of 0.01–10.0 μM and a sensitivity of 2.68 μA dec^{-1} along with high selectivity were obtained. Due to the high stability and mechanical flexibility of the MSM, the surface topography and temperature variations of the human skin do not affect the performance of this device, which further demonstrates the capability for real-time on-body monitoring as a wearable sensor assembly.

In the case of monitoring charged and electroactive metabolites in biological systems, such as UA, DA, AA, and various neurotransmitters, FSOECT-based sensors have also been widely investigated.[131,174] However, one of the drawbacks for most of those OECT-based sensors is the lack of selectivity since any electroactive metabolite can react at the gate electrode surface. This problem stands as a barrier to application of OECT-based sensors in complex physiological environments. Liu and co-workers[190,211] recently reported a PEDOT:PSS-based

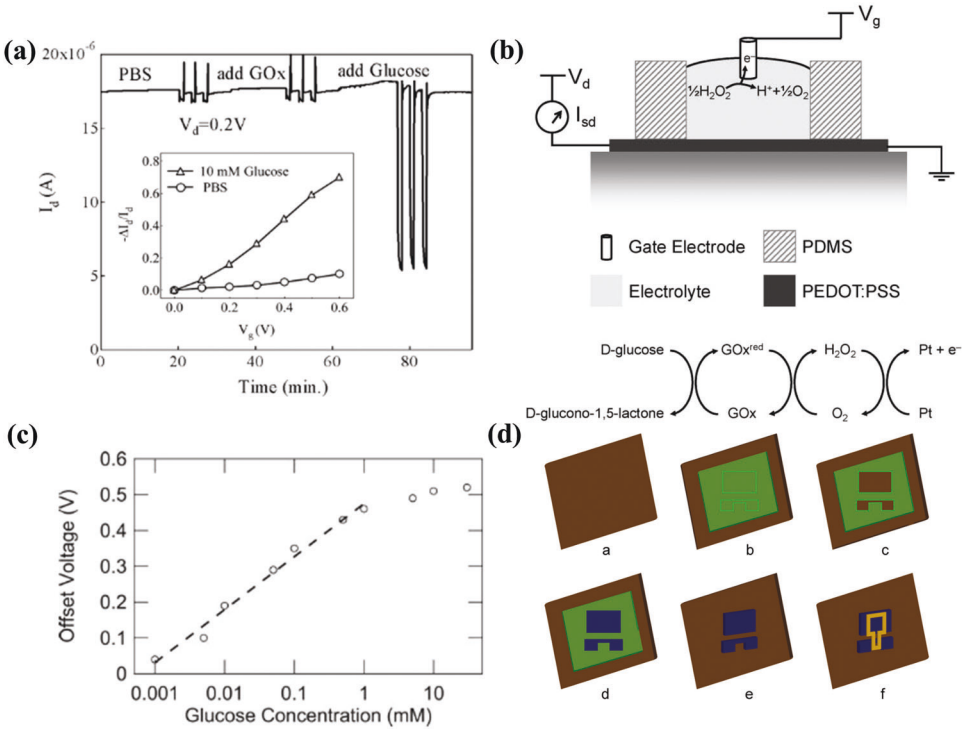

Figure 18. a) Channel current vs time for the PEDOT:PSS-based OECT in a PBS solution, in which the GOx and glucose are added. Inset is the variation ratios of channel current as a function of gate voltage in different electrolytes. Reproduced with permission.[130] Copyright 2004, Royal Society of Chemistry. b) Schematic illustration of the reaction at the Pt gate electrode surface and the reaction cycle involved in the GOx-based glucose detection of OECT. c) Dependence of the offset voltage on the glucose concentration. b,c) Reproduced with permission.[28] Copyright 2008, Royal Society of Chemistry. d) Schematic illustration of the FSOECT fabrication process. a: pretreated substrate, b: fasten patterned polyimide tape, c: strip patterned region, d: spin-coated PEDOT:PSS, e: peel unwanted tape, f: fasten polymer well. Reproduced with permission.[189] Copyright 2011, Elsevier.

FSOECT with high selectivity to DA and AA (Figure 22e). In this work, a Ti/Au layer was deposited on a flexible PEN substrate as the source/drain electrodes followed by PEDOT:PSS spin-coating deposition on the channel. For the fabrication of the gate electrode, a nitrogen/oxygen-codoped carbon cloth (NOCC) was fabricated by carbonizing PANI-wrapped carbon cloths at high temperature and then directly pasted on the PEN substrate (Figure 22f). The doping of N and O atoms in the carbon cloth electrode surface was regulated by changing the carbonization atmosphere (oxidative, inert, or reductive). By optimizing the reaction atmosphere, highly sensitive and selective carbon cloth gate electrodes were obtained for DA and AA detection. Significant concentration ranges of 5×10^{-6} to 1×10^{-3} M for AA detection and 1×10^{-6} to 3×10^{-4} M for DA detection were achieved in addition to high selectivity. Surface composition analysis and theoretical simulations indicated that detection selectivity was highly dependent on the heteroatoms present on the gate electrode surface. Furthermore, the device flexibility was also tested according to the transfer characteristics after bending test (Figure 22g), while stable sensing performance could be obtained after bending the device to both sides with a bending angle of 90° for 500 times, and the device flexibility could be further improved by developing a fully carbon cloth FSOECT, since only the gate electrode was made of carbon cloth in this work.

To further increase the selectivity for DA detection, a metal-free gate electrode consisted of Nafion and reduced-graphene-oxide-wrapped carbonized silk fabric was utilized as the gate electrode of a PEDOT:PSS-based FSOECT.[190] In this configuration, the selective detection of DA was achieved by electrostatic repulsion between the negatively charged Nafion and the interfering molecules (negatively charged UA and AA with carboxyl groups), thus, the interfering molecules are unable to react at the gate electrode surface except for DA. The design concept of replacing traditional metal electrodes with carbon materials (carbon cloth and carbon silk) in the fabrication of freestanding electrodes not only improves the selectivity of OECT-based sensors in electroactive metabolites detection, but also facilitates the further development of wearable textile sensors.

To improve selectivity in biosensing applications, aptamer-based technology has proven to be an excellent choice.[268–270] Mayer and co-workers[229] recently reported a DA sensor by combining aptamers as the specific recognition element in a FSOECT. In this configuration, Au as source, drain, and gate electrodes was fabricated on a flexible PI substrate, next PEDOT:PSS was deposited as the channel material. Here, a split aptamer strategy, by splitting the full aptamer of DA into two fragments (aptamer 1 and aptamer 2), was employed to modify the gate electrode. The receptor fragment (aptamer 1) was covalently attached to the gate electrode surface via a thiol–gold bond, and the other fragment (aptamer 2) was used for signaling, labeled with a redox group (methylene blue) at the distal end. Once the mixture of analyte DA and aptamer 2 is added, a sand-

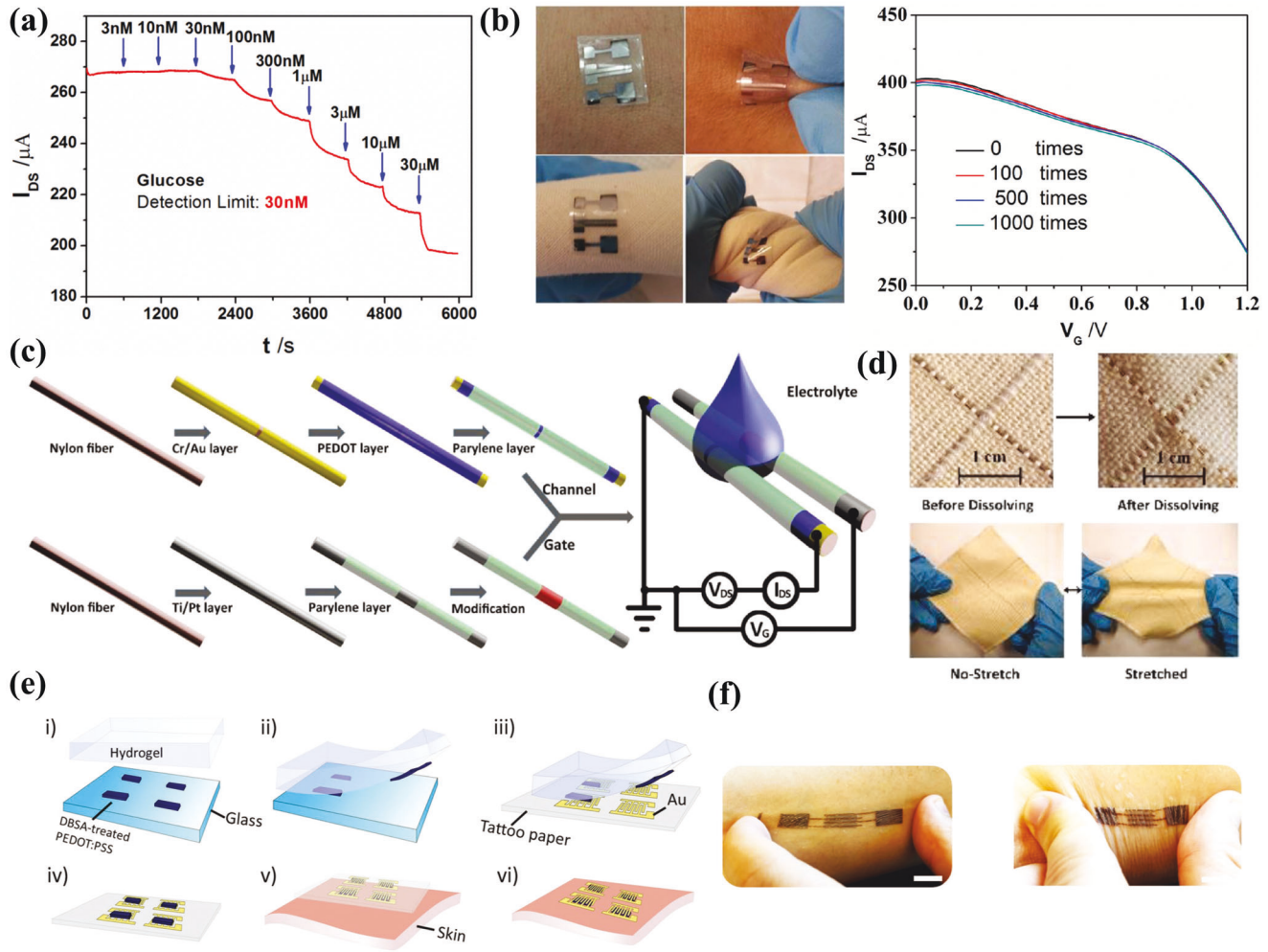

Figure 19. a) I_{DS} responses of a FSOECT with Gox–GO/PANI/Nafion–graphene/Pt gate electrodes to different glucose concentrations. b) Photographs of a FSOECTs attached to various deformable surfaces, along with the corresponding transfer characteristics after various bending cycles (PBS electrolyte). a,b) Reproduced with permission.[65] Copyright 2014, Wiley-VCH. c) Fabrication process and wiring of the functionalized gate and source–drain fiber of a FSOECT-based fabric sensor. d) Photographs of a FSOECT-based fabric sensor (dark color) embedded in a fabric before and after dissolving the PVA fibers. c,d) Reproduced with permission.[210] Copyright 2018, Wiley-VCH. e) Schematic illustration of fabricating a FSOECT-based tattoo by transfer-printing DBSA-treated PEDOT:PSS films with a hydrogel. f) Photographs of a skin-attachable FSOECT-based tattoo under mechanical deformation. e,f) Reproduced with permission.[133] Copyright 2019, Wiley-VCH.

wich structure of aptamer 1/DA/aptamer 2 is formed, which will increase the local concentration of the redox probe at the gate electrode surface. The transfer characteristics of the aptamer-modified FSOECT to DA exhibits a significant gate voltage shift of 103 mV for a DA concentration of 10 pM and the potential shift increased further when rising the analyte concentration. The resulting shift of gate potential is caused by the potential drop variation at the gate/electrolyte and electrolyte/channel interfaces due to the Faradaic current at the gate electrode induced by the redox group of the formed sandwich structure. Most importantly, the high selectivity of the aptamer-modified FSOECT, exhibiting an ≈6.7-fold greater voltage shift to DA (10 μM) compared with four common interferents, including UA, AA, glutamate, and gamma-aminobutyric acid (100 pM). An ultralow detection limit of 0.5 fM, with a linear detection range from 5 fM to 1 nM, was obtained.

5.1.4. Antibody/Antigen-Based Biomarkers

Biomarkers are crucial for the detection of both normal and abnormal processes in the human body and aid in the diagnosis of certain conditions including cancer. However, in human samples such as blood or serum, biomarkers exist at very low concentrations (approximately femtomolar range) making their detection a significant challenge.[271] OECT-based biosensors are an attractive platform as immunosensors to detect specific antibody–antigen interactions. Generally, either antibodies or antigens can be the immobilized biorecognition molecules on the transducer, which is placed in contact with the analyte solution containing specific antibody/antigen marker to detect the specific antibody–antigen interaction. Usually, two methods are used to functionalize OECTs as immunosensors, including immobilizing antibody or antigen on channel layer[127,272,271] or gate

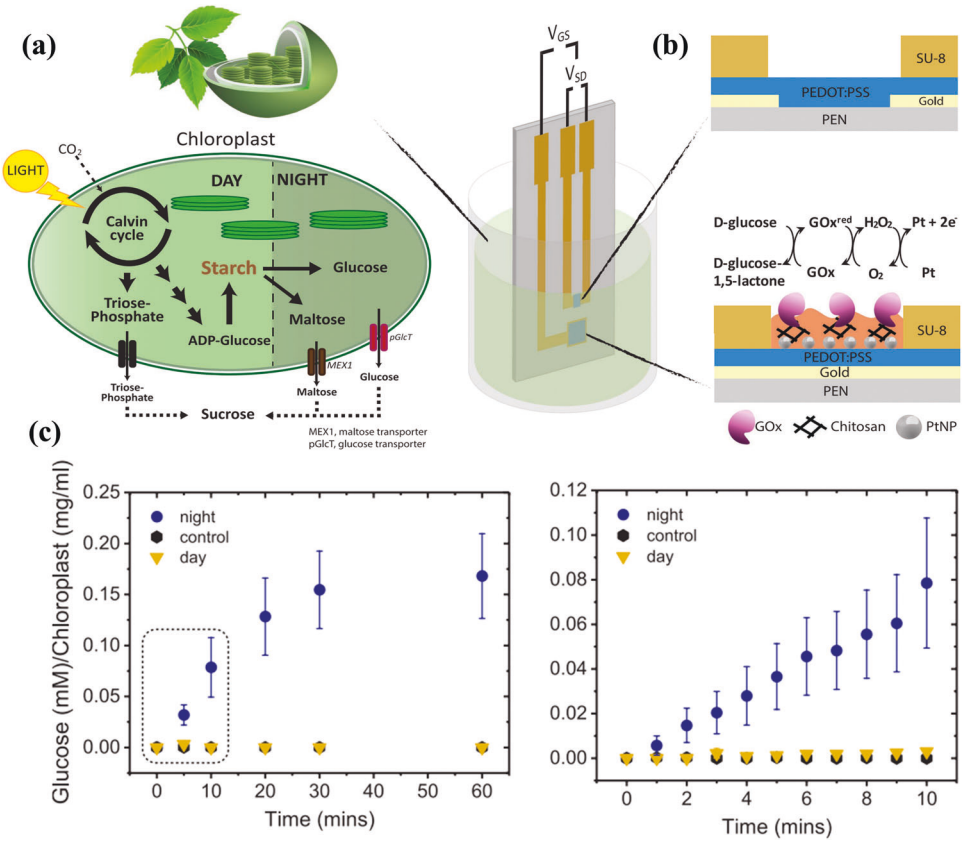

Figure 20. a) Schematic illustration of detecting glucose export from isolated chloroplasts and b) the design of the FSOECT-based glucose sensor. c) Glucose exportation of 0–60 min with 5 min resolution and 0–10 min with 1 min resolution, from nighttime chloroplasts in blue, daytime chloroplasts in yellow, and control response in black. a–c) Reproduced with permission.[132] Copyright 2019, Wiley-VCH.

electrode.[64,273,274] In 2002, Contractor and co-workers[127] first exploited antigen–antibody binding for the design and fabrication of OECT-based immunosensor. They used goat anti-rabbit anti-immunoglobulin G (anti-IgG) and antigen rabbit IgG as the biospecific binding pair. In this work, Au source–drain contacts were first defined on a polycarbonate membrane. Next, a PEDOT layer was electrochemically polymerized on the channel region and functioned as the semiconductor. Importantly, the anti-IgG was mixed in the PEDOT matrix during the polymerization process. Upon antibody–antigen binding, the polymer conformation changes resulting in a variation of the channel film conductivity; in this device, an antigen rabbit IgG concentration as low as 1×10^{-10} g mL^{-1} could be detected with a response time of 3 min.

For gate-modified OECT immunosensors, the surface potential of the gate electrode can be influenced by the antibody–antigen binding affecting the effective gate voltage (V_{GS}^{eff}) of the transistor which, in turn, will affect the doping state of channel layer. Recently, the gate modification strategy has been widely adopted in FSOECT-based immunosensors (Table 5). Torsi and co-workers have systematically investigated immunosensors based on electrolyte-gated transistors,[72,275–279] and recently this group pioneered a printed PEDOT:PSS-FSOECT-based immunosensor for the detection of IgG.[64] The device configuration is shown in **Figure 23**a and consists of thermally evaporated Au source/drain electrodes on flexible PET substrate connected by a layer of printed PEDOT:PSS (thickness: 450 nm). A PDMS well is glued around the channel area and filled with 300 µL of PBS solution (10^{-2} M) acting as the gating medium. The gate electrode consists of a Au-plated Kapton film and was modified with active carboxyl groups to bind with the anti-IgG (Figure 23b). The device transfer characteristics were tested after incubating the same anti-IgG-functionalized gate electrode with several IgG standard solutions having different concentrations (Figure 23c). This FSOECT-based immunosensor can respond to analyte concentrations spanning eight orders of magnitude (from 6 aM to 66 pM), which is well below the detection limits (picomolar range) of the leading enzyme-linked immunosorbent assay.[280] Recently, the outbreak of coronavirus disease (COVID-19) caused by severe acute respiratory syndrome coronavirus 2 (SARS-CoV-2) and its continued spread have seriously threatened public health. A FSOECT-based immunosensor with a gate modification for the detection of SARS-CoV-2 IgG was reported by Yan and co-workers.[55] In this work, the FSOECT was fabricated on a plastic PET substrate in which Au source/drain/gate electrodes were deposited, and an organic channel made of PEDOT:PSS was patterned. A small volume (5 µL) of an aqueous PBS solution was dripped on the PEDOT:PSS surface as the electrolyte (Figure 23d). To construct a portable detection system, the device was connected to a portable meter that was controlled

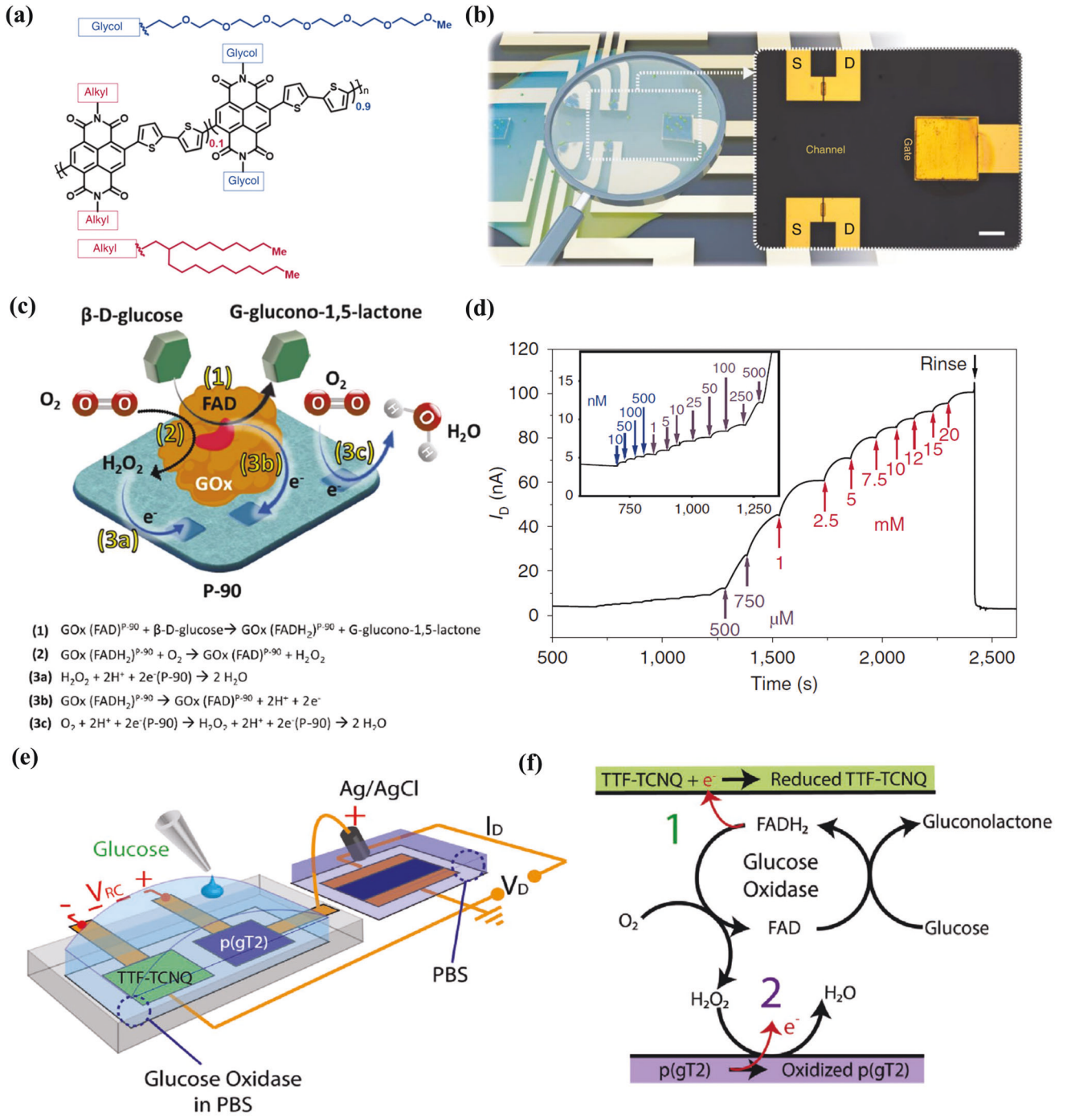

Figure 21. a) Molecular structure of the n-type copolymer P-90. b) Schematic illustration of a P-90-based OECT glucose sensor, where the channel was incubated with GOx solution before measurements. Microscopy image shows two of the P-90 channels alongside a P-90 gate electrode. c) The sensing mechanisms upon oxidation of glucose by GOx at the P-90 interface. d) Current response of the P-90-based OECT glucose sensor to the successive addition of glucose. Inset is the current response under low concentrations (≤500 μM). a–d) Reproduced with permission.[258] Copyright 2019, Springer Nature. e) Scheme of the reaction cell–OECT design, where Ag/AgCl pellet was used as the gate electrode of OECT. f) Schematic illustration of the reactions occurring in the reaction cell. e,f) Reproduced with permission.[260] Copyright 2021, Wiley-VCH.

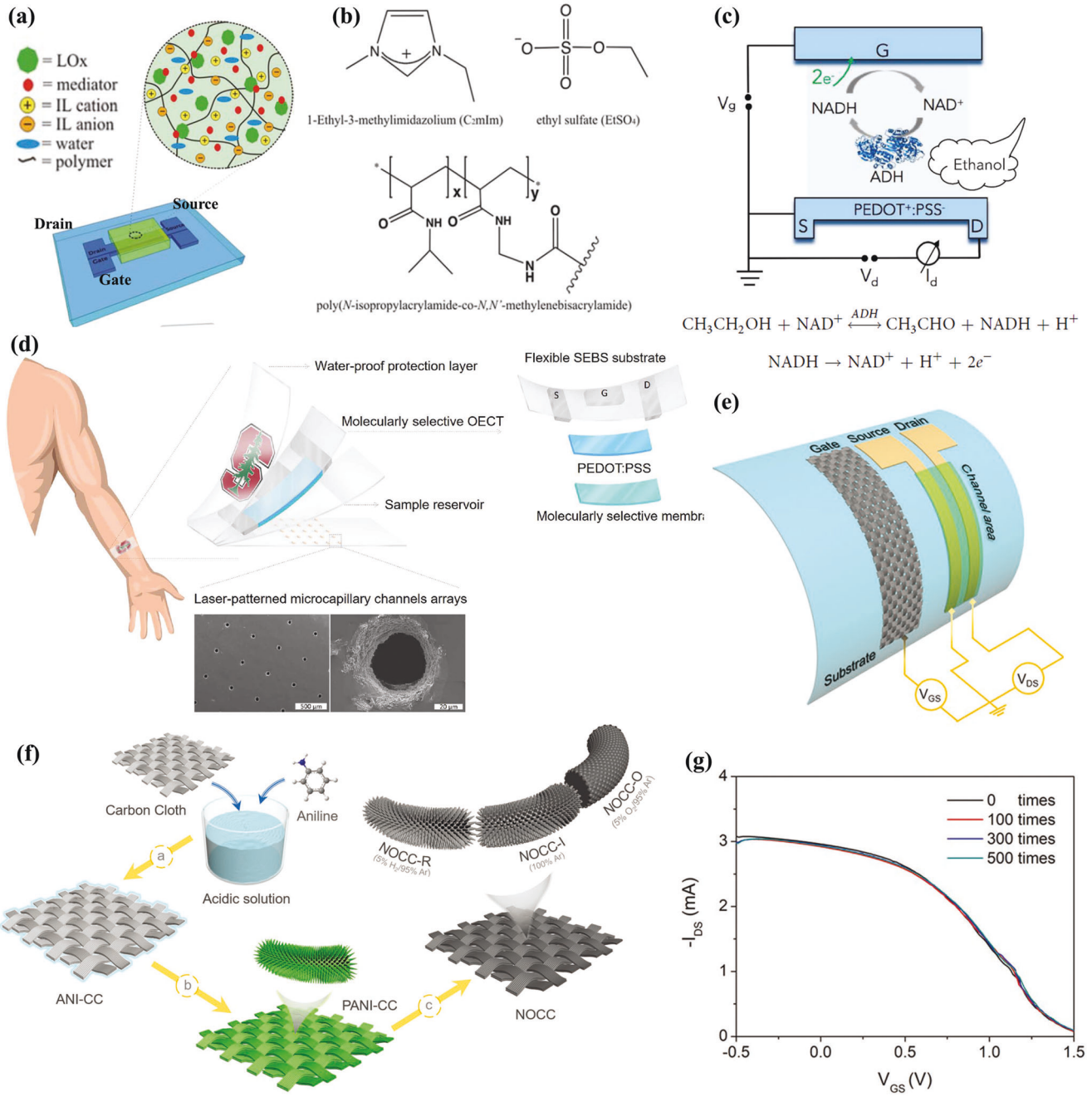

Figure 22. a) Schematic illustration and b) ion gel components of a FSOECT enzymatic sensor with an ion gel/enzyme mixture. a,b) Reproduced with permission.[197] Copyright 2012, Royal Society of Chemistry. c) Enzymatic reaction of ethanol and ADH in an electrolyte solution. Ethanol is oxidized to acetaldehyde, while NAD^+ is reduced to NADH. Reproduced with permission.[173] Copyright 2016, Springer Nature. d) Schematic illustration of a FSOECT-based wearable cortisol sensor, the device comprises a PE-based protection layer, molecularly selective sensing layer on a SEBS substrate, and a laser-patterned layer with microcapillary channel array for sweat acquisition. Reproduced with permission.[179] Copyright 2018, American Association for the Advancement of Science. e,f) Schematic illustration of a flexible carbon-cloth-based FSOECT (e) and the relative fabrication process (f) of a carbon-cloth-based gate electrode. g) Transfer curves of the flexible carbon-cloth-based FSOECTs in a PBS solution after bending. e–g) Reproduced with permission.[211] Copyright 2019, Wiley-VCH.

by a mobile phone through Bluetooth. The gate modification consisted of functionalizing the Au gate electrode with a self-assembled monolayer of mercaptoacetic acid (MAA) through gold–thiol binding. With this approach, the antigens (SARS-CoV-2 spike protein) could be captured on the gate surface through the covalent bond between carboxylic group of the self-assembled monolayer and the amino group of the antigen. After that, bovine serum albumin (BSA) was added to fill the remaining vacancy between modified antigens on the gate electrode surface and to minimize nonspecific bindings induced by interferents. The

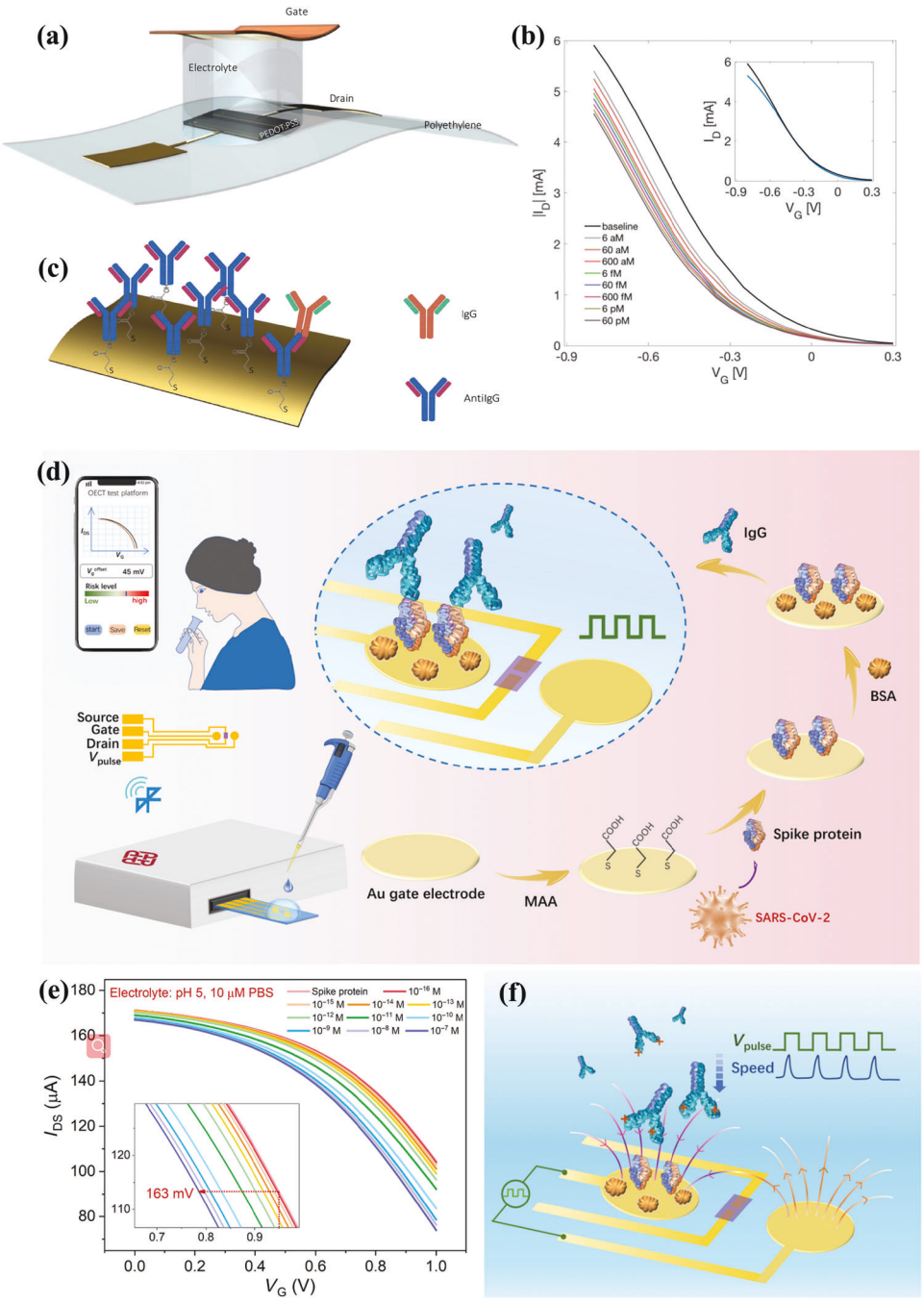

Figure 23. a) Schematic of the printed FSOECT-based immunosensor for detection of IgG. b) Scheme of a self-assembled monolayer for capturing anti-IgGs deposited on the PBS exposed surface of a Au-coated Kapton film. c) Transfer characteristics measured with an anti-IgG gate electrode assayed with several concentrations of IgG ranging from 6 aM to 66 pM. Inset: transfer curves measured before (black line) and after (blue line) the assay. a–c) Reproduced with permission.[64] Copyright 2016, IOP Publishing. d) Scheme of the FSOECT-based immunosensor for the detection of SARS-CoV-2 IgG and the gate modification processes. e) Transfer characteristics after incubation of SARS-CoV-2 IgG with different concentrations in sequence (electrolyte: 10 μM PBS, pH 5.0). f) The scheme of IgG migration under voltage pulses between two electrodes during incubation process. d–f) Reproduced with permission.[55] Copyright 2021, American Association for the Advancement of Science.

transfer curves of these FSOECTs were tested before and after the incubation of a SARS-CoV-2 IgG solution (≤30 min). The results demonstrated that a detection limit as low as 1 fM could be achieved when the pH value of the PBS electrolyte (10 μM) is 5.0 (Figure 23e). Additionally, to enable faster detection, voltage pulses were applied on the gate electrode to reduce the incubation time (Figure 23f) with a 2 min incubation under voltage pulse leading to a detection limit of 1 fM in PBS. For practical applications, the device achieved a detection limit of 10 fM IgG in saliva and serum samples with an incubation time of 5 min.

This work highlights the role of FSOECT-based immunosensors as useful tool in fast and point-of-care detections of COVID-19 antibody.

5.2. Bioelectrical Sensors

Monitoring the electrical physiological activities of organ, tissue, or even cells is of great significance for studying and understanding the functions of biological systems.[281,282] Advancements in bioelectronics have provided novel methods for electrophysiological sensing,[283–285] which provide high sensitivity, superior biocompatibility, and excellent flexibility/stretchability. Based on the detecting targets, the bioelectrical signal sensing of OECTs can be divided into cell activity monitoring and body activity monitoring. In this section, applications and recent progresses of both rigid OECTs and FSOECTs in bioelectrical sensing are reported. Major structure and performance of FSOECT-based sensors are summarized in **Table 6**.

5.2.1. Cell Activity Monitoring

The application of OECTs in cell activity monitoring can be divided into two areas according to the nature of detected cells, which are nonelectrogenic cells and electrogenic cells. The research on nonelectrogenic cells mainly includes cell growth control,[35] cell coverage monitoring,[36] transcellular ion transport,[240] and the integrity of barrier tissues.[37] Among them, research on monitoring the integrity of barrier tissues by OECTs is the most investigated, since the barrier tissue plays a critical role in protecting the body against external factors by modulating the ion flux.[293] Owens and co-workers[37,59,294–296] conducted a systematic and in-depth investigation on the integrity of barrier tissues by utilizing rigid OECTs. Channel current and/or time constant τ of the OECT (τ is obtained by fitting the channel current response to a square pulse of the gate voltage) were used to evaluate the integrity of a barrier tissue.[59] As shown in **Figure 24**a, a planar rigid OECT with a PEDOT:PSS gate electrode and channel was covered with a layer of barrier tissue cells (Madin–Darby canine kidney cells: MDCK-I). The barrier tissue formed by the MDCK-I cells partially blocks the ion flow path of OECT and slowed down the dedoping process, thus the quality of the barrier tissue can be evaluated by measuring τ. Therefore, a larger τ value represents a longer time for dedoping the channel and is thus associated with a healthy, functional barrier-tissue layer. As shown in Figure 24b, after the MDCK-I cells were grown on an OECT for 4 days, trypsin (an enzyme to detach cells from surfaces) was added to the culture medium and the corresponding τ value was recorded simultaneously. The normalized τ value started to decrease after 6 min, which is associated with a faster dedoping of the channel due to the disrupted barrier function of the MDCK-I cell layer. Furthermore, OECTs were also demonstrated to monitor barrier tissue disruption caused by toxins, drugs, and viruses with high temporal resolution, excellent stability in complex matrix, and high sensitivity, which effectively improved the traditional methods limited by cumbersome and expensive procedures.[294–297]

Furthermore, the simple device design of an OECT makes it compatible with established optical characterization techniques commonly used in cell biology. Thus, it is possible to simultaneously measure the barrier resistance corresponding to its integrity and record optical information. Owens and co-workers[59,298] integrated a planar OECT with PEDOT:PSS gate electrode and channel into the established microscope used in cell biology, and constructed a versatile rigid platform for barrier tissue monitoring, which was able to provide cell images with high resolution (≈120 cells over 0.12 mm^2) (Figure 24c) and achieve continuous measurement of the cell behavior (Figure 24d). In addition, since these PEDOT:PSS-based OECTs show satisfactory performance in monitoring barrier tissue integrity, it can also be extended for real-time assessment of nanomaterial toxicity.[299] After adding the nanomaterials into the electrolyte of a planar PEDOT:PSS-based OECT with cells cultured on the device surface, the toxicity could be evaluated by monitoring the physiological state variations of the cells, this method opened up a new prospect in assessing environment toxicity. Since the measurement of barrier tissue integrity does not require highly flexible sensors, FSOECT has been less developed for this type of applications.

In the case of electrogenic cells, such as cardiomyocytes and neurons, behavior monitoring is achieved by recording cell action potential variation during physiological activities. Considering the small size (0.1–5.0 μm) and aggregation of cells, OECTs used for electrogenic cell monitoring are generally constructed as an array capable of recording, and even spatial mapping, the transmission and variation of electrical signals. Hsing and co-workers[286] reported the first study on using a PEDOT:PSS-based rigid OECT and FSOECT arrays for action potential monitoring of cardiomyocyte-like HL-1 cells (**Figure 25**a). Each OECT unit in the array had an active area of 30 × 40 μm^2 and was separated by a distance of 200 μm from each other. The Au source/drain electrodes and interconnects were made by photolithography and encapsulated with anSU-8 layer, and a PEDOT:PSS layer was deposited between the source and drain electrode as the channel material. The HL-1 cells were seeded into the glass ring culture chamber glued on the top of OECT array surface. The as-fabricated OECT array was then characterized in cell culture medium solution with a Ag/AgCl gate electrode. Individual or clusters of cells started to contract spontaneously after the cells covered the surface of the OECTs and formed a dense confluent layer (Figure 25b). Next, the action potential signal was recorded and further processed by a homemade feedback circuit (a 10 kΩ feedback resistor connected to the OECT to convert I_{DS} to a voltage signal at the first operational amplifier). After the voltage signals were filtered by a high pass filter, a SNR higher than 10 dB could be obtained. In addition, the OECT array also demonstrated the capability for chronotropic drug screening by recording the positive chronotropic effect of the action potential from the cells under the stimulation of isoproterenol. As shown in Figure 25c, the frequency of the recorded representative traces of spikes increased by 116.28 ± 18.52% after the treatment of 1 × 10^{-3} M isoproterenol. In addition, the authors also demonstrated that a FSOECT array on a PET substrate and a PDMS chamber for cell culture exhibited comparable SNR, which opened up the possibility of using OECTs in cell mechanobiological studies.

Mayer and co-workers[57] conducted more systematic research using a FSOECT sensing array which realized signal propagation mapping and pharmacological application of cell

Table 6. Flexible and stretchable OECTs for bioelectric signal sensors.

Object	Monitoring application	Substrate	Source/drain	Gate	Channel material	Flexibility	Signal-to-noise ratio (SNR)	Ref.
HL-1 cells	Action potential	PET[a]	Au	Ag/AgCl probe	PEDOT:PSS	N/A	Larger than 4 dB	[286]
HL-1 cells	Action potential	PI[b]	Au	Ag/AgCl probe	PEDOT:PSS	Bending strain: 0.78%; bending radius: 100 µm	N/A	[57]
3T3 fibroblast cell	Cell culturing	PET[a]/PEN[c]	Silver paste	Silver paste	PEDOT:PSS	Flexible	N/A	[287]
Rat brain	ECoG[d]	Parylene	Au	Au/PEDOT:PSS	PEDOT:PSS	N/A	52.7 dB	[56]
Human body	ECG[e]	Parylene	Au	None	PEDOT:PSS	Stretching strain: 30%	24 dB	[196]
Human body	ECG[e]	PLGA[f]	Au	None	PEDOT:PSS	Bending radius: 80 µm	N/A	[214]
Human body	ECG[e]	PDMS[g]	Au	Ag/AgCl wire	PEDOT:PSS	Tensile strain: 60%	12.2 dB	[288]
Human body	ECG[e]	PDMS[g]	Au	Ag/AgCl pellet	p(g2T-T)	Stretching strain: 100%	N/A	[289]
Human body Rat heart	ECG[e]	Levan: [Ch][MA][h]	Au	Au	P3CPT	Bending strain: 1.11%, stretching strain: 5%	N/A	[213]
Human body	EEG[i]	Parylene	Au	Au/PEDOT:PSS–chitosan/ion membrane	PEDOT:PSS	N/A	N/A	[290]
Rat brain	ECoG[d]	Parylene	Au	None	PEDOT:PSS	Compression strain: 50%	13 dB	[58]
Rat heart	ECG[e]	Parylene	Au	None	PEDOT:PSS	Stretching strain: 15%	52 dB	[200]
Rat muscle	EMG[j]	Parylene	Au	None	PEDOT:PSS	N/A	N/A	[215]
Human body Rat heart	ECG[e]	Parylene	Au	None	PEDOT:PSS	Compression strain: 33%	25.9 dB 40.02 dB	[216]
Human body	ECG[e]	Human skin	Au	Au	PEDOT:PSS	Bending radius: 45 µm	21.7 dB	[291]
Human body	ECG[e]	Fibrous nanomesh	Au	None	PEDOT:PSS	N/A	29.0 dB	[292]

[a] Poly(ethylene terephthalate); [b] Polyamide; [c] Poly(ethylene-2,6-naphthalate); [d] Electrocorticography; [e] Electrocardiography; [f] Poly(L-lactide-*co*-glycolide); [g] Poly(dimethylsiloxane); [h] Mixed choline bicarbonate and malic acid; [i] Electroencephalography; [j] Electromyography.

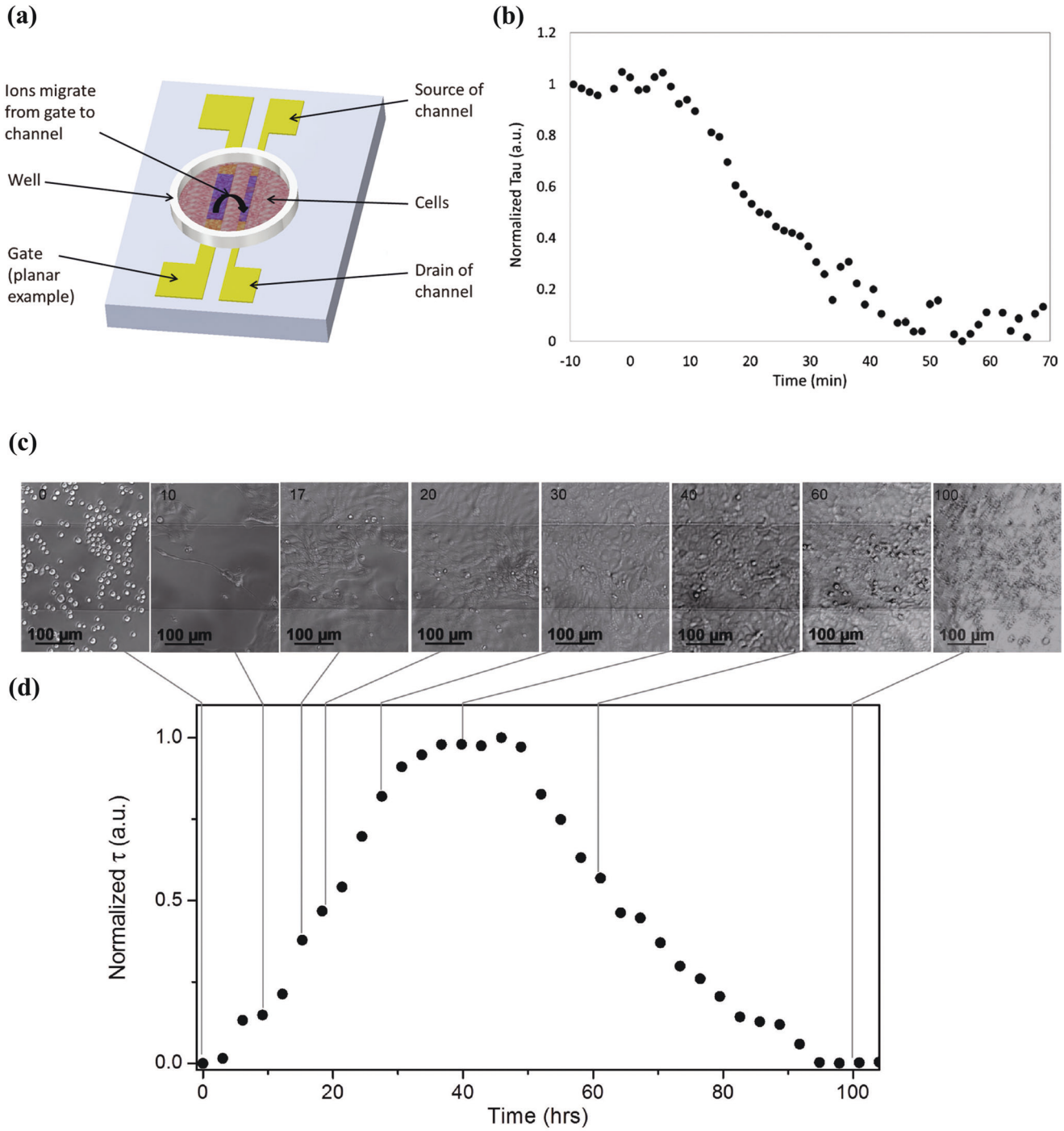

Figure 24. a) Schematic diagram of an OECT with planar PEDOT:PSS gate, where MDCK-I cells grew directly inside a PDMS well on the channel surface. b) The normalized τ value recorded after the addition of trypsin. Trypsin 0.1X (Trypsin 1X corresponds to 0.05 % trypsin with 0.02% ethylenediaminetetraacetic acid) was added at $t = 0$ min. a,b) Reproduced with permission.[59] Copyright 2015, Wiley-VCH. c) Micro-optical images and d) the corresponding electrical characterization of MDCK-I cells on the planar OECT for 4.5 days, and the cells started to separate from the substrate after 50 h due to the unchanged media. c,d) Reproduced with permission.[298] Copyright 2015, Wiley-VCH.

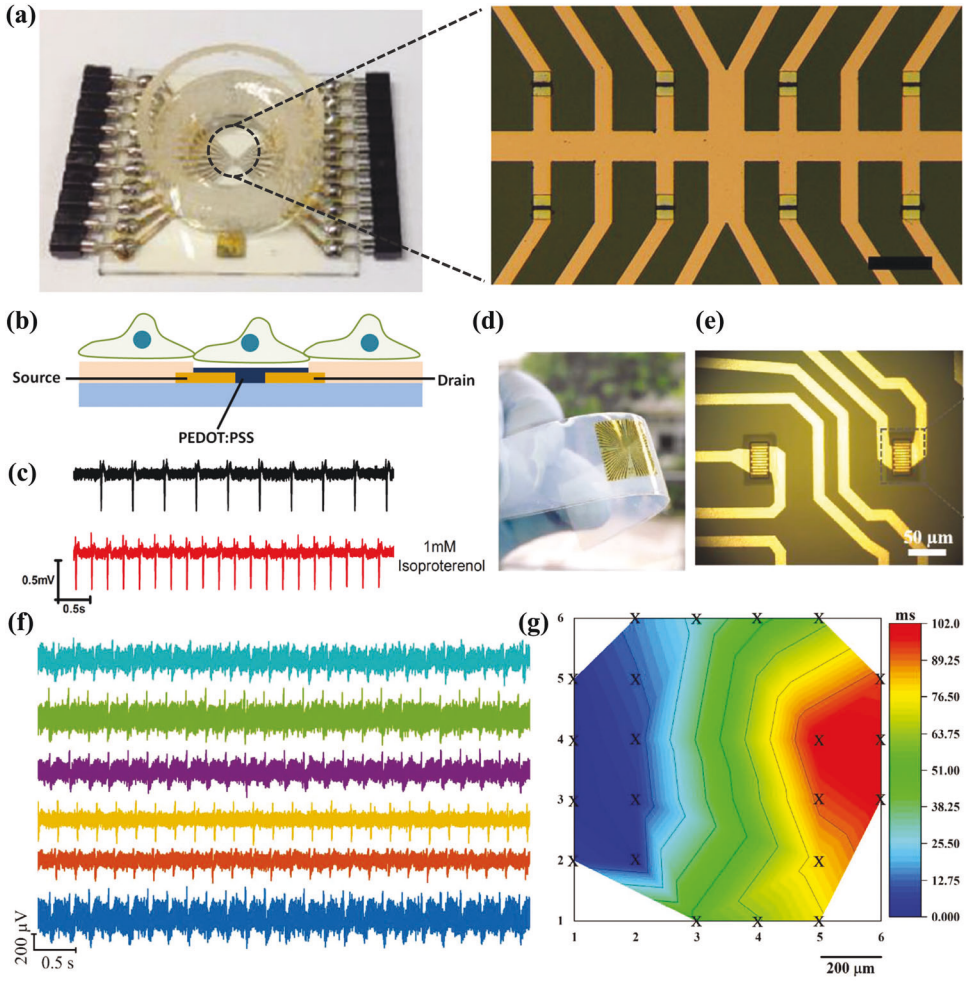

Figure 25. a) Photograph of a PEDOT:PSS-based FSOECT array for the action potential monitoring of HL-1 cells along with an enlarged optical images of channel area. b) Schematic illustration for action potential monitoring of electrogenic cells. c) Representative recorded traces of cells spike before and after the addition of 1×10^{-3} M isoproterenol. a–c) Reproduced with permission.[286] Copyright 2014, Wiley-VCH. d) Image of an FSOECT sensing array with high flexibility and transparency, and e) enlarged optical image of sensing units. f) Different cell action potential shapes recorded on FSOECT array and g) relevant contour map of activation time based on the propagation of cell action potentials. d–g) Reproduced with permission.[57] Copyright 2018, Wiley-VCH.

action potential. In this study, a transparent PEDOT:PSS-based FSOECT matrix (27 functional OECTs) was fabricated on a flexible PI substrate (Figure 25d,e). This device exhibited stable electrical performance under a bending strain up to 0.78%. Next, cardiomyocyte-like HL-1 cells were cultured on the FSOECT array to form a spontaneously contracting cell line, and a home-made amplification circuit based on the fabricated FSOECT sensing array was used to record the action potential. According to the traces of spikes recorded from the different OECT sensing units shown in Figure 25f, it was found that the tested action potential signals exhibit a synchronized beating rate of 5 Hz, along with a SNR of 3–7 dB. Visualization of action potential propagation was also recorded by real-time mapping of tested signals from each OECT unit (Figure 25g). From the contour map, it was observed that the cell action potential has an obvious propagation direction with a propagation velocity of 10 mm s^{-1}. Based on this result, the FSOECT sensing array was used to capture cell response to a drug (norepinephrine: a clinical drug for treating heart disease) stimulation. The authors found a clear relationship between the recorded signals and the drug concentration, where the action potential frequency increases with the concentration of norepinephrine. This work demonstrates that FSOECT sensors can be used for real-time behavior monitoring during cell growth.

5.2.2. Body Activity Monitoring

Monitoring of electrical physiological signals derived from dynamic body status, including information processing of brain and the muscle activities, provides valuable information on the diagnosis of major diseases. Most of these electrical physiological signals originate from low-frequency (<100 Hz) phenomena which are synchronized with the corresponding active cells, such as neurons and muscle cells. Thus, a transistor device (e.g., field-effect transistor) exhibits great advantages in improving the

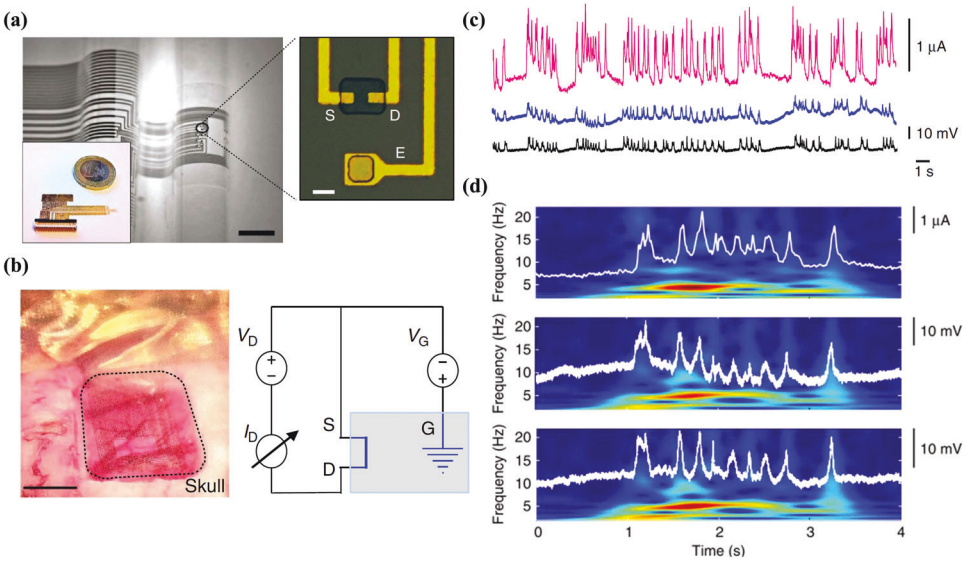

Figure 26. a) Images of ultrathin FSOECT array on parylene substrate. b) In vivo recording of a rat brain activity by FSOECT array, along with the relevant circuit diagram where a blue area indicates the rat brain. c) Recorded rat brain activities from a FSOECT (pink), a PEDOT:PSS electrode (blue), and an Ir-penetrating electrode (black). d) Time–frequency analysis of rat epileptiform activity during a short period, recorded by a FSOECT (top), a PEDOT:PSS surface electrode (middle), and an Ir-penetrating electrode (bottom). a–d) Reproduced with permission.[56] Copyright 2013, Springer Nature.

SNR compared with traditional electrodes due to the local amplification properties endowed by the transistor circuit and promising potential for high-level integration. Moreover, in addition to a high SNR, excellent biocompatibility and great flexibility or conformal body contact are also mandatory for successful in vivo or in vitro wearable testing. FSOECTs, which meet all of the above requirements, have recently demonstrated huge advantages in recording electrical signals of various body activities.

Khodagholy et al.[56] first constructed an ultrathin FSOECT array on a parylene substrate as an electrocorticography (ECoG) probe for the in situ recording of a rat brain activity (**Figure 26**a). As shown in Figure 26b, the OECT array was placed over the somatosensory cortex of a rat brain, and a common source configuration was adopted as the wiring layout of the device. The electrophysiological signals, that is, electric field fluctuations generated by the ion flow during dynamic brain activities, were captured by the OECTs and converted into I_{DS} variations. With this configuration, a SNR of 52.7 dB (peak: 1.3 mA, standard deviation background: 3 nA) could be obtained when monitoring of abnormal brain activities from the Genetic Absence Epilepsy Rat from Strasbourg (Figure 26c), which outperformed those of other traditional electrodes (Ir-penetrating electrodes of an implanted silicon probe: 32.0 dB, PEDOT:PSS surface electrode: 30.2 dB). Besides, the corresponding time–frequency analysis data of different methods during recording the rat epileptiform activity were also compared (Figure 26d). The corresponding time traces were normalized according to the peaks of the activity and demonstrated the improvement of SNR by using OECT. Although the biocompatibility of the proposed flexible OECT array was not reported, which may bring inevitable risks to the animals during the implantable testing, this work provided a new way to realize in vivo real-time monitoring of brain electrical signals with high sensitivity.

In vivo monitoring of electrical signals, such as neural network recording, also requires an optically transparent sensing array to achieve efficient light stimulation. Lee et al.[58] proposed a transparent FSOECT array as an implantable sensor of ECoG signals on an optogenetic rat brain. As shown in **Figure 27**a, the highly flexible and conformable sensor is composed of OECT units and ultrafine rectangular Au grid wiring (line width: 3 μm) and it was fabricated on a parylene substrate (1.2 μm), and the final thickness of the device was ≈3 μm after encapsulation with a SU-8 layer (1.2 μm). Most importantly, since the PEDOT:PSS channel is inherently transparent and semitransparent wirings and electrodes are realized by using ultrafine/thin Au metal grids, the resulting device is also both flexible and transparent. The unique grid structure of this sensor also contributed to the excellent mechanical durability, where the sheet resistance of the Au grid electrode increased only from 3 to 7 Ω sq^{-1} as the compression strain increases to 50%. For the detection of ECoG signals in the rat brain, an as-fabricated 3 × 5 OECT array was coated on the rat brain surface, each OECT unit has a large g_m of 1.1 mS and fast response time of 363 μs. After stimulating the target position of the optogenetic rat brain with a laser beam (473 nm, 40 mW) (Figure 27b), evoked ECoG signals were recorded by the transparent FSOECT array. Figure 27c indicates the recorded ECoG signal with a current amplitude of 0.96 μA measured by the FSOECT at the center of the array (the corresponding electric potential amplitude was calculated by $\Delta I_{DS}/g_m$). Thus, a SNR of 13 dB was achieved with a peak-to-peak noise of 0.2 μA and a root mean square(RMS) noise level of 0.02 μA.

A reliable in vivo wearable sensor also requires the evaluation of the mechanical compliance in the stretched range, as well as the biocompatibility with tested biological systems. Thus, Lee et al.[200] proposed an ultrathin PEDOT:PSS-based FSOECT array sensor with a honeycomb grid-patterned structure. In this work, a 1.2 μm-thick parylene substrate with a honeycomb grid

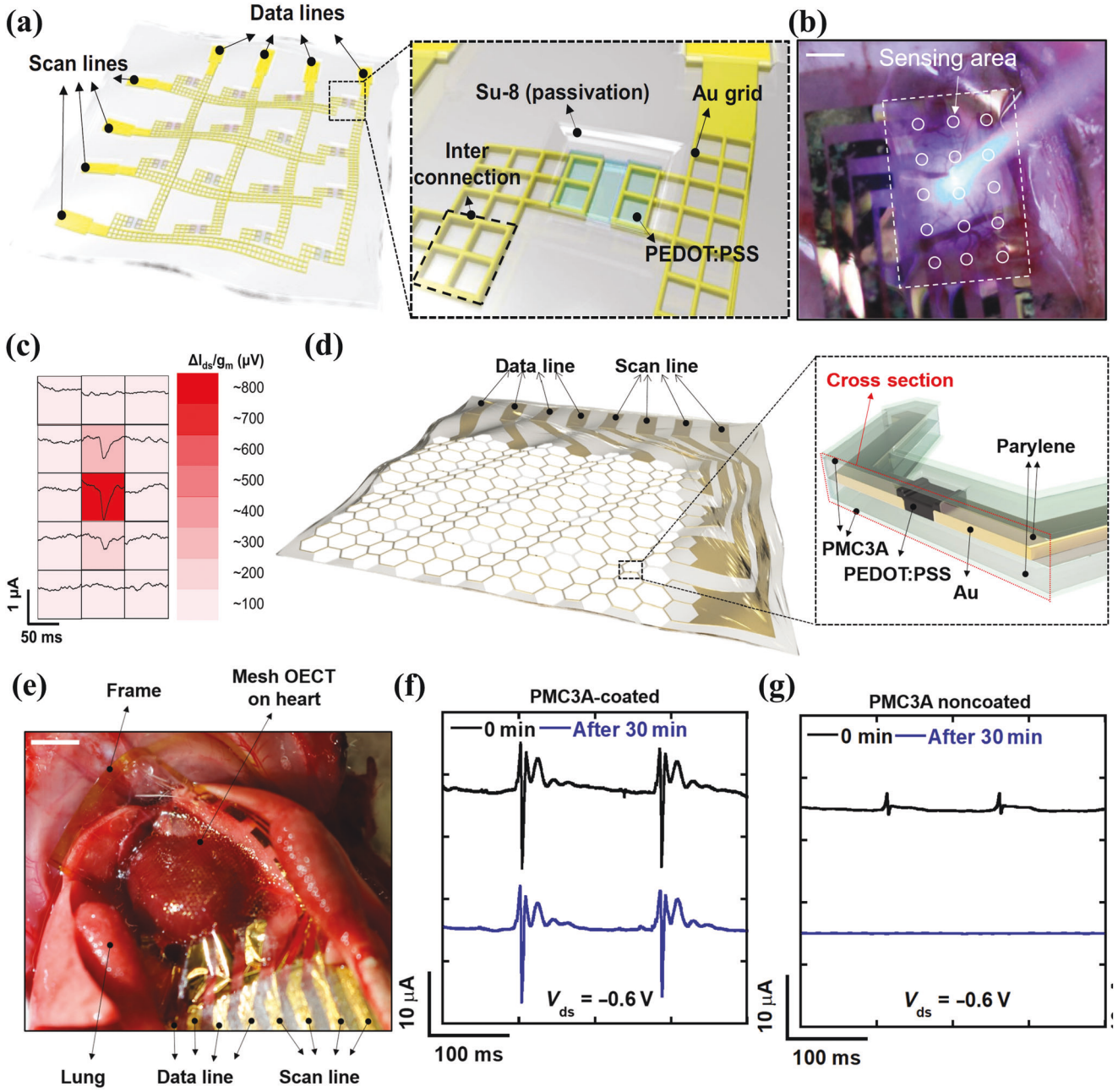

Figure 27. a) Picture of a transparent electrophysiology FSOECT array on a parylene substrate. b) The optical photo of the FSOECT array on the cortical surface of an optogenetic rat, and c) the recorded signals after stimulating by laser beam. a–c) Reproduced with permission.[58] Copyright 2017, National Academy of Science. d) Layout of the highly stretchable active OECT array with honeycomb grid constructed on parylene substrate. e) Optical image of FSOECT array applied in ECG recording on the heart of a rat, and f,g) the detected signals with (f) and without (g) PMC3A coating. d–g) Reproduced with permission.[200] Copyright 2018, American Association for the Advancement of Science.

pattern was first fabricated, then a wiring Au array was deposited on the top to construct the 4 × 4 array sensor (Figure 27d), followed with a top parylene film encapsulation (1.2 μm). The total thickness of the final device was ≈2.6 μm. By testing the transfer characteristics of the OECT array with a Ag/AgCl gate electrode in the PBS electrolyte, the average g_m was ≈1.1 mS. The device mechanical properties were also evaluated and it was found that the g_m and channel current of this FSOECT array decreased by 7% after 1000 stretching cycles (15% strain). Moreover, to address the degradation of response times of OECT induced by the adhered blood clots (platelet accumulation) from surgical bleeding on the OECT channel during the in vivo monitoring, a 100 nm-thick poly(3-methoxypropyl acrylate (PMC3A) layer with excellent ionic conductivity was coated on the channel surface to avoid the platelet accumulation. The as-fabricated FSOECT array was finally attached to the exposed surface of a rat heart to measure

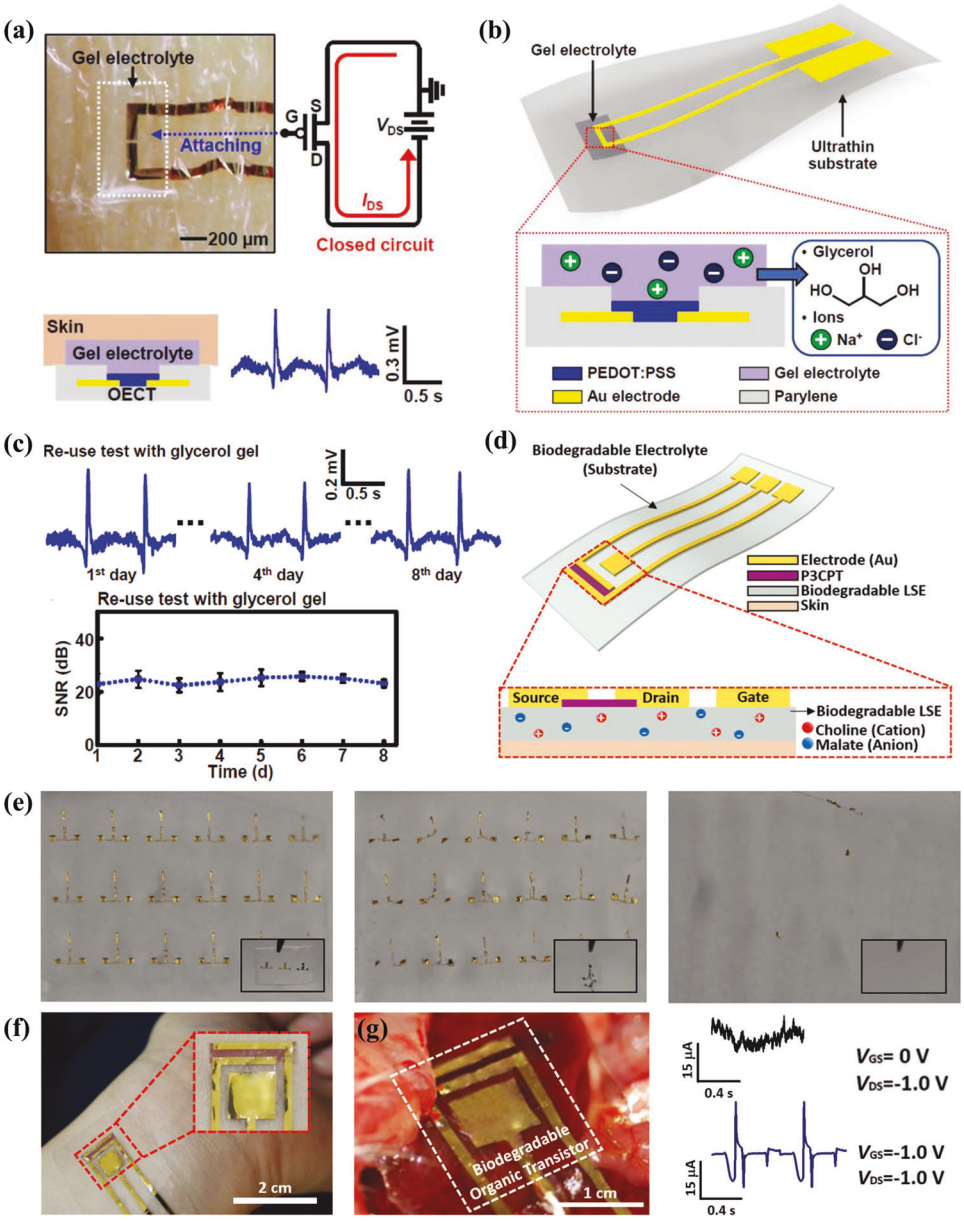

Figure 28. a) Images of a FSOECTs for in vitro ECG monitoring of the human body, along with the electrocardiograms recorded on the skin. b) Schematic of a FSOECT with ultrathin and nonvolatile gel electrolyte. c) ECG signals measured during a testing period of 8 days using the FSOECT sensor with the glycerol gel electrolyte. a–c) Reproduced with permission.[196] Copyright 2019, Wiley-VCH. d) Schematic illustration of an FSOECT based on a biodegradable solid-state layer as substrate and electrolyte. e) Photos of biodegradable FSOECTs immersed in deionized water for 0 (left), 30 (middle), and 120 (right) min, respectively. f,g) The images of biodegradable FSOECTs applied for ECG signals recording from human skin (f) and the heart of a rat (g). d–g) Reproduced with permission.[213] Copyright 2020, Wiley-VCH.

the ECG signals (Figure 27e), revealing a SNR of 52 dB which remained stable even after 30 min of attachment (Figure 27f). As a comparison, the control device without PMC3A encapsulation became inactive under the same conditions (Figure 27g). The high SNR and stability of the FSOECT-based sensor array demonstrated in this work is mainly from the result of the highly conformable structure of this device, as well as the use of PMC3A encapsulation layer preventing the formation of blood clots.

In the case of in vitro monitoring of electrical signals, the use of nonvolatile electrolytes for FSOECTs is advantageous to obtain stable performance in wearable sensing. Someya and coworkers[196] developed an ultrathin and nonvolatile gel electrolyte to construct PEDOT:PSS-based FSOECTs for the in vitro ECG monitoring of a person (**Figure 28**a). The gel electrolyte consisted of a mixture of PVA, acrylamide, and an ion-containing glycerol (Figure 28b). Thus, this device exhibited stable electrical characteristics when an applied strain varied from 0% to 30%. A SNR around 24 dB could be obtained during ECG monitoring up to 8 days (Figure 28c). The authors pointed out that stable ECG monitoring obtained from the gel electrolyte outperformed that

of a hydrogel electrolyte (30 min) and a NaCl aqueous solution (20 min).

To further meet the requirements of biocompatibility for both in vivo and in vitro monitoring applications, Kim and co-workers[213] developed a resorbable and stretchable levan-based solid-state electrolyte (LSE) consisting of levan polysaccharides and an IL (mixed choline bicarbonate and malic acid ([Ch][MA])) for constructing a FSOECT with poly[3-(5-carboxypentyl) thiophene-2,5-diyl] (P3CPT) as p-type channel material. It is worth noting that the solid-state electrolyte also acted as the substrate (Figure 28d). The fabricated LSE could be completely dissolved in deionized water within 2 h since both levan polysaccharides and IL are water soluble (Figure 28e). To demonstrate a fully degradable device that is suitable for in vivo use, the authors replaced the Au electrodes with PEDOT:PSS. This device was first used for in vitro ECG monitoring for 15 days when adhered on the skin of a subject (Figure 28f). Note, the FSOECT could establish a good contact with the human skin since LSE is mainly composed of fructose, which is soft and tacky. Next, in vivo monitoring was demonstrated by measuring the ECG signal by placing the device on a rat heart (Figure 28g). Since the device was made of materials degradable in a body fluid environment, the signal decreased after 20 min of operation. Obviously, the life span of the degradable FSOECT proposed in this work for the in vivo detection is still too short to meet the requirements for practical applications (a Holter monitor for clinic use is typically worn for 1–2 days).

Another new sensor design concept was recently proposed by Spyropoulos et al.,[290] called an ion-gated OECT (IGT), that uses additional mobile ions within the channel semiconductor to achieve a self-(de)doping process, thus eliminating the need for an external electrolyte. The transistor architecture is shown in **Figure 29**a, where the Au gate, source, and drain contacts were deposited in a planar architecture. Then, a PEDOT:PSS (1% (3-glycidyloxypropyl)trimethoxysilane (GOPS)) layer and a chitosan ion membrane were patterned on the gate electrode area by photolithography and plasma reactive ion etching process. Based on the same pattering process, an active channel material consisting of a blend of PEDOT:PSS and D-sorbitol, the latter functioning as an "ion reservoir," was deposited. When a positive voltage was applied, mobile ions within the "ion reservoir" regions in the vicinity of the PEDOT-rich regions of the film compensated the sulfonate anions on the PSS. This process decreased the hole density in the PEDOT and, consequently, reduced the channel current. Because of this architecture, the response time associated with ion movement could be greatly reduced (time constant = 2.6 μs), which is much smaller than that (>10 μs)[79,300,301] of typical electrolyte-gated transistors. A wearable IGT-based sensor was constructed by preparing the IGTs on a 2 μm-thick parylene substrate and was used for human EEG monitoring. This device exhibited several advantages such as comfortable wearing (Figure 29b), miniaturized design (1.5 mm wide) (Figure 29c), and high-quality recording of neurophysiological data, which clearly revealed brain activities.

Someya and co-workers also integrated OECTs with a data reading system and a power source, which further upgraded FSOECT-based sensors to a versatile platform for physiological monitoring.[215,216] In one of the studies,[215] OECTs were integrated with OFETs to realize a flexible (5 × 5) electrophysiology sensing array for data reading from numerous detection points (Figure 29d). The device structure of each OECT + OFET sensing element is shown in Figure 29e, and it comprises the OFET having an Al gate, an AlO_x + *n*-octadecylphosphonic acid (ODPA) hybrid insulator and a dinaphtho[2,3-*b*:2′,3′-*f*]thieno[3,2-*b*]thiophene (DNTT) semiconductor and Au source/drain contacts that were fabricated on a 600 nm-thick parylene substrate. Next, a PEDOT:PSS-based OECT was connected to the OFET through a via hole. The integrated device was operated in a PBS electrolyte with a Ag/AgCl wire as the gate electrode of the OECT. Since the total thickness of the device was only 2.0 μm, stable electrical performance could be retained even after multiple foldings (Figure 29f). Most importantly, the cutoff frequency of this device was ≈3 kHz with a g_m exceeding 1 mS (Figure 29g), which is advantageous for the detection of high frequency biosignals. To evaluate the sensing performance, a single cell comprising one OECT and one OFET was prepared for myoelectric potential recording on a moving muscle. To distinguish the evoked biological signal of the muscle from an artifact resulting from an electrical stimulation, a transgenic rat which expresses a light sensitive gene was used in this work. After coating the device on the muscle tissue surface of the optogenetic mice (Figure 29h), the drain current induced by the light-evoked myoelectric potential was measured. These results demonstrated that a myoelectric potential signal within ≈5 ms involved with the muscle contraction could be recorded. By comparing the signals recorded from the array in the ON and OFF states of the OFETs, it was found that stable monitoring was obtained under repetitive light stimulations at 2, 3, and 5 Hz when the OFETs were switched ON. No signals could be obtained when the OFET was in the OFF state. These data demonstrated that the OECTs were successfully operated by the support of OFETs and the integrated device provides a novel circuit design for a multiarray OECT in an active matrix.

Finally, Someya and co-workers also integrated an energy supply module to construct a self-powered FSOECT-based bioelectric sensor.[216] In this study, an organic photovoltaic (OPV) power source with a high power conversion efficiency of 10.5% was integrated with an OECT on a 1 μm-thick flexible parylene film. For the OPV device proposed in this work, a bulk heterojunction comprising poly[4,8-bis(5-(2-ethylhexyl)thiophen-2-yl)benzo[1,2-*b*;4,5-*b*′]dithiophene-2,6-diyl-alt-(4-octyl-3-fluorothieno[3,4-*b*] thiophene)-2-carboxylate-2-6-diyl] polymer with [6,6]-phenyl-C71-butyric acid methyl ester was used as the photoactive layer, and a solution-processable zinc oxide nanoparticle layer was served as the electron-transporting layer. In addition, the OPV device also consisted of a 100 nm-thick layer of bottomindium tin oxide (ITO) electrode, a 100 nm-thick layer of top Ag electrode, as well as a Cr/Au electrode as the contact pad. The integrated device configuration was shown in **Figure 30**a,b, where the OECT is composed of Cr/Au electrodes as source and drain, patterned PEDOT:PSS layer as channel material, and the top Ag electrode of the OPV device is connected to the drain electrode of the OECT. The integrated device was performed using a solution of PBS as the electrolyte and a Ag/AgCl wire as the gate of the OECT. The introduction of the flexible OPV module avoided unstable output power under mechanical deformation, and further improved the OECT performance by reducing the noise current (0.02 μA)

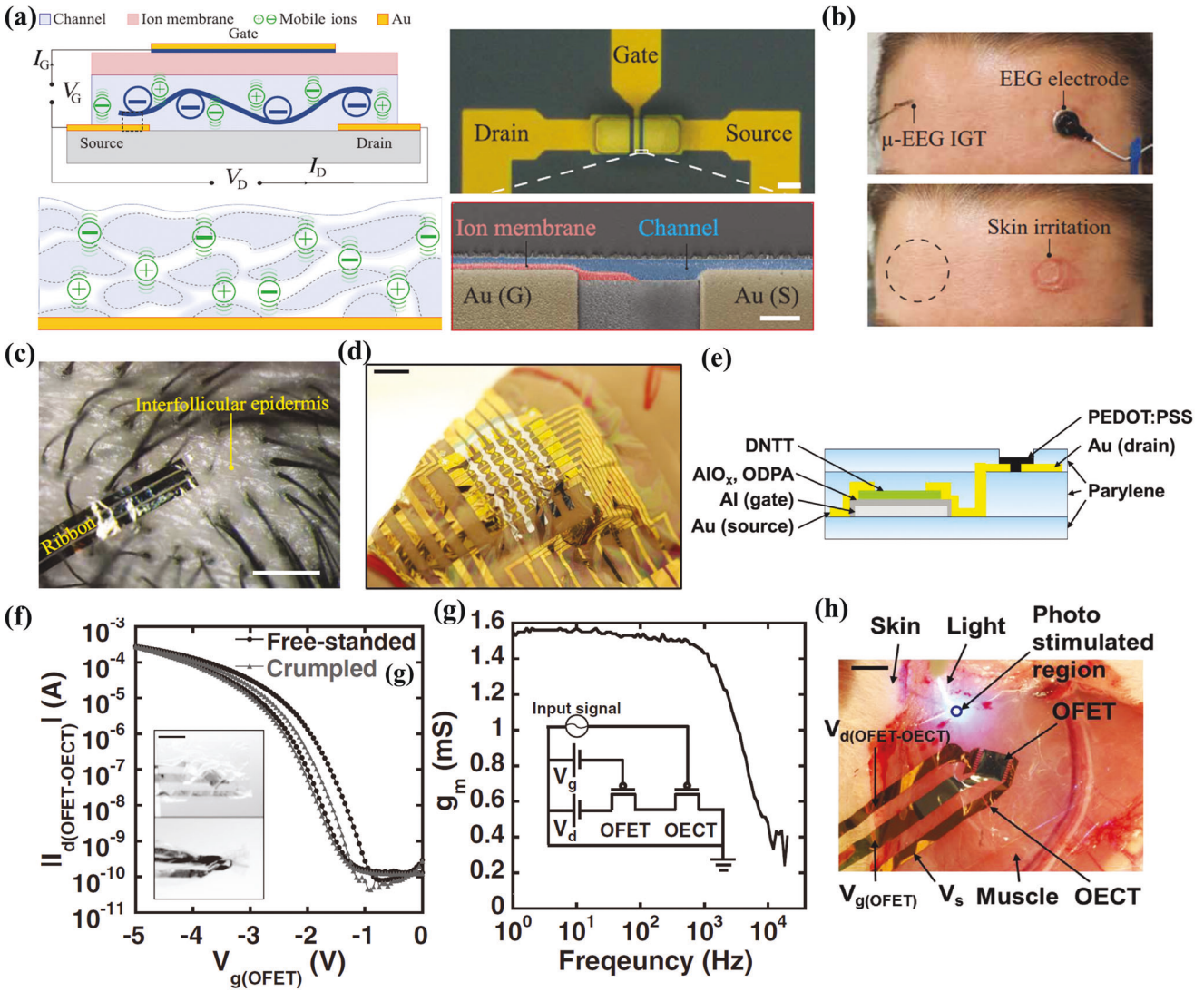

Figure 29. a) Schematic illustration of an ion-gated OECT, along with a top view optical image. b) Images of the ion-gated OECT and conventional clinical EEG electrode applied in human EEG monitoring, and c) an image of the ion-gated OECT with miniaturized design conforming to human scalp. a–c) Reproduced with permission.[290] Copyright 2019, American Association for the Advancement of Science. d) Photo of a 5 × 5 flexible active sensor array constructed on ultrathin parylene substrate, and e) the schematic illustration of an individual pixel consisted of OECT and OFET. f) The transfer curve of the integrated device before and after crumpled. g) The frequency dependence of the transconductance of the flexible integrated device. h) Image of the flexible integrated device for myoelectric potential monitoring on a transgenic rat. d–h) Reproduced with permission.[215] Copyright 2016, Wiley-VCH.

versus that of conventional energy supplies (0.51 μA for source meter, 0.08 μA for AA battery) (Figure 30c). The integrated self-powered device was used for ECG monitoring and showed high SNRs of 25.9 and 40.02 dB from in vitro testing on human skin and in vivo recording on rat heart, respectively (Figure 30d,e). This work demonstrated that self-powered flexible sensors, from the combination of functional OECTs and an OPV power source, offers a new entry to biological signal detection. Inspired by this approach, FSOECT biased by an integrated perovskite solar cell was developed by Yan and co-workers.[304] This device was used as wearable sensors for tracking photoplethysmogram signals and peripheral oxygen saturation under ambient environment.

6. Conclusions

Flexible/stretchable (bio)electronic sensor devices for human health monitoring, monitoring of biological systems and cell/bio-organism functions are of considerable scientific and technological interest. Particularly, high-performance sensors enabling fast detection of biomarkers and information collection on health status at molecular level, as well as new types of biosensors for electrophysiological recording of cells, tissues, organs, and body activities have resulted in considerable research activities. OECTs and OECT-based circuits have the potential to be the most suitable semiconductor devices for these sensing functions, due to the unique mixed ionic–electronic charge transport, biocompatible interfaces between electronics and biological systems,

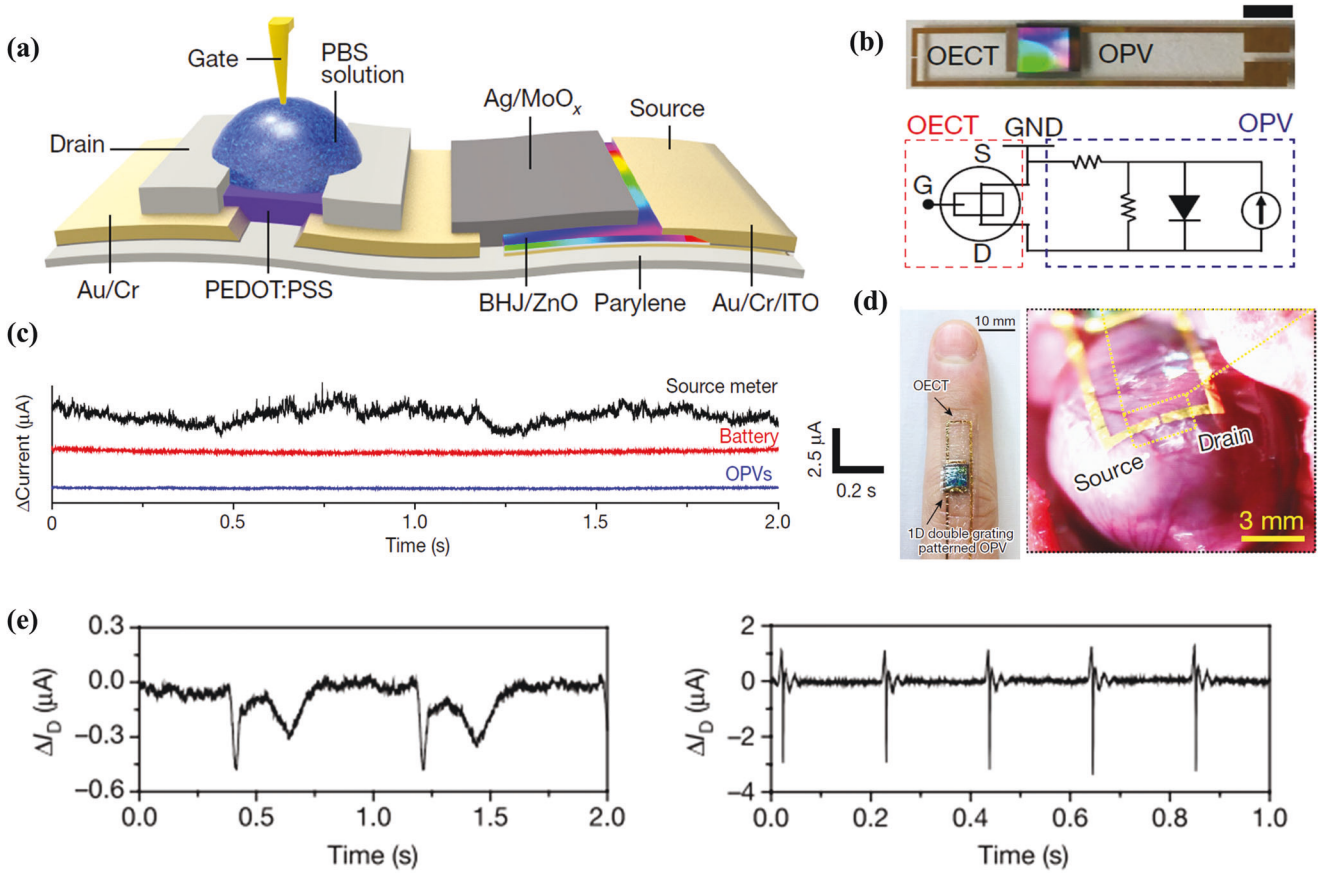

Figure 30. a) Schematic illustration of a self-powered FSOECT integrated with an OPV power source, and b) image of the constructed integrated device and relevant circuit diagram. c) I_{DS} of the OECT when biased by an external source meter (black), a commercial 1.5 V AA battery (red), and an OPV (blue), respectively. d) Optical images and e) the recorded signals of integrated self-powered system applied in ECG recording from human body (left) and a heart of a rat (right). a–e) Reproduced with permission.[216] Copyright 2018, Springer Nature.

functionality in several complex electrolyte environments typical of biological systems, and unique nature of signal amplification favoring high sensitivity and large SNR for both biochemical and bioelectrical sensing mechanisms. Furthermore, OECT components offer integration on plastic and elastic substrates for use on mechanically flexible and/or stretchable (bio)surfaces. Benefitting from these advantages, FSOECT-based biosensors have been further developed by material optimization, structure engineering, as well as exploring new applications. Furthermore, there are impressive advances in fabrication with low-cost printing methods (e.g., 3D printing, room-temperature inkjet printing),[303,302] integration with novel power sources,[304,305] biocompatibility and mechanical compliance,[306,307] and new sensing approaches for early diagnosis of diseases.[308]

However, many challenges remain for broad applicability and commercialization of OECTs, and particularly FSOECTs, for bio-/physiological sensing. First, fidelity and a wide process window for the fabrication process are untested and accurate standard deviation analysis of all OECT performance parameters are not established. Furthermore, most of the existing studies have addressed simple fabrication of a limited number of OECTs/FSOECTs avoiding more complex monolithic integration with other important components needed for complete sensor activities such as control circuits, power generation, and displaying the data.

Specific to FSOECTs, reproducible performance when the device is fabricated on elastomers and fibers as well as stable performance upon mechanical deformations is very limited. Thus, more extensive studies will be necessary to quantify and optimize interfacial adhesion between the different device material components, stacked multifilm crack analysis, and details of the failure mechanisms upon deformation. Furthermore, while studies exploring new and efficient sensing mechanisms in rigid OECT platforms for physiological sensing have made progress lately, these efforts have not yet been fully explored in flexible/stretchable devices, despite the "softer" nature may be advantages for discovering new approaches to sensing functions. Nonetheless, progress in developing flexible/stretchable components, including channel materials, electrodes, and solid electrolytes, is very encouraging. Furthermore, visions for employing FSOECTs for physiological sensing have stimulated experiments in various biological systems which are impossible on rigid platforms. Thus, we firmly believe that FSOECTs will promote a wave of new research in the biomedical arena in the next decade and will create new types of sensor products.

Acknowledgements

This work was financially supported by the National Natural Science Foundation of China (Grant No. 32201648 and 62273073), the China Postdoctoral Science Foundation (Grant No. 2022M712769), the Northwestern University Materials Research Science and Engineering Center (MRSEC NSF Grant No. DMR-2223922). Research in Northwestern University was also financially supported by the AFOSR (Grant Nos. FA9550-18-1-0320 and FA9550-22-1-0423), and Northwestern University (MRSEC grant NSF DMR-1720139 and NSF DMR-2223922).

Conflict of Interest

The authors declare no conflict of interest.

Keywords

biosensing, e-skin, flexible and stretchable electronics, organic electrochemical transistors, physiological sensing

Received: October 26, 2022
Revised: January 31, 2023
Published online: July 6, 2023

[1] Y. Li, *Sci. Program.* **2021**, *2021*, 3739045.
[2] E. Kaniusas, in *Biomedical Signals and Sensors I*, Springer, Berlin, Germany **2012**, pp. 1–26.
[3] E. Kaniusas, in *Biomedical Signals and Sensors I*, Springer, Berlin, Germany **2012**, pp. 183–282.
[4] I. Jeerapan, J. R. Sempionatto, A. Pavinatto, J.-M. You, J. Wang, *J. Mater. Chem. A* **2016**, *4*, 18342.
[5] C. M. Lochner, Y. Khan, A. Pierre, A. C. Arias, *Nat. Commun.* **2014**, *5*, 5745.
[6] S. B. Mondal, S. W. D. Tsen, S. Achilefu, *Adv. Funct. Mater.* **2020**, *30*, 2000185.
[7] K. Mishra, J. P. Fuenzalida-Werner, F. Pennacchietti, R. Janowski, A. Chmyrov, Y. Huang, C. Zakian, U. Klemm, I. Testa, D. Niessing, *Nat. Biotechnol.* **2021**, *40*, 598.
[8] Y. Hattori, L. Falgout, W. Lee, S. Y. Jung, E. Poon, J. W. Lee, I. Na, A. Geisler, D. Sadhwani, Y. Zhang, *Adv. Healthcare Mater.* **2014**, *3*, 1597.
[9] Y. J. Hong, H. Jeong, K. W. Cho, N. Lu, D. H. Kim, *Adv. Funct. Mater.* **2019**, *29*, 1808247.
[10] L. C. Kourtis, O. B. Regele, J. M. Wright, G. B. Jones, *npj Digital Med.* **2019**, *2*, 9.
[11] M. Arnaud, J. Chiffelle, R. Genolet, B. Navarro Rodrigo, M. A. Perez, F. Huber, M. Magnin, T. Nguyen-Ngoc, P. Guillaume, P. Baumgaertner, *Nat. Biotechnol.* **2021**, *40*, 656.
[12] Y. Gu, C. Wang, N. Kim, J. Zhang, T. M. Wang, J. Stowe, R. Nasiri, J. Li, D. Zhang, A. Yang, *Nat. Nanotechnol.* **2021**, *17*, 292.
[13] W. Gao, S. Emaminejad, H. Y. Y. Nyein, S. Challa, K. Chen, A. Peck, H. M. Fahad, H. Ota, H. Shiraki, D. Kiriya, *Nature* **2016**, *529*, 509.
[14] C. B. Huang, S. Witomska, A. Aliprandi, M. A. Stoeckel, M. Bonini, A. Ciesielski, P. Samorì, *Adv. Mater.* **2019**, *31*, 1804600.
[15] H. Montazerian, A. Rashidi, A. Dalili, H. Najjaran, A. S. Milani, M. Hoorfar, *Small* **2019**, *15*, 1804991.
[16] J. Guo, B. Zhou, C. Yang, Q. Dai, L. Kong, *Adv. Funct. Mater.* **2019**, *29*, 1902898.
[17] A. M. Nightingale, C. L. Leong, R. A. Burnish, S.-u. Hassan, Y. Zhang, G. F. Clough, M. G. Boutelle, D. Voegeli, X. Niu, *Nat. Commun.* **2019**, *10*, 2741.
[18] Y. Pang, K. Zhang, Z. Yang, S. Jiang, Z. Ju, Y. Li, X. Wang, D. Wang, M. Jian, Y. Zhang, *ACS Nano* **2018**, *12*, 2346.
[19] D. Son, J. Lee, S. Qiao, R. Ghaffari, J. Kim, J. E. Lee, C. Song, S. J. Kim, D. J. Lee, S. W. Jun, *Nat. Nanotechnol.* **2014**, *9*, 397.
[20] W. Wu, H. Haick, *Adv. Mater.* **2018**, *30*, 1705024.
[21] Y. Bonnassieux, C. J. Brabec, Y. Cao, T. B. Carmichael, M. L. Chabinyc, K.-T. Cheng, G. Cho, A. Chung, C. L. Cobb, A. Distler, H.-J. Egelhaaf, G. Grau, X. Guo, G. Haghiashtiani, T.-C. Huang, M. M. Hussain, B. Iniguez, T.-M. Lee, L. Li, Y. Ma, D. Ma, M. C. McAlpine, T. N. Ng, R. Österbacka, S. N. Patel, J. Peng, H. Peng, J. Rivnay, et al., *Flexible Printed Electron.* **2021**, *6*, 023001.
[22] B. Wang, W. Huang, L. Chi, M. Al-Hashimi, T. J. Marks, A. Facchetti, *Chem. Rev.* **2018**, *118*, 5690.
[23] A. Tricoli, N. Nasiri, S. De, *Adv. Funct. Mater.* **2017**, *27*, 1605271.
[24] Y. Khan, F. J. Pavinatto, M. C. Lin, A. Liao, S. L. Swisher, K. Mann, V. Subramanian, M. M. Maharbiz, A. C. Arias, *Adv. Funct. Mater.* **2016**, *26*, 1004.
[25] Y. Liu, M. Pharr, G. A. Salvatore, *ACS Nano* **2017**, *11*, 9614.
[26] A. C. Myers, H. Huang, Y. Zhu, *RSC Adv.* **2015**, *5*, 11627.
[27] H. S. White, G. P. Kittlesen, M. S. Wrighton, *J. Am. Chem. Soc.* **1984**, *106*, 5375.
[28] D. A. Bernards, D. J. Macaya, M. Nikolou, J. A. Defranco, S. Takamatsu, G. G. Malliaras, *J. Mater. Chem.* **2007**, *18*, 116.
[29] D. J. Macaya, M. Nikolou, S. Takamatsu, J. T. Mabeck, R. M. Owens, *Sens. Actuators, B* **2007**, *123*, 374.
[30] S. N. Young, D. A. Bernards, D. J. Macaya, J. A. Defranco, N. Maria, R. M. Owens, G. G. Malliaras, *Sensors* **2009**, *9*, 9896.
[31] E. J. Strand, E. Bihar, S. M. Gleason, S. Han, S. W. Schreiber, M. N. Renny, G. G. Malliaras, R. R. McLeod, G. L. Whiting, *Adv. Electron. Mater.* **2021**, *8*,2100853.
[32] C. Chen, Q. Song, W. Lu, Z. Zhang, Y. Yu, X. Liu, R. He, *RSC Adv.* **2021**, *11*, 37917.
[33] B. Burtscher, P. A. Manco Urbina, C. Diacci, S. Borghi, M. Pinti, A. Cossarizza, C. Salvarani, M. Berggren, F. Biscarini, D. T. Simon, *Adv. Healthcare Mater.* **2021**, *10*, 2100955.
[34] L. M. M. Ferro, L. Merces, D. H. S. de Camargo, C. C. B. Bufon, *Adv. Mater.* **2021**, *33*, 2101518.
[35] M. H. Bolin, K. Svennersten, D. Nilsson, A. Sawatdee, E. W. Jager, A. Richter-Dahlfors, M. Berggren, *Adv. Mater.* **2009**, *21*, 4379.
[36] L. Peng, Y. Feng, Y. Jinjiang, H. L. W. Chan, Y. Mo, *Adv. Mater.* **2010**, *22*, 3655.
[37] L. H. Jimison, S. A. Tria, D. Khodagholy, M. Gurfinkel, E. Lanzarini, A. Hama, G. G. Malliaras, R. M. Owens, *Adv. Mater.* **2012**, *24*, 5919.
[38] N. Cacocciola, M. Parmeggiani, M. Segantini, A. Verna, D. Baruffaldi, S. Villata, F. Frascella, S. L. Marasso, G. Canavese, M. Cocuzza, *Biomed. Sci. Eng.* **2021**, *4*, 160.
[39] Y. Jimbo, D. Sasaki, T. Ohya, S. Lee, W. Lee, F. A. Hassani, T. Yokota, K. Matsuura, S. Umezu, T. Shimizu, *Proc. Natl. Acad. Sci. USA* **2021**, *118*, e2022300118.
[40] K. Lieberth, P. Romele, F. Torricelli, D. A. Koutsouras, M. Brückner, V. Mailänder, P. Gkoupidenis, P. W. Blom, *Adv. Healthcare Mater.* **2021**, *10*, 2100845.
[41] P. Leleux, J. Rivnay, T. Lonjaret, J. M. Badier, C. Bénar, T. Hervé, P. Chauvel, G. G. Malliaras, *Adv. Healthcare Mater.* **2015**, *4*, 142.
[42] J. Rivnay, P. Leleux, M. Ferro, M. Sessolo, A. Williamson, D. A. Koutsouras, D. Khodagholy, M. Ramuz, X. Strakosas, R. M. Owens, *Sci. Adv.* **2015**, *1*, e1400251.
[43] M. Braendlein, T. Lonjaret, P. Leleux, J. M. Badier, G. G. Malliaras, *Adv. Sci.* **2017**, *4*, 1600247.
[44] A. Nawaz, Q. Liu, W. L. Leong, K. E. Fairfull-Smith, P. Sonar, *Adv. Mater.* **2021**, *33*, 2101874.
[45] J. E. Tyrrell, K. Petkos, E. M. Drakakis, M. G. Boutelle, A. J. Campbell, *Adv. Funct. Mater.* **2021**, *31*, 2103385.

[46] D. T. Simon, E. O. Gabrielsson, K. Tybrandt, M. Berggren, *Chem. Rev.* **2016**, *116*, 13009.
[47] C. Liao, F. Yan, *Polym. Rev.* **2013**, *53*, 352.
[48] A.-M. Pappa, O. Parlak, G. Scheiblin, P. Mailley, A. Salleo, R. M. Owens, *Trends Biotechnol.* **2018**, *36*, 45.
[49] T. Blaudeck, P. A. Ersman, M. Sandberg, S. Heinz, A. Laiho, J. Liu, I. Engquist, M. Berggren, R. R. Baumann, *Adv. Electron. Mater.* **2012**, *22*, 2939.
[50] L. Basiricò, P. Cosseddu, B. Fraboni, A. Bonfiglio, *Thin Solid Films* **2011**, *520*, 1291.
[51] L. Basiricò, P. Cosseddu, A. Scidà, B. Fraboni, G. Malliaras, A. Bonfiglio, *Org. Electron.* **2012**, *13*, 244.
[52] N. Kaihovirta, T. Mäkelä, X. He, C.-J. Wikman, C.-E. Wilén, R. Österbacka, *Org. Electron.* **2010**, *11*, 1207.
[53] P. A. Ersman, D. Nilsson, J. Kawahara, G. Gustafsson, M. Berggren, *Org. Electron.* **2013**, *14*, 1276.
[54] P. Lin, F. Yan, *Adv. Mater.* **2012**, *24*, 34.
[55] H. Liu, A. Yang, J. Song, N. Wang, P. Lam, Y. Li, H. K.-W. Law, F. Yan, *Sci. Adv.* **2021**, *7*, eabg8387.
[56] D. Khodagholy, T. Doublet, P. Quilichini, M. Gurfinkel, P. Leleux, A. Ghestem, E. Ismailova, T. Hervé, S. Sanaur, C. Bernard, G. G. Malliaras, *Nat. Commun.* **2013**, *4*, 1575.
[57] Y. Liang, M. Ernst, F. Brings, D. Kireev, V. Maybeck, A. Offenhäusser, D. Mayer, *Adv. Healthcare Mater.* **2018**, *7*, 1800304.
[58] W. Lee, D. Kim, N. Matsuhisa, M. Nagase, M. Sekino, G. G. Malliaras, T. Yokota, T. Someya, *Proc. Natl. Acad. Sci. USA* **2017**, *114*, 10554.
[59] M. Ramuz, K. Margita, A. Hama, P. Leleux, J. Rivnay, I. Bazin, R. M. Owens, *ChemPhysChem* **2015**, *16*, 1210.
[60] S. Y. Yang, J. A. Defranco, Y. A. Sylvester, T. J. Gobert, D. J. Macaya, R. M. Owens, G. G. Malliaras, *Lab Chip* **2009**, *9*, 704.
[61] J. T. Mabeck, J. A. Defranco, D. A. Bernards, G. G. Malliaras, S. Hocde, C. J. Chase, *Appl. Phys. Lett.* **2005**, *87*, 99.
[62] A. Koklu, S. Wustoni, V.-E. Musteata, D. Ohayon, M. Moser, I. McCulloch, S. P. Nunes, S. Inal, *ACS Nano* **2021**, *15*, 8130.
[63] H. Ling, S. Liu, Z. Zheng, F. Yan, *Small Methods* **2018**, *2*, 1800070.
[64] E. Macchia, P. Romele, K. Manoli, M. Ghittorelli, M. Magliulo, Z. M. Kovács-Vajna, F. Torricelli, L. Torsi, *Flexible Printed Electron.* **2018**, *3*, 034002.
[65] L. Caizhi, M. Chunhin, Z. Meng, H. L. W. Chan, Y. Feng, *Adv. Mater.* **2015**, *27*, 676.
[66] X. Strakosas, M. Bongo, R. M. Owens, *J. Appl. Polym. Sci.* **2015**, *132*, 41735.
[67] J. Liao, H. Si, X. Zhang, S. Lin, *Sensors* **2019**, *19*, 218.
[68] N. Wang, A. Yang, Y. Fu, Y. Li, F. Yan, *Acc. Chem. Res.* **2019**, *52*, 277.
[69] H. Sun, J. Y. Gerasimov, M. Berggren, S. Fabiano, *J. Mater. Chem. C* **2018**, *6*, 11778.
[70] W. Huang, J. Chen, G. Wang, Y. Yao, X. Zhuang, R. M. Pankow, Y. Cheng, T. J. Marks, A. Facchetti, *J. Mater. Chem. C* **2021**, *9*, 9348.
[71] J. Rivnay, S. Inal, A. Salleo, R. M. Owens, M. Berggren, G. G. Malliaras, *Nat. Rev. Mater.* **2018**, *3*, 17086.
[72] F. Torricelli, D. Z. Adrahtas, Z. Bao, M. Berggren, F. Biscarini, A. Bonfiglio, C. A. Bortolotti, C. D. Frisbie, E. Macchia, G. G. Malliaras, I. McCulloch, M. Moser, T.-Q. Nguyen, R. M. Owens, A. Salleo, A. Spanu, L. Torsi, *Nat. Rev. Methods Primers* **2021**, *1*, 66.
[73] K. Manoli, M. Magliulo, M. Y. Mulla, M. Singh, L. Sabbatini, G. Palazzo, L. Torsi, *Angew. Chem., Int. Ed.* **2015**, *54*, 12562.
[74] N. Lago, A. Cester, *Appl. Sci.* **2017**, *7*, 1292.
[75] W. Lee, T. Someya, *Chem. Mater.* **2019**, *31*, 6347.
[76] L. Wang, X. Yue, Q. Sun, L. Zhang, G. Ren, G. Lu, H.-D. Yu, W. Huang, *Nano Res.* **2022**, *15*, 2433.
[77] H. Sirringhaus, *Adv. Mater.* **2014**, *26*, 1319.
[78] H. Koezuka, A. Tsumura, T. Ando, *Synth. Met.* **1987**, *18*, 699.
[79] D. Khodagholy, J. Rivnay, M. Sessolo, M. Gurfinkel, P. Leleux, L. H. Jimison, E. Stavrinidou, T. Herve, S. Sanaur, R. M. Owens, G. G. Malliaras, *Nat. Commun.* **2013**, *4*, 2133.
[80] D. Zhao, S. Fabiano, M. Berggren, X. Crispin, *Nat. Commun.* **2017**, *8*, 14214.
[81] Y. Xia, W. Zhang, M. Ha, J. H. Cho, M. J. Renn, C. H. Kim, C. D. Frisbie, *Adv. Funct. Mater.* **2010**, *20*, 587.
[82] A. Facchetti, *Chem. Mater.* **2011**, *23*, 733.
[83] H. Sun, X. Guo, A. Facchetti, *Chem* **2020**, *6*, 1310.
[84] L. Torsi, M. Magliulo, K. Manoli, G. Palazzo, *Chem. Soc. Rev.* **2013**, *42*, 8612.
[85] R. P. Ortiz, A. Facchetti, T. J. Marks, *Chem. Rev.* **2010**, *110*, 205.
[86] X. Guo, A. Facchetti, T. J. Marks, *Chem. Rev.* **2014**, *114*, 8943.
[87] A. Giovannitti, D.-T. Sbircea, S. Inal, C. B. Nielsen, E. Bandiello, D. A. Hanifi, M. Sessolo, G. G. Malliaras, I. McCulloch, J. Rivnay, *Proc. Natl. Acad. Sci. USA* **2016**, *113*, 12017.
[88] Z. Wang, X. Zhuang, Y. Chen, B. Wang, J. Yu, W. Huang, T. J. Marks, A. Facchetti, *Chem. Mater.* **2019**, *31*, 7608.
[89] L. Kergoat, B. Piro, M. Berggren, G. Horowitz, M.-C. Pham, *Anal. Bioanal. Chem.* **2012**, *402*, 1813.
[90] S. N. Afraj, C. C. Lin, A. Velusamy, C. H. Cho, H. Y. Liu, J. Chen, G. H. Lee, J. C. Fu, J. S. Ni, S. H. Tung, *Adv. Funct. Mater.* **2022**, *32*, 2200880.
[91] K. Stallings, R. Turrisi, Y. Chen, L. Zeng, B. Wang, J. Smith, M. J. Bedzyk, L. Beverina, A. Facchetti, T. J. Marks, *ACS Appl. Electron. Mater.* **2022**, *4*, 2015.
[92] J. Wu, Y. Chen, J. Liu, Z. Pang, G. Li, Z. Lu, Y. Huang, A. Facchetti, T. J. Marks, *J. Mater. Chem. C* **2022**, *10*, 2724.
[93] H. Guo, C.-Y. Yang, X. Zhang, A. Motta, K. Feng, Y. Xia, Y. Shi, Z. Wu, K. Yang, J. Chen, *Nature* **2021**, *599*, 67.
[94] H. Yan, Z. Chen, Y. Zheng, C. Newman, J. R. Quinn, F. Dötz, M. Kastler, A. Facchetti, *Nature* **2009**, *457*, 679.
[95] X. Zhuang, J.-S. Kim, W. Huang, Y. Chen, G. Wang, J. Chen, Y. Yao, Z. Wang, F. Liu, J. Yu, *Proc. Natl. Acad. Sci. USA* **2023**, *120*, e2216672120.
[96] J. Kim, J. B. Park, D. Zheng, J. S. Kim, Y. Cheng, S. K. Park, W. Huang, T. J. Marks, A. Facchetti, *Adv. Mater.* **2022**, *34*, 2205871.
[97] K. Stallings, J. Smith, Y. Chen, L. Zeng, B. Wang, G. Di Carlo, M. J. Bedzyk, A. Facchetti, T. J. Marks, *ACS Appl. Mater. Interfaces* **2021**, *13*, 15399.
[98] X. Zhuang, S. Patel, C. Zhang, B. Wang, Y. Chen, H. Liu, V. P. Dravid, J. Yu, Y.-Y. Hu, W. Huang, *J. Am. Chem. Soc.* **2020**, *142*, 12440.
[99] W. Huang, P.-H. Chien, K. McMillen, S. Patel, J. Tedesco, L. Zeng, S. Mukherjee, B. Wang, Y. Chen, G. Wang, *Proc. Natl. Acad. Sci. USA* **2020**, *117*, 18231.
[100] Z. Wang, X. Zhuang, B. Wang, W. Huang, T. J. Marks, A. Facchetti, *Adv. Funct. Mater.* **2021**, *31*, 2100451.
[101] B. Wang, X. Yu, P. Guo, W. Huang, L. Zeng, N. Zhou, L. Chi, M. J. Bedzyk, R. P. Chang, T. J. Marks, *Adv. Electron. Mater.* **2016**, *2*, 1500427.
[102] A. Giovannitti, C. B. Nielsen, D.-T. Sbircea, S. Inal, M. Donahue, M. R. Niazi, D. A. Hanifi, A. Amassian, G. G. Malliaras, J. Rivnay, I. McCulloch, *Nat. Commun.* **2016**, *7*, 13066.
[103] A. Savva, D. Ohayon, J. Surgailis, A. F. Paterson, T. C. Hidalgo, X. Chen, I. P. Maria, B. D. Paulsen, A. J. Petty, J. Rivnay, *Adv. Electron. Mater.* **2019**, *5*, 1900249.
[104] H. Sun, M. Vagin, S. Wang, X. Crispin, R. Forchheimer, M. Berggren, S. Fabiano, *Adv. Mater.* **2018**, *30*, 1704916.
[105] H. Y. Wu, C. Y. Yang, Q. Li, N. B. Kolhe, X. Strakosas, M. A. Stoeckel, Z. Wu, W. Jin, M. Savvakis, R. Kroon, D. Tu, H. Y. Woo, M. Berggren, S. A. Jenekhe, S. Fabiano, *Adv. Mater.* **2021**, *34*, 2106235.
[106] D. Ohayon, A. Savva, W. Du, B. D. Paulsen, I. Uguz, R. S. Ashraf, J. Rivnay, I. McCulloch, S. Inal, *ACS Appl. Mater. Interfaces* **2021**, *13*, 4253.

[107] A. Giovannitti, I. P. Maria, D. Hanifi, M. J. Donahue, D. Bryant, K. J. Barth, B. E. Makdah, A. Savva, D. Moia, M. Zetek, P. R. F. Barnes, O. G. Reid, S. Inal, G. Rumbles, G. G. Malliaras, J. Nelson, J. Rivnay, I. McCulloch, *Chem. Mater.* **2018**, *30*, 2945.
[108] S. Griggs, A. Marks, H. Bristow, I. McCulloch, *J. Mater. Chem. C* **2021**, *9*, 8099.
[109] S. Inal, G. G. Malliaras, J. Rivnay, *Nat. Commun.* **2017**, *8*, 1767.
[110] V. Venkatraman, J. T. Friedlein, A. Giovannitti, I. P. Maria, I. McCulloch, R. R. McLeod, J. Rivnay, *Adv. Sci.* **2018**, *5*, 1800453.
[111] A. Savva, R. Hallani, C. Cendra, J. Surgailis, T. C. Hidalgo, S. Wustoni, R. Sheelamanthula, X. Chen, M. Kirkus, A. Giovannitti, *Adv. Funct. Mater.* **2020**, *30*, 1907657.
[112] D. A. Bernards, G. G. Malliaras, *Adv. Funct. Mater.* **2007**, *17*, 3538.
[113] J. T. Friedlein, S. E. Shaheen, G. G. Malliaras, R. R. McLeod, *Adv. Electron. Mater.* **2015**, *1*, 1500189.
[114] V. Kaphle, S. Liu, A. Al-Shadeedi, C. M. Keum, B. Lüssem, *Adv. Mater.* **2016**, *28*, 8766.
[115] J. T. Friedlein, J. Rivnay, D. H. Dunlap, I. McCulloch, S. E. Shaheen, R. R. McLeod, G. G. Malliaras, *Appl. Phys. Lett.* **2017**, *111*, 023301.
[116] N. D. Robinson, P.-O. Svensson, D. Nilsson, M. Berggren, *J. Electrochem. Soc.* **2006**, *153*, H39.
[117] J. T. Friedlein, R. R. McLeod, J. Rivnay, *Org. Electron.* **2018**, *63*, 398.
[118] A. K. Ahuja, M. R. Behrend, J. J. Whalen, M. S. Humayun, J. D. Weiland, *IEEE Trans. Biomed. Eng.* **2008**, *55*, 1457.
[119] J. Newman, *J. Electrochem. Soc.* **1966**, *113*, 501.
[120] D. A. Koutsouras, P. Gkoupidenis, C. Stolz, V. Subramanian, G. G. Malliaras, D. C. Martin, *ChemElectroChem* **2017**, *4*, 2321.
[121] J. W. Thackeray, H. S. White, M. S. Wrighton, *J. Phys. Chem.* **1985**, *89*, 5133.
[122] E. W. Paul, A. J. Ricco, M. S. Wrighton, *J. Phys. Chem.* **1985**, *89*, 1441.
[123] N. P. Gaponik, D. G. Shchukin, A. I. Kulak, D. V. Sviridov, *Mendeleev Commun.* **1997**, *7*, 70.
[124] S. Chao, M. S. Wrighton, *J. Am. Chem. Soc.* **1987**, *109*, 6627.
[125] D. Nilsson, T. Kugler, P.-O. Svensson, M. Berggren, *Sens. Actuators, B* **2002**, *86*, 193.
[126] R. Dabke, G. Singh, A. Dhanabalan, R. Lal, A. Contractor, *Anal. Chem.* **1997**, *69*, 724.
[127] M. Kanungo, D. N. Srivastava, A. Kumar, A. Contractor, *Chem. Commun.* **2002**, 680.
[128] K. Krishnamoorthy, R. S. Gokhale, A. Q. Contractor, A. Kumar, *Chem. Commun.* **2004**, 820.
[129] J. W. Thackeray, M. S. Wrighton, *J. Phys. Chem.* **1986**, *90*, 6674.
[130] Z.-T. Zhu, J. T. Mabeck, C. Zhu, N. C. Cady, C. A. Batt, G. G. Malliaras, *Chem. Commun.* **2004**, 1556.
[131] K. Xie, N. Wang, X. Lin, Z. Wang, X. Zhao, P. Fang, H. Yue, J. Kim, J. Luo, S. Cui, *Elife* **2020**, *9*, e50345.
[132] C. Diacci, J. W. Lee, P. Janson, G. Dufil, G. Méhes, M. Berggren, D. T. Simon, E. Stavrinidou, *Adv. Mater. Technol.* **2020**, *5*, 1900262.
[133] S. Zhang, H. Ling, Y. Chen, Q. Cui, J. Ni, X. Wang, M. C. Hartel, X. Meng, K. Lee, J. Lee, W. Sun, H. Lin, S. Emaminejad, S. Ahadian, N. Ashammakhi, M. R. Dokmeci, A. Khademhosseini, *Adv. Funct. Mater.* **2020**, *30*, 1906016.
[134] E. Dauzon, X. Sallenave, C. Plesse, F. Goubard, A. Amassian, T. D. Anthopoulos, *Adv. Mater.* **2021**, *33*, 2101469.
[135] K. Harris, A. Elias, H.-J. Chung, *J. Mater. Sci.* **2016**, *51*, 2771.
[136] S. E. Root, S. Savagatrup, A. D. Printz, D. Rodriquez, D. J. Lipomi, *Chem. Rev.* **2017**, *117*, 6467.
[137] Q. Thiburce, N. A. Melosh, A. Salleo, *Flexible Printed Electron.* **2022**, *7*, 034001.
[138] J. Chen, W. Huang, D. Zheng, Z. Xie, X. Zhuang, D. Zhao, Y. Chen, N. Su, H. Chen, R. M. Pankow, *Nat. Mater.* **2022**, *21*, 564.
[139] Y. Leterrier, *Handbook of Flexible Organic Electronics: Materials, Manufacturing and Applications*, Woodhead Publishing, Cambridge, UK **2014**.
[140] M. Kaltenbrunner, T. Sekitani, J. Reeder, T. Yokota, K. Kuribara, T. Tokuhara, M. Drack, R. Schwödiauer, I. Graz, S. Bauer-Gogonea, *Nature* **2013**, *499*, 458.
[141] C. Lechat, A. R. Bunsell, P. Davies, *J. Mater. Sci.* **2011**, *46*, 528.
[142] K. A. Sierros, D. R. Cairns, J. S. Abell, S. N. Kukureka, *Thin Solid Films* **2010**, *518*, 2623.
[143] K.-I. Jang, K. Li, H. U. Chung, S. Xu, H. N. Jung, Y. Yang, J. W. Kwak, H. H. Jung, J. Song, C. Yang, A. Wang, Z. Liu, J. Y. Lee, B. H. Kim, J.-H. Kim, J. Lee, Y. Yu, B. J. Kim, H. Jang, K. J. Yu, J. Kim, J. W. Lee, J.-W. Jeong, Y. M. Song, Y. Huang, Y. Zhang, J. A. Rogers, *Nat. Commun.* **2017**, *8*, 15894.
[144] T. Uhrmann, L. Baer, T. Dimopoulos, N. Wiese, M. Rührig, A. Lechner, *J. Magn. Magn. Mater.* **2006**, *307*, 209.
[145] R. Katragadda, Z. Wang, W. Khalid, Y. Li, Y. Xu, *Appl. Phys. Lett.* **2007**, *91*, 083505.
[146] R. P. Von Metzen, T. Stieglitz, *Biomed. Microdevices* **2013**, *15*, 727.
[147] M. Amjadi, Y. J. Yoon, I. Park, *Nanotechnology* **2015**, *26*, 375501.
[148] H. Niu, H. Wang, H. Zhou, T. Lin, *RSC Adv.* **2014**, *4*, 11782.
[149] R. M. Grigorescu, F. Ciuprina, P. Ghioca, M. Ghiurea, L. Iancu, B. Spurcaciu, D. M. Panaitescu, *J. Phys. Chem. Solids* **2016**, *89*, 97.
[150] J. Blanchard, A. Sobey, J. Blake, *Composites, Part B* **2016**, *84*, 228.
[151] N. P. Bansal, R. H. Doremus, *Handbook of Glass Properties*, Elsevier, Amsterdam, The Netherlands **2013**.
[152] R. Ott, C. Fan, J. Li, T. Hufnagel, *J. Non-Cryst. Solids* **2003**, *317*, 158.
[153] Y. Li, R. Tanigawa, H. Okuzaki, *Smart Mater. Struct.* **2014**, *23*, 074010.
[154] B. O'Connor, E. P. Chan, C. Chan, B. R. Conrad, L. J. Richter, R. J. Kline, M. Heeney, I. McCulloch, C. L. Soles, D. M. DeLongchamp, *ACS Nano* **2010**, *4*, 7538.
[155] V. Mottaghitalab, G. M. Spinks, G. G. Wallace, *Synth. Met.* **2005**, *152*, 77.
[156] A. K. Tripathi, K. Myny, B. Hou, K. Wezenberg, G. H. Gelinck, *IEEE Trans. Electron Devices* **2015**, *62*, 4063.
[157] P. Heremans, A. K. Tripathi, A. de Jamblinne de Meux, E. C. Smits, B. Hou, G. Pourtois, G. H. Gelinck, *Adv. Mater.* **2016**, *28*, 4266.
[158] S. P. Lacour, S. Wagner, Z. Huang, Z. Suo, *Appl. Phys. Lett.* **2003**, *82*, 2404.
[159] E. Kamio, T. Yasui, Y. Iida, J. P. Gong, H. Matsuyama, *Adv. Mater.* **2017**, *29*, 1704118.
[160] L. Xu, Z. Huang, Z. Deng, Z. Du, T. L. Sun, Z. H. Guo, K. Yue, *Adv. Mater.* **2021**, *33*, 2105306.
[161] X. Li, R. Li, Z. Liu, X. Gao, S. Long, G. Zhang, *Macromol. Rapid Commun.* **2018**, *39*, 1800400.
[162] A. Al-Halhouli, H. Qitouqa, A. Alashqar, J. Abu-Khalaf, *Sens. Rev.* **2018**, *38*, 438.
[163] J. Fan, C. Montemagno, M. Gupta, *Org. Electron.* **2019**, *73*, 122.
[164] G. Scheiblin, A. Aliane, X. Strakosas, V. F. Curto, G. G. Malliaras, *MRS Commun.* **2015**, *5*, 507.
[165] A. Pierre, S. E. Doris, R. Lujan, R. A. Street, *Adv. Mater. Technol.* **2019**, *4*, 1800577.
[166] V. Zardetto, T. M. Brown, A. Reale, A. Di Carlo, *J. Polym. Sci., Part B: Polym. Phys.* **2011**, *49*, 638.
[167] B. V. Khau, A. D. Scholz, E. Reichmanis, *J. Mater. Chem. C* **2020**, *8*, 15067.
[168] J. B. Fortin, T.-M. Lu, *Chem. Mater.* **2002**, *14*, 1945.
[169] C. Liao, M. Zhang, M. Y. Yao, T. Hua, L. Li, F. Yan, *Adv. Mater.* **2015**, *27*, 7493.
[170] T. Y. Chang, V. G. Yadav, S. De Leo, A. Mohedas, B. Rajalingam, C.-L. Chen, S. Selvarasah, M. R. Dokmeci, A. Khademhosseini, *Langmuir* **2007**, *23*, 11718.
[171] G. Tarabella, M. Villani, D. Calestani, R. Mosca, S. Iannotta, A. Zappettini, N. Coppedè, *J. Mater. Chem.* **2012**, *22*, 23830.
[172] F. Vurro, M. Janni, N. Coppedè, F. Gentile, R. Manfredi, M. Bettelli, A. Zappettini, *Sensors* **2019**, *19*, 4667.

[173] E. Bihar, Y. Deng, T. Miyake, M. Saadaoui, G. G. Malliaras, M. Rolandi, *Sci. Rep.* **2016**, *6*, 27582.
[174] X. Qing, Y. Wang, Y. Zhang, X. Ding, W. Zhong, D. Wang, W. Wang, Q. Liu, K. Liu, M. Li, *ACS Appl. Mater. Interfaces* **2019**, *11*, 13105.
[175] Y. Li, N. Wang, A. Yang, H. Ling, F. Yan, *Adv. Electron. Mater.* **2019**, *5*, 1900566.
[176] X. Wu, A. Surendran, M. Moser, S. Chen, B. T. Muhammad, I. P. Maria, I. McCulloch, W. L. Leong, *ACS Appl. Mater. Interfaces* **2020**, *12*, 20757.
[177] S. Zhang, E. Hubis, G. Tomasello, G. Soliveri, P. Kumar, F. Cicoira, *Chem. Mater.* **2017**, *29*, 3126.
[178] S. T. Keene, D. Fogarty, R. Cooke, C. D. Casadevall, A. Salleo, O. Parlak, *Adv. Healthcare Mater.* **2019**, *8*, e1901321.
[179] O. Parlak, S. T. Keene, A. Marais, V. F. Curto, A. Salleo, *Sci. Adv.* **2018**, *4*, eaar2904.
[180] L. Ouyang, B. Wei, C.-C. Kuo, S. Pathak, B. Farrell, D. C. Martin, *Sci. Adv.* **2017**, *3*, e1600448.
[181] J. Y. Oh, M. Shin, J. B. Lee, J.-H. Ahn, H. K. Baik, U. Jeong, *ACS Appl. Mater. Interfaces* **2014**, *6*, 6954.
[182] M. Döbbelin, R. Marcilla, M. Salsamendi, C. Pozo-Gonzalo, P. M. Carrasco, J. A. Pomposo, D. Mecerreyes, *Chem. Mater.* **2007**, *19*, 2147.
[183] Y. Wang, C. Zhu, R. Pfattner, H. Yan, L. Jin, S. Chen, F. Molina-Lopez, F. Lissel, J. Liu, N. I. Rabiah, *Sci. Adv.* **2017**, *3*, e1602076.
[184] S. Savagatrup, E. Chan, S. M. Renteria-Garcia, A. D. Printz, A. V. Zaretski, T. F. O'Connor, D. Rodriquez, E. Valle, D. J. Lipomi, *Adv. Funct. Mater.* **2015**, *25*, 427.
[185] Y. Li, S. Zhang, X. Li, V. R. N. Unnava, F. Cicoira, *Flexible Printed Electron.* **2019**, *4*, 044004.
[186] X. Wu, A. Surendran, J. Ko, O. Filonik, E. M. Herzig, P. Müller-Buschbaum, W. L. Leong, *Adv. Mater.* **2019**, *31*, 1805544.
[187] N. Matsuhisa, Y. Jiang, Z. Liu, G. Chen, C. Wan, Y. Kim, J. Kang, H. Tran, H. C. Wu, I. You, Z. Bao, X. Chen, *Adv. Electron. Mater.* **2019**, *5*, 1900347.
[188] B. Wang, A. Facchetti, *Adv. Mater.* **2019**, *31*, 1901408.
[189] S. K. Kanakamedala, H. T. Alshakhouri, M. Agarwal, M. A. DeCoster, *Sens. Actuators, B* **2011**, *157*, 92.
[190] W. Ji, D. Wu, W. Tang, X. Xi, Y. Su, X. Guo, R. Liu, *Sens. Actuators, B* **2020**, *304*, 127414.
[191] Y. S. Yoon, C. Fabio, B. Robert, B. L. Fernando, D. Dermot, R. M. Owens, G. G. Malliaras, *Chem. Commun.* **2010**, *46*, 7972.
[192] Z. Yi, G. Natale, P. Kumar, E. Di Mauro, M.-C. Heuzey, F. Soavi, I. I. Perepichka, S. K. Varshney, C. Santato, F. Cicoira, *J. Mater. Chem. C* **2015**, *3*, 6549.
[193] S. Chen, A. Surendran, X. Wu, W. L. Leong, *Adv. Funct. Mater.* **2020**, *30*, 2006186.
[194] Z. Chen, N. Gao, Y. Chu, Y. He, Y. Wang, *ACS Appl. Mater. Interfaces* **2021**, *13*, 33557.
[195] Y. Chen, J. Meng, Y. Xu, Y. Li, Q. Zhang, C. Hou, H. Sun, G. Wang, H. Wang, *Adv. Electron. Mater.* **2021**, *7*, 2100231.
[196] H. Lee, S. Lee, W. Lee, T. Yokota, K. Fukuda, T. Someya, *Adv. Funct. Mater.* **2019**, *29*, 1906982.
[197] D. Khodagholy, V. F. Curto, K. J. Fraser, M. Gurfinkel, R. Byrne, D. Diamond, G. G. Malliaras, F. Benito-Lopez, R. M. Owens, *J. Mater. Chem.* **2012**, *22*, 4440.
[198] Y. Kim, T. Lim, C.-H. Kim, C. S. Yeo, K. Seo, S.-M. Kim, J. Kim, S. Y. Park, S. Ju, M.-H. Yoon, *NPG Asia Mater.* **2018**, *10*, 1086.
[199] B. Marchiori, R. Delattre, S. Hannah, S. Blayac, M. Ramuz, *Sci. Rep.* **2018**, *8*, 8477.
[200] W. Lee, S. Kobayashi, M. Nagase, Y. Jimbo, I. Saito, Y. Inoue, T. Yambe, M. Sekino, G. G. Malliaras, T. Yokota, M. Tanaka, T. Someya, *Sci. Adv.* **2018**, *4*, eaau2426.
[201] R. A. Green, R. T. Hassarati, L. Bouchinet, C. S. Lee, G. L. Cheong, F. Y. Jin, C. W. Dodds, G. J. Suaning, L. A. Poole-Warren, N. H. Lovell, *Biomaterials* **2012**, *33*, 5875.
[202] M. Moser, L. R. Savagian, A. Savva, M. Matta, J. F. Ponder Jr, T. C. Hidalgo, D. Ohayon, R. Hallani, M. Reisjalali, A. Troisi, *Chem. Mater.* **2020**, *32*, 6618.
[203] I. R. Minev, P. Musienko, A. Hirsch, Q. Barraud, N. Wenger, E. M. Moraud, J. Gandar, M. Capogrosso, T. Milekovic, L. Asboth, *Science* **2015**, *347*, 159.
[204] O. Graudejus, P. Görrn, S. Wagner, *ACS Appl. Mater. Interfaces* **2010**, *2*, 1927.
[205] I. M. Graz, D. P. Cotton, S. P. Lacour, *Appl. Phys. Lett.* **2009**, *94*, 071902.
[206] Y. Lee, J. Y. Oh, W. Xu, O. Kim, T. R. Kim, J. Kang, Y. Kim, D. Son, J. B.-H. Tok, M. J. Park, *Sci. Adv.* **2018**, *4*, eaat7387.
[207] S. Jang, C. Kim, J. J. Park, M. L. Jin, S. J. Kim, O. O. Park, T. S. Kim, H. T. Jung, *Small* **2018**, *14*, 1702818.
[208] W. Huang, J. Chen, Y. Yao, D. Zheng, X. Ji, L.-W. Feng, D. Moore, N. R. Glavin, M. Xie, Y. Chen, *Nature* **2023**, *613*, 496.
[209] L. Peng, L. Xiaoteng, H. I-Ming, Y. Feng, *Adv. Mater.* **2011**, *23*, 4035.
[210] A. Yang, Y. Li, C. Yang, Y. Fu, F. Yan, *Adv. Mater.* **2018**, *30*, 1800051.
[211] X. Xi, D. Wu, W. Ji, S. Zhang, W. Tang, Y. Su, X. Guo, R. Liu, *Adv. Funct. Mater.* **2019**, *30*, 1905361.
[212] Y. Yao, W. Huang, J. Chen, G. Wang, H. Chen, X. Zhuang, Y. Ying, J. Ping, T. J. Marks, A. Facchetti, *Proc. Natl. Acad. Sci. USA* **2021**, *118*, 2111790118.
[213] Y. J. Jo, H. Kim, J. Ok, Y. J. Shin, J. H. Shin, T. H. Kim, Y. Jung, T.-i. Kim, *Adv. Funct. Mater.* **2020**, *30*, 1909707.
[214] A. Campana, T. Cramer, D. T. Simon, M. Berggren, F. Biscarini, *Adv. Mater.* **2014**, *26*, 3874.
[215] W. Lee, D. Kim, J. Rivnay, N. Matsuhisa, T. Lonjaret, T. Yokota, H. Yawo, M. Sekino, G. G. Malliaras, T. Someya, *Adv. Mater.* **2016**, *28*, 9722.
[216] S. Park, S. W. Heo, W. Lee, D. Inoue, Z. Jiang, K. Yu, H. Jinno, D. Hashizume, M. Sekino, T. Yokota, K. Fukuda, K. Tajima, T. Someya, *Nature* **2018**, *561*, 516.
[217] L. J. Currano, F. C. Sage, M. Hagedon, L. Hamilton, J. Patrone, K. Gerasopoulos, *Sci. Rep.* **2018**, *8*, 15890.
[218] J. Kim, A. S. Campbell, B. E.-F. de Ávila, J. Wang, *Nat. Biotechnol.* **2019**, *37*, 389.
[219] Y. Yang, W. Gao, *Chem. Soc. Rev.* **2019**, *48*, 1465.
[220] L. Piwek, D. A. Ellis, S. Andrews, A. Joinson, *PLoS Med.* **2016**, *13*, e1001953.
[221] J. Kim, A. S. Campbell, J. Wang, *Talanta* **2018**, *177*, 163.
[222] N. Coppedè, M. Janni, M. Bettelli, C. L. Maida, F. Gentile, M. Villani, R. Ruotolo, S. Iannotta, N. Marmiroli, M. Marmiroli, A. Zappettini, *Sci. Rep.* **2017**, *7*, 16195.
[223] D. Majak, J. Fan, M. Gupta, *Sens. Actuators, B* **2019**, *286*, 111.
[224] Y. Wang, Y. Wang, R. Zhu, Y. Tao, Y. Chen, Q. Liu, X. Liu, D. Wang, *Mater. Sci. Eng., B* **2022**, *278*, 115657.
[225] Y. Wang, X. Qing, Q. Zhou, Y. Zhang, Q. Liu, K. Liu, W. Wang, M. Li, Z. Lu, Y. Chen, *Biosens. Bioelectron.* **2017**, *95*, 138.
[226] R. R. Nair, *Flexible Printed Electron.* **2020**, *5*, 015001.
[227] S. Demuru, C.-H. Huang, K. Parvez, R. Worsley, G. Mattana, B. Piro, V. Noël, C. Casiraghi, D. Briand, *ACS Appl. Nano Mater.* **2022**, *5*, 1664.
[228] E. Battista, V. Lettera, M. Villani, D. Calestani, F. Gentile, P. A. Netti, S. Iannotta, A. Zappettini, N. Coppedè, *Org. Electron.* **2016**, *40*, 51.
[229] M. Berto, C. Diacci, L. Theuer, M. D. Lauro, C. A. Bortolotti, *Flexible Printed Electron.* **2018**, *3*, 024001.
[230] Y. Liang, T. Guo, L. Zhou, A. Offenhäusser, D. Mayer, *Materials* **2020**, *13*, 2577.
[231] R. Zhu, Y. Wang, Y. Tao, Y. Wang, Y. Chen, M. Li, Q. Liu, L. Yang, D. Wang, *Electrochim. Acta* **2022**, *425*, 140716.

[232] S. Demuru, J. Kim, M. El Chazli, S. Bruce, M. Dupertuis, P.-A. Binz, M. Saubade, C. Lafaye, D. Briand, *ACS Sens.* **2022**, *7*, 2721.
[233] Y. Song, H. Zhang, T. Mukhopadhyaya, A. S. Hall, H. E. Katz, *Biosens. Bioelectron.* **2022**, *216*, 114691.
[234] M. Bariya, H. Y. Y. Nyein, A. Javey, *Nat. Electron.* **2018**, *1*, 160.
[235] J. Ping, Y. Wang, K. Fan, W. Tang, J. Wu, Y. Ying, *J. Mater. Chem. B* **2013**, *1*, 4781.
[236] C. Jiang, X. Li, Y. Yao, Y. Ying, J. Ping, *Anal. Chem.* **2018**, *90*, 13088.
[237] M. Berggren, R. Forchheimer, J. Bobacka, P.-O. Svensson, D. Nilsson, O. Larsson, A. Ivaska, in *Organic Semiconductors in Sensor Applications*, Springer, Berlin, Germany **2008**, pp. 263–280.
[238] P. Lin, F. Yan, H. L. W. Chan, *ACS Appl. Mater. Interfaces* **2010**, *2*, 1637.
[239] Y. Wang, Z. Zhou, X. Qing, W. Zhong, Q. Liu, W. Wang, M. Li, K. Liu, D. Wang, *Anal. Bioanal. Chem.* **2016**, *408*, 5779.
[240] C. Yao, C. Xie, P. Lin, F. Yan, P. Huang, I. M. Hsing, *Adv. Mater.* **2013**, *25*, 6575.
[241] S. Wustoni, C. Combe, D. Ohayon, M. H. Akhtar, I. Mcculloch, S. Inal, *Adv. Funct. Mater.* **2019**, *29*, 1904403.
[242] S. Sukeerthi, A. Contractor, *Anal. Chem.* **1999**, *71*, 2231.
[243] M. Kanungo, A. Kumar, A. Contractor, *Anal. Chem.* **2003**, *75*, 5673.
[244] D. Hoa, T. S. Kumar, N. Punekar, R. Srinivasa, R. Lal, A. Contractor, *Anal. Chem.* **1992**, *64*, 2645.
[245] H. Sangodkar, S. Sukeerthi, R. Srinivasa, R. Lal, A. Contractor, *Anal. Chem.* **1996**, *68*, 779.
[246] P. Bartlett, P. Birkin, *Anal. Chem.* **1993**, *65*, 1118.
[247] P. Bartlett, P. Birkin, *Anal. Chem.* **1994**, *66*, 1552.
[248] P. Bartlett, *Analyst* **1998**, *123*, 387.
[249] P. Bartlett, J. Wang, *J. Chem. Soc., Faraday Trans.* **1996**, *92*, 4137.
[250] F. Battaglini, P. Bartlett, J. Wang, *Anal. Chem.* **2000**, *72*, 502.
[251] D. Raffa, K. Leung, F. Battaglini, *Anal. Chem.* **2003**, *75*, 4983.
[252] P. N. Bartlett, Y. Astier, *Chem. Commun.* **2000**, 105.
[253] G. Tarabella, C. Santato, Y. Y. Sang, S. Iannotta, G. G. Malliaras, F. Cicoira, *Appl. Phys. Lett.* **2010**, *97*, 205.
[254] C. Fabio, S. Michele, Y. Omid, J. A. Defranco, Y. S. Yoon, G. G. Malliaras, *Adv. Mater.* **2010**, *22*, 1012.
[255] O. Yaghmazadeh, F. Cicoira, D. A. Bernards, S. Y. Yang, Y. Bonnassieux, G. G. Malliaras, *J. Polym. Sci., Part B: Polym. Phys.* **2015**, *49*, 34.
[256] Y. Kim, J. Do, J. Kim, Y. Y. Sang, G. G. Malliaras, C. K. Ober, E. Kim, *Jpn. J. Appl. Phys.* **2010**, *49*, 01AE10.
[257] A. M. Pappa, D. Ohayon, A. Giovannitti, I. P. Maria, A. Savva, I. Uguz, J. Rivnay, I. McCulloch, R. M. Owens, S. Inal, *Sci. Adv.* **2018**, *4*, eaat0911.
[258] D. Ohayon, G. Nikiforidis, A. Savva, A. Giugni, S. Wustoni, T. Palanisamy, X. Chen, I. P. Maria, E. Di Fabrizio, P. Costa, I. McCulloch, S. Inal, *Nat. Mater.* **2020**, *19*, 456.
[259] A. Koklu, D. Ohayon, S. Wustoni, A. Hama, X. Chen, I. McCulloch, S. Inal, *Sens. Actuators, B* **2021**, *329*, 129251.
[260] S. T. M. Tan, A. Giovannitti, A. Melianas, M. Moser, B. L. Cotts, D. Singh, I. McCulloch, A. Salleo, *Adv. Funct. Mater.* **2021**, *31*, 2010868.
[261] S. Wustoni, T. C. Hidalgo, A. Hama, D. Ohayon, A. Savva, N. Wei, N. Wehbe, S. Inal, *Adv. Mater. Technol.* **2019**, *5*, 1900943.
[262] M. Braendlein, A. M. Pappa, M. Ferro, A. Lopresti, C. Acquaviva, E. Mamessier, G. G. Malliaras, R. M. Owens, *Adv. Mater.* **2017**, *29*, 1605744.
[263] A. M. Pappa, V. F. Curto, M. Braendlein, X. Strakosas, M. J. Donahue, M. Fiocchi, G. G. Malliaras, R. M. Owens, *Adv. Healthcare Mater.* **2016**, *5*, 2295.
[264] H. Tang, P. Lin, H. L. W. Chan, F. Yan, *Biosens. Bioelectron.* **2011**, *26*, 4559.
[265] C. Xiong, W. Yang, Q. Hao, L. Zhang, L. Qiu, C. Wei, Y. Feng, Z. Lei, *Sens. Actuators, B* **2017**, *246*, 235.
[266] C. Liao, M. Zhang, L. Niu, Z. Zheng, F. Yan, *J. Mater. Chem. B* **2014**, *2*, 191.
[267] C. H. Mak, C. Liao, Y. Fu, M. Zhang, C. Y. Tang, Y. H. Tsang, H. L. W. Chana, F. Yan, *J. Mater. Chem. C* **2015**, *3*, 6532.
[268] X. Zhou, Q. Zhu, Y. Yang, *Biosens. Bioelectron.* **2020**, *165*, 112422.
[269] H. Yu, Z. Chen, Y. Liu, O. Alkhamis, Z. Song, Y. Xiao, *Angew. Chem., Int. Ed.* **2021**, *60*, 2993.
[270] S. Lin, X. Cheng, J. Zhu, B. Wang, D. Jelinek, Y. Zhao, T.-Y. Wu, A. Horrillo, J. Tan, J. Yeung, *Sci. Adv.* **2022**, *8*, eabq4539.
[271] R.-X. He, M. Zhang, F. Tan, P. H. Leung, X.-Z. Zhao, H. L. Chan, M. Yang, F. Yan, *J. Mater. Chem.* **2012**, *22*, 22072.
[272] D.-J. Kim, N.-E. Lee, J.-S. Park, I.-J. Park, J.-G. Kim, H. J. Cho, *Biosens. Bioelectron.* **2010**, *25*, 2477.
[273] Y. Fu, N. Wang, A. Yang, H. K.-w. Law, L. Li, F. Yan, *Adv. Mater.* **2017**, *29*, 1703787.
[274] X. Guo, J. Liu, F. Liu, F. She, Q. Zheng, H. Tang, M. Ma, S. Yao, *Sens. Actuators, B* **2017**, *240*, 1075.
[275] P. Seshadri, K. Manoli, N. Schneiderhan-Marra, U. Anthes, P. Wierzchowiec, K. Bonrad, C. Di Franco, L. Torsi, *Biosens. Bioelectron.* **2018**, *104*, 113.
[276] M. Magliulo, D. De Tullio, I. Vikholm-Lundin, W. M. Albers, T. Munter, K. Manoli, G. Palazzo, L. Torsi, *Anal. Bioanal. Chem.* **2016**, *408*, 3943.
[277] E. Macchia, R. A. Picca, K. Manoli, C. Di Franco, D. Blasi, L. Sarcina, N. Ditaranto, N. Cioffi, R. Österbacka, G. Scamarcio, *Mater. Horiz.* **2020**, *7*, 999.
[278] S. K. Sailapu, E. Macchia, I. Merino-Jimenez, J. P. Esquivel, L. Sarcina, G. Scamarcio, S. D. Minteer, L. Torsi, N. Sabaté, *Biosens. Bioelectron.* **2020**, *156*, 112103.
[279] E. Macchia, K. Manoli, B. Holzer, C. Di Franco, M. Ghittorelli, F. Torricelli, D. Alberga, G. F. Mangiatordi, G. Palazzo, G. Scamarcio, *Nat. Commun.* **2018**, *9*, 3223.
[280] H. Lilja, D. Ulmert, A. J. Vickers, *Nat. Rev. Cancer* **2008**, *8*, 268.
[281] H. Fang, K. J. Yu, C. Gloschat, Z. Yang, E. Song, C.-H. Chiang, J. Zhao, S. M. Won, S. Xu, M. Trumpis, Y. Zhong, S. W. Han, Y. Xue, D. Xu, S. W. Choi, G. Cauwenberghs, M. Kay, Y. Huang, J. Viventi, I. R. Efimov, J. A. Rogers, *Nat. Biomed. Eng.* **2017**, *1*, 0038.
[282] J. J. Jun, N. A. Steinmetz, J. H. Siegle, D. J. Denman, M. Bauza, B. Barbarits, A. K. Lee, C. A. Anastassiou, A. Andrei, Ç. Aydın, *Nature* **2017**, *551*, 232.
[283] D.-H. Kim, N. Lu, R. Ghaffari, Y.-S. Kim, S. P. Lee, L. Xu, J. Wu, R.-H. Kim, J. Song, Z. Liu, *Nat. Mater.* **2011**, *10*, 316.
[284] J. W. Jeong, M. K. Kim, H. Cheng, W. H. Yeo, X. Huang, Y. Liu, Y. Zhang, Y. Huang, J. A. Rogers, *Adv. Healthcare Mater.* **2014**, *3*, 642.
[285] S. J. Kim, K. W. Cho, H. R. Cho, L. Wang, S. Y. Park, S. E. Lee, T. Hyeon, N. Lu, S. H. Choi, D. H. Kim, *Adv. Funct. Mater.* **2016**, *26*, 3207.
[286] C. Yao, Q. Li, J. Guo, F. Yan, I. M. Hsing, *Adv. Healthcare Mater.* **2015**, *4*, 528.
[287] O. Salyk, J. Víteček, L. Omasta, E. Šafaříková, S. Stříteský, M. Vala, M. Weiter, *Appl. Sci.* **2017**, *7*, 998.
[288] J. Kang, Y.-W. Lim, I. Lee, S. Kim, K. Y. Kim, W. Lee, B.-S. Bae, *ACS Appl. Mater. Interfaces* **2022**, *14*, 24840.
[289] Y. Dai, S. Dai, N. Li, Y. Li, M. Moser, J. Strzalka, A. Prominski, Y. Liu, Q. Zhang, S. Li, H. Hu, W. Liu, S. Chatterji, P. Cheng, B. Tian, I. McCulloch, J. Xu, S. Wang, *Adv. Mater.* **2022**, *34*, 2201178.
[290] G. D. Spyropoulos, J. N. Gelinas, D. Khodagholy, *Sci. Adv.* **2019**, *5*, eaau7378.
[291] S. Chen, K. Hou, T. Li, X. Wu, Z. Wang, L. Wei, W. L. Leong, *Adv. Mater. Technol.* **2022**, *8*, 2200611.
[292] J. Wang, S. Lee, T. Yokota, T. Someya, *Adv. Funct. Mater.* **2022**, *32*, 2200458.
[293] M. S. Balda, J. A. Whitney, C. Flores, S. González, M. Cereijido, K. Matter, *J. Cell Biol.* **1996**, *134*, 1031.

[294] S. Tria, L. H. Jimison, A. Hama, M. Bongo, R. M. Owens, *Biosensors* **2013**, *3*, 44.
[295] S. A. Tria, M. Ramuz, M. Huerta, P. Leleux, J. Rivnay, L. H. Jimison, A. Hama, G. G. Malliaras, R. M. Owens, *Adv. Healthcare Mater.* **2014**, *3*, 1053.
[296] M. Ramuz, A. Hama, J. Rivnay, P. Leleux, R. Owens, *J. Mater. Chem. B* **2015**, *3*, 5971.
[297] A. Romeo, G. Tarabella, P. D'Angelo, C. Caffarra, D. Cretella, R. Alfieri, P. G. Petronini, S. Iannotta, *Biosens. Bioelectron.* **2015**, *68*, 791.
[298] M. Ramuz, A. Hama, M. Huerta, J. Rivnay, P. Leleux, R. M. Owens, *Adv. Mater.* **2014**, *26*, 7083.
[299] F. Decataldo, M. Barbalinardo, D. Gentili, M. Tessarolo, M. Calienni, M. Cavallini, B. Fraboni, *Adv. Biosyst.* **2020**, *4*, 1900204.
[300] K. Tybrandt, R. Forchheimer, M. Berggren, *Nat. Commun.* **2012**, *3*, 871.
[301] M. Ha, Y. Xia, A. A. Green, W. Zhang, M. J. Renn, C. H. Kim, M. C. Hersam, C. D. Frisbie, *ACS Nano* **2010**, *4*, 4388.
[302] S. Wang, Y. Gao, Q. Huang, X. Guo, A. Yang, Y. Zhang, Q. Zhuang, D. Chen, L. Chen, X. Ju, *Adv. Funct. Mater.* **2022**, *32*, 2203730.
[303] M. Massetti, S. Zhang, H. Padinare, B. Burtscher, C. Diacci, D. T. Simon, X. Liu, M. Fahlman, D. Tu, M. Berggren, S. Fabiano, *npj Flexible Electron.* **2023**, *7*, 11.
[304] J. Song, G. Tang, J. Cao, H. Liu, Z. Zhao, S. Griggs, A. Yang, N. Wang, H. Cheng, C. K. Liu, I. McCulloch, F. Yan, *Adv. Mater.* **2022**, *35*, 2207763.
[305] B. Lin, M. Wang, C. Zhao, S. Wang, K. Chen, X. Li, Z. Long, C. Zhao, X. Song, S. Yan, *npj Flexible Electron.* **2022**, *6*, 77.
[306] A. Takemoto, T. Araki, K. Nishimura, M. Akiyama, T. Uemura, K. Kiriyama, J. M. Koot, Y. Kasai, N. Kurihira, S. Osaki, *Adv. Sci.* **2023**, *10*, 2204746.
[307] T. Li, J. Y. Cheryl Koh, A. Moudgil, H. Cao, X. Wu, S. Chen, K. Hou, A. Surendran, M. Stephen, C. Tang, C. Wang, Q. J. Wang, C. Y. Tay, W. L. Leong, *ACS Nano* **2022**, *16*, 12049.
[308] Y. Deng, H. Qi, Y. Ma, S. Liu, M. Zhao, Z. Guo, Y. Jie, R. Zheng, J. Jing, K. Chen, H. Ding, G. Lv, K. Zhang, R. Li, H. Cheng, L. Zhao, X. Sheng, M. Zhang, L. Yin, *Proc. Natl. Acad. Sci. USA* **2022**, *119*, 2208060119.

Yao Yao received her Ph.D. degree from the College of Biosystems Engineering and Food Science of the Zhejiang University in 2021. She worked as a Visiting Scholar at the Department of Chemistry and the Materials Research Center, Northwestern University, from 2019 to 2020 under the supervision of Prof. Tobin J. Marks and Prof. Antonio Facchetti. Her main research interests are transistors and transistor-based biosensors.

Wei Huang obtained his B.S. (2010) in physics from Nankai University and his Ph.D. (2016) in optical engineering from the University of Electronic Science and Technology of China (UESTC). He was a Postdoctoral Fellow and later a Research Assistant Professor in the Department of Chemistry, Northwestern University, under the supervision of Prof. Tobin J. Marks and Prof. Antonio Facchetti. Currently, he is a Professor in the School of Automation Engineering, UESTC. His research interests include flexible/stretchable electronics, transistor-based multifunctional sensors, and solar cells.

Jianfeng Ping is a Tenured Professor at the Zhejiang University. He obtained his B.S. degree at the Zhejiang University of Technology and his Ph.D. degree at the Zhejiang University. His current research interests focus on functional nanomaterials, agricultural sensors, agricultural information IntelliSense, microenergy harvesting technology for the agricultural environment, plant electronics, and plant nanoscience.

Tobin J. Marks is Ipatieff Professor of Catalysis and Materials Science and Engineering at the Northwestern University. He holds University of Maryland B.S. and Massachusetts Institute of Technology Ph.D. degrees. Research interests: unconventional catalysis, soft and hard matter optoelectronic and photovoltaic materials. Recognitions: U.S. National Medal of Science, Spanish Principe de Asturias Prize, MRS Von Hippel Award, Dreyfus Prize in Chemical Sciences, NAS Award in Chemical Sciences, ACS Priestley Medal, Israel Harvey Prize, German Chemical Society Ziegler Prize.

Antonio Facchetti obtained his Ph.D. degree in chemical sciences from the University of Milan. He is a Co-Founder and currently the Chief Technology Officer of the Flexterra Corporation and a Research Professor of Chemistry at the Northwestern University. He has published about 560 research articles and holds about 120 patents. He received the ACS Award for Creative Invention, the Giulio Natta Gold Medal of the Italian Chemical Society, the team IDTechEx Printed Electronics Europe Award, the corporate Flextech Award. He is a Fellow of the National Academy of Inventors, European Academy of Sciences, Kavli Foundation, American Association for the Advancement of Science, Materials Research Society, American Chemical Society-Polymeric Materials: Science and Engineering Division, and Royal Society of Chemistry.